SLAC-R-1015

Study of Rare Gluonic Penguin Decays B to Phi K Pi (Pi) at BaBar

By Yanyan Gao

SLAC National Accelerator Laboratory, Stanford University, Stanford CA 94309

Work funded in part by DOE Contract DE-AC02-76SF00515

STUDY OF RARE GLUONIC PENGUIN DECAYS

B TO PHI K PI (PI) AT BABAR

by

Yanyan Gao

A dissertation submitted to The Johns Hopkins University in conformity with the requirements for the degree of Doctor of Philosophy.

Baltimore, Maryland

Janurary, 2009

Abstract

The Standard Model of particle physics describes the elementary particles and interactions at an energy level around 100 GeV or less with unprecedented success. However, it is far from being conclusive, with some essential pieces not exactly understood. While the direct access to new physics beyond the Standard Model may be beyond the energy reach of the current operating accelerators, one can look for them in virtual transitions, such as the rare gluonic penguin decays $B \to \varphi K\pi(\pi)$. Furthermore, in the $B \to \varphi(1020)K^*(892)$ decay an interesting polarization puzzle which could indicate some new physics effects has been observed and thereby motivates this thesis.

Three amplitude and angular analyses on decays $B \to \varphi K_J^{(*)}$ are performed based on about 465 million or 384 million $B\overline{B}$ pairs recorded with the *BABAR* detector. Twelve $K_J^{(*)}$ resonances are included in four different final states $K^+\pi^-$, $K_S^0\pi^+$, $K^+\pi^0$ and $K^+\pi^+\pi^-$. Branching fractions, CP-violation parameters and polarizations measurements are made.

The branching fractions of vector–scalar decays $B^0 \to \varphi(K\pi)_0^{*0}$ and $B^\pm \to \varphi(K\pi)_0^{*\pm}$ are measured to be $(4.3 \pm 0.6 \pm 0.4) \times 10^{-6}$ and $(7.0 \pm 1.3 \pm 0.9) \times 10^{-6}$, respectively. The

ABSTRACT

branching fractions of vector–tensor decays $B^0 \to \varphi K_2^*(1430)^0$ and $B^+ \to \varphi K_2^*(1430)^+$ are measured to be $(7.5 \pm 0.9 \pm 0.5) \times 10^{-6}$ and $(8.4 \pm 1.8 \pm 1.0) \times 10^{-6}$, respectively. The longitudinal polarizations f_L of vector–tensor decays $B^0 \to \varphi K_2^*(1430)^0$ and $B^+ \to \varphi K_2^*(1430)^+$ are measured to be $0.901^{+0.046}_{-0.058} \pm 0.037$ and $0.80^{+0.09}_{-0.10} \pm 0.03$, both consistent with the naive Standard Model prediction of $f_L \approx 1$.

Vector–axial-vector decay $B^\pm \to \varphi K_1(1270)^\pm$ is observed for the first time with 5.0σ significance. The branching fraction and the longitudinal polarization of this decay are measured to be $(6.1 \pm 1.6 \pm 1.1) \times 10^{-6}$ and $0.46^{+0.12+0.06}_{-0.13-0.07}$, respectively. This polarization measurement is not consistent with the naive standard model expectation, requiring the presence of a positive-helicity amplitude from a currently unknown source.

Upper limits at 90% confidence level are placed on the branching fractions of decays B^0 and $B^\pm$ to final states with φ and $K^*(1680)^0$, $K_3^*(1780)^0$, $K_4^*(2045)^0$ and $\overline{D}^0$, and $K_1(1400)^\pm$, $K^*(1410)^\pm$ and $K_2(1770)^\pm$ or $K_2(1820)^\pm$ mesons.

Primary Reader: Andrei V. Gritsan

Secondary Reader: Petar Maksimovic

Acknowledgements

I would like to thank first my advisor Andrei Gritsan for the inspirations and encouragement. Your faith in me helped me realize my potential and passion for particle physics. Many times that I was blind to my mistakes, you respected my thoughts and patiently lead me through the logic and let me find the mistakes myself. It is from these practices that I learn to sift through the technical details and get the big physics picture. Your no tolerance of sloppiness and all those expressions following “when I was a graduate student” set me perfect examples in both the research and life.

Thanks to the PEP-II and BaBar collaborators for the effort in bringing the data, without which none of these measurements are possible. Thanks to the quasi-two-body analysis working group, especially Jim Smith, Bill Ford, Fernando Palomo, Walter Toki, Jim Hirschauer and Marc Verderi, for the insightful suggestions and comments to the analyses in this thesis. Thanks to Zijin Guo for being such a great officemate and more importantly for answering my many technical questions. Thanks to Riccardo, Jordi and Diego for the help in the SVT commission and especially those night pagers.

ACKNOWLEDGEMENTS

Thanks to the faculty members at the Hopkins for the useful academic advice. In particular, I would like to thank Petar Maksimovi for sending me to Fermilab in the summer of 2004 and teaching me the important lesson of keeping my mind open. Thanks to Morris Swartz and Bruce Barnett for guiding me through the early years of graduate school and especially in choosing the advisor. Thanks to Jonathan Bagger for introducing me to the beauty of the theoretical particle physics. Thanks to David Kaplan for giving me the opportunity to work in a phenomenology project. Thanks to Prof Gabor and Susan Domokos for the rewarding physics courses. Thanks to Prof David Neufeld, Fred Davidson, Ludwid Brand, Danielle Tarraf and Chi-Ling Chien for being on my thesis defense committee.

Thanks to my friends at Hopkins for those wonderful three years at Baltimore. Thank you Leyi, Hongyu, Wei, Xiaozhou and Kuang-Han for throwing me the thesis defense party. Thanks to my friends Minliang, Ada, Chris, Joe and Joel for the fun time in the California. All of you made my graduate life much colorful.

Finally and most importantly, I would like to thank my family for the unconditional love and support. Thanks to my parents for giving the life, teaching me right from wrong and always supporting me near and far. My deep thanks to my husband Guichun for everything you do for me. I would always appreciate your adventure of leaving your family, friends and work and flying thousands of miles to be with me.

Dedication

This thesis is dedicated to my beloved mother Ji Lin.

Contents

List of Tables

List of Figures

Chapter 1

Introduction

1.1 Introduction to the Standard Model

1.1.1 Elementary Particles and Interactions

The Standard Model (SM) of particles and interactions is built to understand the laws of the nature at the fundamental level, by addressing the questions of what are the elementary building blocks of matter and how do they interact. It is based on the combination of quantum theory and special relativity, namely quantum field theory, in which particles are introduced as quantum fields and the physics is formulated by the Lagrangian $\mathcal{L}$.

According to this model, the basic constituents of matter are fermions with spin-$\frac{1}{2}$, consisting of quarks that form the hadrons (protons, neutrons, pions, etc.) and leptons (electrons, muons, neutrinos, etc.). The basic properties are given by Table 1.1. They obey Fermi-Dirac statistics based on the Pauli Exclusion Principle. So far, there are six kinds (flavors) of quarks and leptons, naturally grouped in three generations (families), the origin of which is not given by the Standard Model itself, rather as an experimental observation. The six quarks are up and down (u, d), charmed and strange (c, s), top and bottom (t, b). The leptons are neutrinoes and charged leptons (ν_e, e), (ν_μ, μ^-) and (ν_τ, τ^-). The interactions of the fermions within each generation are the same. But the universe is primarily composed of the least massive first generation fermions (u, d) and (ν_e, e^-). The second and third generation fermions are usually produced in the accelerators, and decay rapidly to the first generation fermions. There are two types of hadrons. A baryon like the proton is built primarily from three quarks qqq, while a meson like the pion is built from a quark and an antiquark ($\bar{q}$).

In the Standard Model, fundamental interactions are interpreted in terms of exchanges of the other type of elementary particles, bosons with integral spins. Three of the four fundamental forces are included in the Standard Model, electromagnetic force mediated by massless spin-1 photons γ, weak force mediated by massive spin-1 $W^\pm$ (81 GeV) and Z^0 (91 GeV) bosons, and strong force mediated by eight massless spin-1 gluons g. The quarks participate in all the interactions, while the leptons do not interact via the strong force. The bosons are also referred to as gauge bosons, as the interactions in the Standard Model are called gauge theories, where there is an intrinsic invariance principle (gauge invariance) that requires the presence of these interactions, thereby the gauge bosons. The other funda-

Table 1.1: Basic properties of leptons and quarks [56]. The u-, d- and s-quark masses are estimates of so-called "current quark" masses, in a mass-independent subtraction scheme such as $\overline{\mathrm{MS}}$ at a scale $\mu \approx 2$ GeV. The c- and b-quark masses are the "running" masses in the $\overline{\mathrm{MS}}$ scheme.

		Leptons			Quarks	
Generation		Charge(e)	Mass(MeV)	Flavor	Charge(e)	Mass(MeV)
First	ν_e	0	$> 0?$	up	2/3	1.5-3.3
	e	-1	0.51	$d$own	-1/3	3.5-6.0
Second	ν_μ	0	$> 0?$	$c$harmed	2/3	104^{+26}_{-34}
	μ	-1	105.7	$s$trange	-1/3	1270^{+70}_{-110}
Third	ν_τ	0	$> 0?$	$t$op	2/3	$(4.2^{+0.2}_{-0.1}) \times 10^3$
	τ	-1	1776.8	$b$ottom	-1/3	$(171.2 \pm 2.1) \times 10^3$

mental interaction not included in the Standard Model is the much weaker gravity, which is expected to be mediated by massless spin-2 gravitons. Its effect becomes strong at a much higher energy level, the Planck scale around 10^{28}eV, compared with the electroweak interaction energy scale 10^{11}eV. Many theorists believe that it can only be described in the framework of string theory. To indicate the relative magnitudes of the four forces, the comparative strengths of the force between two protons when just in contact are roughly shown in Table 1.2.

Table 1.2: Relative strengths of the four forces between two protons when just in contact.

strong	electromagnetic	weak	gravity
1	10^{-2}	10^{-7}	10^{-39}

The Standard Model describes the elementary particles and interactions at an energy level of around 100 GeV or less with unprecedented success. But it is logically inconsistent. Some essential pieces are not exactly understood, such as origin of mass and how to extrapolate the SM physics to an arbituarily high energy scale such as the Planck scale. There are also a variety of fundamental questions not included in the model, such as the nature of dark matter and how to unify gravity with other interactions, the understanding of which has to rely on some new physics beyond the SM.

1.1.2 The Standard Model Lagrangian

Similar to the classical mechanics, the Standard Model Lagrangian $\mathcal{L} = T - V$, T for the kinetic energy of free fermions and V describing the interactions. The Standard Model Lagrangian $\mathcal{L}$ is assumed to be internally invariant under three sets of transformations $SU(2) \times U(1) \times SU(3)$, each of which is associated with some physical interactions.

The free fermions satisfy the relativistic equation of motion, the $Dirac\,Equation$ [1],

$$(i\gamma^\mu \partial_\mu - m)\psi = 0 \tag{1.1}$$

instead of the $Schrödinger\,Equation$ to ensure its invariance under the Lorentz transformation. In this notation, the spin-$\frac{1}{2}$ fermions are represented by the four-component spinor ψ. The $4 \times 4\,\gamma$-matrices $\gamma^\mu\ :\ (\gamma^0, \gamma^i)$ are chosen mathematically to be consistent with the experimentally observed interactions. The Lagrangian of the free fermions $Dirac\,Kinetic\,Energy$ is thus given by (not derived!),

$$\mathcal{L} = \bar{\psi}(i\gamma^\mu \partial_\mu - m)\psi. \tag{1.2}$$

The four-component spinor ψ solution of the Dirac equation can be rewritten as a pair of two-component spinors

$$\psi = \begin{pmatrix} \psi_R \\ \psi_L \end{pmatrix}.$$

The $Dirac\,Equation$ can be reduced to the 2×2 forms. It turns out that the ψ_R (right-handed fermion) and ψ_L (left-handed fermion) are two different eigenstates under the parity transformation, where $\vec{x} \to -\vec{x}, \vec{p} \to -\vec{p}$. However, only the left-handed fermions feel the weak force in the SM.

The interactions enter the $\mathcal{L}$ by replacing ∂_μ in $\psi\gamma^\mu\partial_\mu\psi$ by covariant derivative $\mathcal{D}_\mu$,

$$\mathcal{D}_\mu = \partial_\mu - ig_1\frac{Y}{2}B_\mu - ig_2\frac{\tau^i}{2}W^i_\mu - ig_3\frac{\lambda^a}{2}G^a_\mu. \tag{1.3}$$

The second term represents the U(1) symmetry, with one spin-1 field B_μ needed to maintain the U(1) gauge invariance. Similarly, the third and fourth terms represents the SU(2) and SU(3) symmetries, with three vector fields W^i_μ, $i = 1, 2, 3$ and eight vector fields G^a_μ, $a = 1 - 8$ needed to maintain the SU(2) and SU(3) gauge invariance respectively. Each of the vector fields is associated with a generator, represented by a constant Y in the SU(1) space, a 2×2 matrix τ^i in SU(2) space and a 3×3 matrices λ^a in SU(3) space. These vector fields do not necessarily all represent the physical gauge bosons, but are associated with the gauge bosons that are given later. The g_1, g_2, g_3 terms are introduced as $coupling\,constants$ to be measured experimentally. Now the Lagrangian for the first generation fermions can be written as [2]:

$$\mathcal{L}_{\texttt{ferm}} = \sum_{f = L, e_R, Q_L, u_R, d_R} \bar{f} i\gamma^\mu \mathcal{D}_\mu f. \tag{1.4}$$

The Lagrangian $\mathcal{L}$ for the second and third generation fermions $\mathcal{L}$s can be obtained by substituting the (ν_e, e, u, d) with (ν_μ, μ, c, s) and (ν_τ, τ, t, b). The L and Q_L are for the left-handed negatively charged leptons and quarks respectively, described as doublet in the SU(2) space. The e_R, u_R, d_R are for the right-handed fermions, described as singlet in the SU(2) space. There is no experimental evidence for right-handed neutrinoes in the nature.

The $U(1)$ and $SU(2)$ terms are built to describe the electromagnetic force and the weak force, respectively. The W^i are converted to states $W^{\pm}_{\mu}, W^0_{\mu}$, and the $W^{\pm}_{\mu}$ are identified as the physical weak force carriers which allow $u_L \leftrightarrow d_L$ and $\nu_e \leftrightarrow e^-$. To connect the vector fields B_μ and W^0_μ to the observed photon (γ) and Z^0, two requirements regarding the handedness (parity property) of fermions need to be satisfied. The electromagnetic interaction conserves the parity, while only the left-handed fermions contribute to the weak force. The two constraints are accommodated by combining and redefining the fields as:

$$\begin{aligned} A_\mu &= \frac{g_2 B_\mu - g_1 Y_L W^0_\mu}{\sqrt{(g_2^2 + g_1^2 Y_L^2)}} \\ Z_\mu &= \frac{g_1 Y_L B_\mu + g_2 W^0_\mu}{\sqrt{(g_2^2 + g_1^2 Y_L^2)}}. \end{aligned} \tag{1.5}$$

In this way the electromagnetic force and the weak force are unified as the electroweak force. An additional photon-like neutral current Z_μ is introduced to mediate the electroweak force between any two charged fermions. The classical electric charge can be defined from $U(1)$ gauge invariance through the $Noether's\, theorem$ [5], which states that any continuous symmetry which leaves the action $\int \mathcal{L}$ invariant leads to a conserved current S_μ, with $\partial^\mu S_\mu = 0$. It is always possible to define a charge $Q(t) = \int d^3x S_0(x)$.

The SU(3) terms describe the strong interactions by Quantum Chromodynamics (QCD). Quarks are labeled with an additional property, referred to as color charge, namely $red, blue, green$. The color charge originates from strong interaction Lagrangian the same way as the electric charge arises from the electromagnetic interaction Lagrangian. Leptons are colorless, thus do not participate in the strong force. The eight gluons G^a interact with the quarks in a similar way as the photons interact with the electrons. However, unlike the electrically neutral photons, the gluons have color charge and interact with each other. The QCD coupling constant has the so-called asymptotic freedom feature. It decreases dramatically as the energy increases.

The mass terms on the other hand cannot be easily defined as $m\bar{\psi}\psi$ to satisfy all the gauge invariance. In fact, it is mathematically proven that the only way to satisfy the $SU(2) \times U(1) \times SU(3)$ invariance is to set all particles massless, in sharp contradiction to nature. The Standard Model solves this problem technically (rather satisfactorily) by the $Higgs\,Mechanism$ [3,4]. It introduces a fundamental field called Higgs ϕ, described as an $SU(2)$ doublelet in the electroweak space. The Lagrangian containing the Higgs breaks the $SU(2) \times U(1)$ invariance in a very subtle way (spontaneous symmetry breaking) so that the good effects of the invariances are preserved. The Higgs field acquires mass from the vacuum potential in the $\mathcal{L}$, and generates the masses of the $W^{\pm}, Z^0$ by substitutions $\phi\partial_\mu\phi \leftrightarrow \phi\mathcal{D}_\mu\phi$. It is also possible to write $SU(2)$ gauge invariant interactions between the Higgs and fermions, which leads to the mass of fermions. However, the exact number of Higgs fields is not certain and is model dependent. None of them has been observed.

1.1.3 Discrete Symmetries and CP Violations

In the Standard Model there are three irreducible discrete symmetry operations: charge conjugation (C), parity (P) and time reversal (T). Parity and time reversal are spacetime symmetries, which send the $(t, \vec{x})$ to $(t, -\vec{x})$ and $(-t, \vec{x})$, respectively. Each particle is assigned an intrinsic parity quantum number $P = \pm 1$ to reflect its behavior under the parity transformation. The charge conjugation interchanges particles and anti-particles without changing the helicity. Thus, only the neutral particles can be the eigenstates of the charge conjugation. The combination of CP changes a particle to its anti-particle and reverses its momentum and helicity.

The Standard Model Lagrangian is assumed to be symmetric under the combination of CPT. It is found experimentally that electromagnetic and strong interactions are invariant under all three operations. In the weak interaction C and P are violated separately, as only left-handed fermions participate in the flavor changing charged process mediated by $W_\mu^\pm$. However the CP and T symmetries are good approximation. Only certain processes such as the neutral K and B meson mixing violate the CP asymmetry.

1.1.4 The CKM Quark Mixing Matrix

The quarks that participate in the electroweak interactions through the flavor changing charged currents $W_\mu^\pm$ are not the mass eigenstates. Instead, the quarks with the same charge mix with each other to produce the electroweak interaction Lagrangian. However, the cross generation mixing is experimentally known to be small. The quarks' mixing is described by the unitary Cabbibo-Kobayashi-Maskawa (CKM) matrix [6, 7], usually in the Wolfenstein parametrization [8]:

$$V_{\mathtt{CKM}} \equiv \begin{pmatrix} V_{ud} & V_{us} & V_{ub} \\ V_{cd} & V_{cs} & V_{cb} \\ V_{td} & V_{ts} & V_{tb} \end{pmatrix} \simeq \begin{pmatrix} 1-\lambda^2 & \lambda & A\lambda^3(\rho-\mathtt{i}\eta) \\ \lambda & 1-\lambda^2 & A\lambda^2 \\ A\lambda^3(1-\rho-\mathtt{i}\eta) & -A\lambda^2 & 1 \end{pmatrix},$$

where $A = 0.818^{+0.007}_{-0.017}$, $\lambda = 0.2272 \pm 0.0010$, $\rho = 0.221^{+0.064}_{-0.028}$, and $\eta = 0.340^{+0.017}_{-0.045}$, as measured by experiments.

The non-trivial phases in V_{ub} and V_{td}, referred to as weak phases, are the sources of all CP violation processes related to the weak interactions within the Standard Model. These phases are usually described by angles α, β, and γ in the so-called Unitarity Triangle, shown by Fig. 1.1. The angles α, β, and γ are defined as

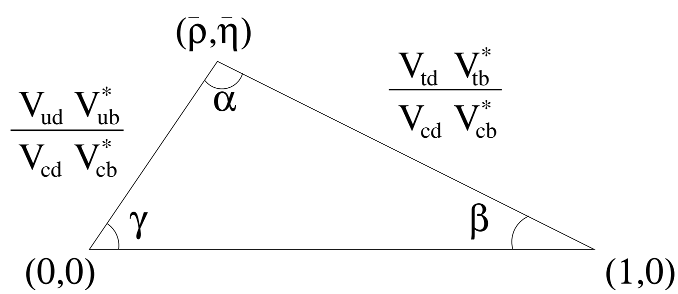

Figure 1.1: The Unitarity Triangle in the $\bar{\rho}$-$\bar{\eta}$ plane.

$$\begin{aligned} \alpha &\equiv \arg\left[-V_{\rm td}V_{\rm tb}^*/V_{\rm ud}V_{\rm ub}^*\right], \\ \beta &\equiv \arg\left[-V_{\rm cd}V_{\rm cb}^*/V_{\rm td}V_{\rm tb}^*\right], \qquad (1.6) \\ \gamma &\equiv \arg\left[-V_{\rm ud}V_{\rm ub}^*/V_{\rm cd}V_{\rm cb}^*\right] \equiv \pi - \alpha - \beta. \end{aligned}$$

These angles can be experimentally extracted from a number of B meson decays, and are the most important parameters in the understanding of CP violation processes.

1.2 The B-meson Production at BABAR

Fig. 1.2 shows the cross-section for the production of $\Upsilon(nS)$ hadrons in the e^+e^- collisions in the center-of-mass energy region near 10 GeV. The cross-section for the production of fermion pairs at the $\Upsilon(4S)$ are shown in Table 1.3. Accompanying the resonant production of B-mesons is the so-called continuum physics of roughly 2.5 nb of cross section. It consists of the e^+e^- annihilation into quark pairs ($u\bar{u}$, $d\bar{d}$, $s\bar{s}$, $c\bar{c}$) and lepton pairs (e^+e^-, $\mu^+\mu^-$, $\tau^+\tau^-$). The light quark (u , d , s) and lepton (e, μ) events are less interesting, and used primarily for the normalization of the experiment.

Table 1.3: Production cross-section at $\sqrt{s} = M(\Upsilon(4S))$. The e^+e^- cross-section is the effective cross-section, expected with the experimental acceptance.

$e^+e^- \rightarrow$	$b\bar{b}$	$c\bar{c}$	$s\bar{s}$	$u\bar{u}$	$d\bar{d}$	$\tau^+\tau^-$	$\mu^+\mu^-$	e^+e^-
Cross-section (nb)	1.05	1.30	0.35	1.39	0.35	0.94	1.16	40

The $\Upsilon(4S)$ resonance decays almost exclusively to pairs of B-mesons with the following features.

- Since the $\Upsilon(4S)$ decays to only two particles, the daughter $B\overline{B}$ mesons have a unique momentum in the $\Upsilon(4S)$ center-of-mass frame. In addition, the fraction of all events

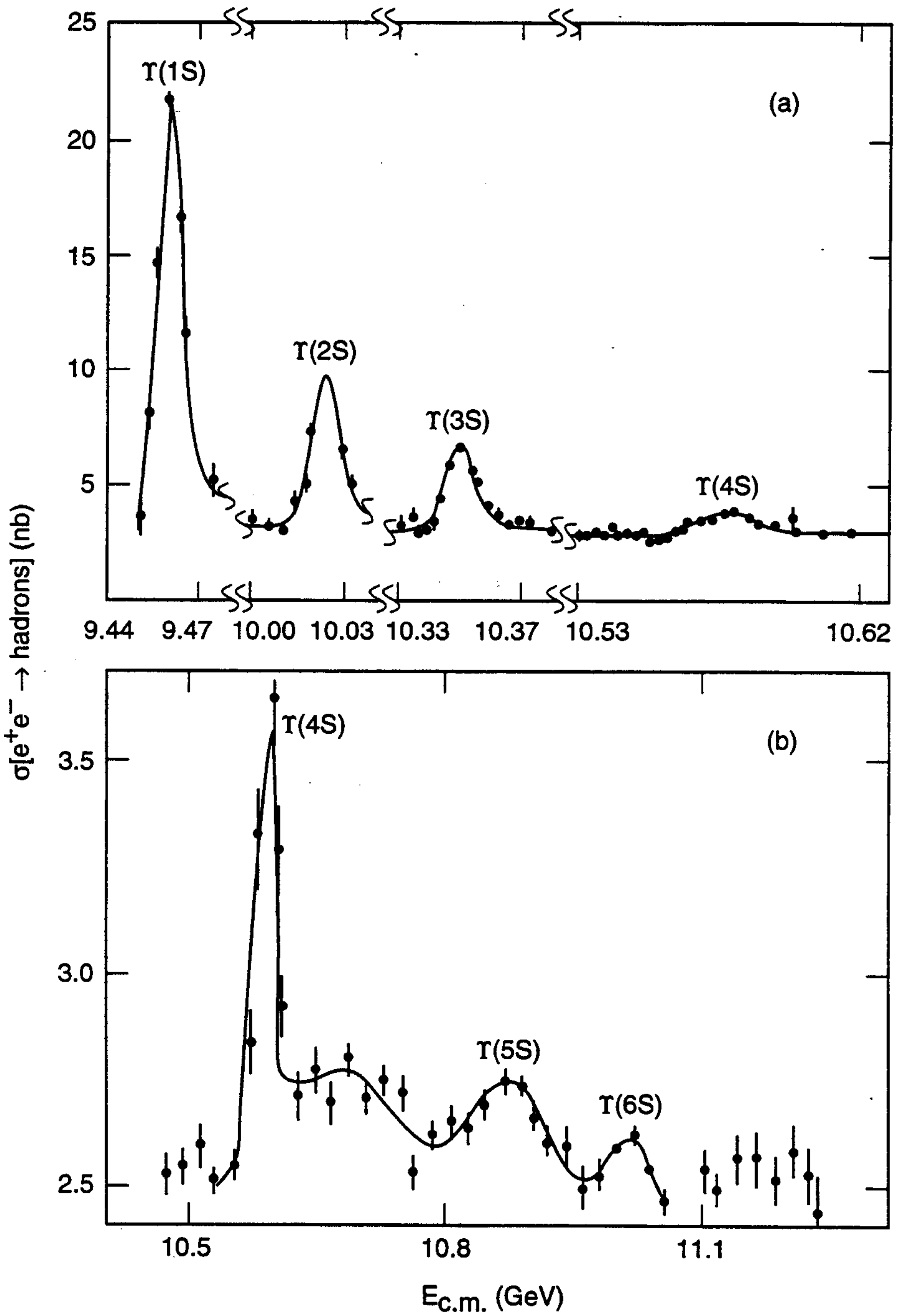

Figure 1.2: The cross section for the production of hadrons in e^+e^- collisions in the center-of-mass energy region near 10 GeV. The data are characterized by a series of resonances, the Υ family, which herald the onset of the b quark threshold. The data in (a) are from the CUSB detector group; the data in (b) are from the CLEO detector group.

that contain a $B\overline{B}$ pair is 30%, significantly greater than at higher energies or in proton collisions. These two effects greatly limit contamination from continuum backgrounds (non-b quarks) that accompany the $\Upsilon(4S)$.

- When the $\Upsilon(4S)$ decays, the $B\overline{B}$ are coherently produced in a P-wave state, resulting two nonidentical B mesons. One is a B^0/B^- and the other is a $\overline{B}^0/B^+$. This feature is particularly advantageous for CP violation studies.

- The multiplicity of hadrons in the $\Upsilon(4S)$ decay is relatively small, which keeps combinatorial backgrounds at a reasonable level in the B meson reconstruction.

1.3 The Gluonic Penguin Decays $B \to \varphi K^*$

The B-mesons decay dominantly through flavor changing charged current $b \to c\,W^-$, as indicated by the CKM matrix diagonal element V_{cb} [6, 7]. The charmless B-meson decays to the final states without charm quarks provide abundant source of events to measure the other CKM matrix elements (such as V_{ub}), and to search for phenomena outside the SM, including charged Higgs bosons and SUSY particles [9, 10].

Among the many charmless B-decays, the rare gluonic penguin decay $B \to \varphi K^*(892)$ through the $b \to s$ flavor changing neutral current (FCNC) is particularly of interest for several reasons. Within the SM the $B \to \varphi K^*$ decay is dominated by the pure QCD penguin diagram shown in Fig. 1.3, followed by strong decays $\varphi \to K^+K^-$ and $K^* \to K\pi$.

Without the pollution from a tree level process, the CP violation effects in this decay are expected to be suppressed in the SM. The $b \to ss\bar{s}$ transition is sensitive to contributions from beyond the SM, as the new physics (NP) particles at higher energy level may contribute off-shell in the loop. The vector-vector decay $B \to \varphi K^*$ also enables rich angular analysis. Many parameters sensitive to both the SM and NP interactions can be studied.

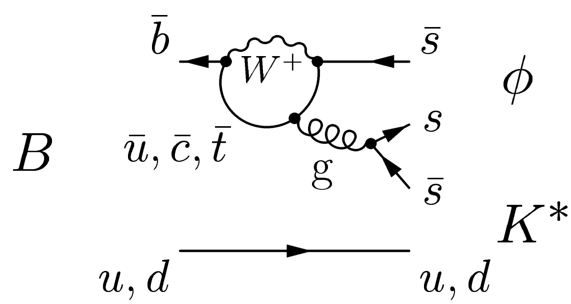

Figure 1.3: Penguin (loop) diagram describing the decays $B \to \varphi K^*$.

1.3.1 Polarization Puzzle

The first experimental evidence for $B \to \phi K^*(892)$ was provided by the CLEO [11] and *BABAR* [12] experiments. Furthermore, an interesting effect known as the polarization puzzle [13–15] has been observed in this decay. It reveals a large discrepancy between the measured polarization and the naive SM prediction has been observed in this decay.

The momentum and angular momentum conservation in the decay $B \to \varphi K^*(892)$ indicates that φ and $K^*(892)$ have the same helicity $\lambda \equiv \vec{S} \cdot \hat{p} = \pm 1, 0$. The decay amplitude is thus the sum of three complex helicity amplitudes, one longitudinal A_0 and two transverse A_{+1} and A_{-1}. The longitudinal polarization is defined as $f_L = |A_0|^2/\Sigma|A_\lambda|^2$ and the two transverse amplitudes can be rewritten in terms of the CP-even amplitude $A_\parallel = (A_{+1} + A_{-1})/\sqrt{2}$ and CP-odd amplitude $A_\perp = (A_{+1} - A_{-1})/\sqrt{2}$. Accordingly, the total and CP-odd transverse polarizations are defined as $f_T = 1 - f_L$ and $f_\perp = |A_\perp|^2/\Sigma|A_\lambda|^2$.

From naive SM factorization, the transverse amplitudes $A_\parallel$ and $A_\perp$ are suppressed by factors of m_φ/m_B and m_φ^2/m_B^2 respectively compared to the longitudinal amplitude A_0. This amplitude hierarchy can be understood intuitively (see Sec. 1.3.2 for more) from two constraints in the SM, the (V-A) structure in the weak interaction sector and the helicity conservation in the strong interaction sector. The (V-A) structure indicates that only left-handed or right-handed quarks or anti-quarks contribute in the $b \to s$ or $\bar{b} \to \bar{s}$ weak interaction, shown in Fig. 1.3. The helicity conservation in strong interaction sector suggests that the $s\bar{s}$ pairs emitted from the hard gluon bear opposite helicities. Considering both constraints, it is obvious that A_0 amplitude dominates. The A_{+1} and A_{-1} amplitudes suppressions can be obtained in the helicity flip framework [17].

The amplitudes hierarchy $A_0 \gg A_{+1} \gg A_{-1}$ predicted by the naive SM factorization puts $f_L \approx 1$ for the decay $B \to \varphi K^*(892)$. In contrast, f_L was measured as $0.52 \pm 0.05 \pm 0.02$ [15]. The discrepancy between the SM predication and experimental measurement in f_L has become known as the "polarization puzzle". It has raised a lot of interest among both the experimental and theoretical particle physics community. The

SM predicted longitudinal dominance was confirmed experimentally for the SU(3) related vector-vector decays $B \to \rho\rho$ and ρK^* [18, 19], which proceed through dominant $b \to d$ penguin loops and CKM suppressed tree processes ($B^+ \to \rho^+ K^{*0}$ is pure penguin). The theoretical efforts are summarized in the next section.

1.3.2 Theoretical Approaches

The polarization puzzle in the decay $B \to \varphi K^*(892)$ has motivated a number of proposed contributions from the NP [20–28] beyond the SM. On the other hand, there are some explanations within the SM based on new mechanisms, such as the penguin annihilation [17, 29–34], electroweak penguin [35] and QCD rescattering [36–39]. The naive and QCD factorization of SM prediction and the NP effects are to be discussed below.

To understand the QCD effects in hadronic B-decays quantitatively, two useful tools from quantum field theory are usually employed, the operator product expansion (OPE) [40] and the renormalization group [42–47]. In the OPE, the SM low-energy effective Hamiltonian for the pure penguin $b \to ss\bar{s}$ [50] transition can be written as

$$H^s_{eff} = -\frac{G_F}{\sqrt{2}} \sum_{i=3}^{10} (V_{ub}V^*_{us}c^u_i + V_{cb}V^*_{cs}c^c_i + V_{tb}V^*_{ts}c^t_i)\mathcal{O}^s_i + h.c., \tag{1.7}$$

where the superscript u, c, t indicates the quark which is internal or involved in the penguin loop. The c_i are Wilson coefficients and the $\mathcal{O}_i$ are the local operators shown by Eq. (1.8). Both the c_i and $\mathcal{O}_i$ depend on the QCD renormalization scale μ. The c_i depend on the mass of the $W^{\pm}$ bosons and other heavy particles such as the t and b quarks. The $\mathcal{O}_{3-6}$ are the strong gluon-induced penguin operators. The $\mathcal{O}_{7-10}$ are due to the γ and Z^0 exchange (electroweak penguins) and "box" diagrams at loop level.

$$\begin{aligned}
\mathcal{O}_3 &= (\bar{s}_\alpha b_\alpha)_{V-A} \sum_q (\bar{q}_\beta q_\beta)_{V-A} \\
\mathcal{O}_4 &= (\bar{s}_\alpha b_\beta)_{V-A} \sum_q (\bar{q}_\beta q_\alpha)_{V-A} \\
\mathcal{O}_5 &= (\bar{s}_\alpha b_\alpha)_{V-A} \sum_q (\bar{q}_\beta q_\beta)_{V+A} \\
\mathcal{O}_6 &= (\bar{s}_\alpha b_\beta)_{V-A} \sum_q (\bar{q}_\beta q_\alpha)_{V+A} \\
\mathcal{O}_7 &= \frac{3}{2}(\bar{s}_\alpha b_\alpha)_{V-A} \sum_q e_q (\bar{q}_\beta q_\beta)_{V+A} \\
\mathcal{O}_8 &= \frac{3}{2}(\bar{s}_\alpha b_\beta)_{V-A} \sum_q e_q (\bar{q}_\beta q_\alpha)_{V+A} \\
\mathcal{O}_9 &= \frac{3}{2}(\bar{s}_\alpha b_\alpha)_{V-A} \sum_q e_q (\bar{q}_\beta q_\beta)_{V-A} \\
\mathcal{O}_{10} &= \frac{3}{2}(\bar{s}_\alpha b_\beta)_{V-A} \sum_q e_q (\bar{q}_\beta q_\alpha)_{V-A} \qquad (1.8)
\end{aligned}$$

Within the naive SM factorization, the decay amplitude can be written as [48]

$$A[B \to \varphi K^*] = \frac{G_F}{\sqrt{2}} X P_\varphi \; , \qquad (1.9)$$

with

$$\begin{aligned}
X &= -\sum_{q=u,c,t} V_{qb}^* V_{qs} \times \left[a_3^q + a_4^q + a_5^q - \frac{1}{2}(a_7^q + a_9^q + a_{10}^q) \right] \; , \\
P_\varphi &= \texttt{decay constant} \times \texttt{form factor} \qquad (1.10) \\
&= \langle \varphi | \bar{s} \gamma^\mu s | 0 \rangle \langle K^* | \bar{b} \gamma_\mu (1-\gamma_5) s | B \rangle = m_\varphi g_\varphi \eta_\varphi^{*\mu} \langle K^* | \bar{b} \gamma_\mu (1-\gamma_5) s | B \rangle ,
\end{aligned}$$

where a_i are the combinations of Wilson Coefficiencies

$$a_i = \begin{cases} c_i + c_{i-1}/N_c \ , & i \text{ even } \ , \\ c_i + c_{i+1}/N_c \ , & i \text{ odd } \ . \end{cases} \tag{1.11}$$

The quantities m_φ, g_φ and $\eta_\varphi^{*\mu}$ represent the mass, decay constant and the polarization four-vector of the φ meson. The polarization amplitudes are then given by

$$\begin{aligned} A_0 &\approx \frac{G_F}{\sqrt{2}} 2 m_B m_\varphi g_\varphi X \sqrt{\frac{2}{3}} \left[\left(\widetilde{A}_1 - \widetilde{A}_2 \right) \right. \\ &\quad + \left. \frac{m_{K^*}}{m_B} \left(\widetilde{A}_1 + \widetilde{A}_2 \right) \right] \frac{m_B^2}{4 m_\varphi m_{K^*}} \ , \\ A_\parallel &\approx -\frac{G_F}{\sqrt{2}} \sqrt{2} m_B \frac{1}{\sqrt{2}} \left[m_\varphi g_\varphi \left(1 + \frac{m_{K^*}}{m_B} \right) \widetilde{A}_1 X \right] \ , \\ A_\perp &\approx -\frac{G_F}{\sqrt{2}} \sqrt{2} m_B \frac{1}{\sqrt{2}} \left[m_\varphi g_\varphi \left(1 - \frac{m_{K^*}}{m_B} \right) \widetilde{V} X \right] \ , \end{aligned} \tag{1.12}$$

where $\widetilde{A}_1$, $\widetilde{A}_2$ and $\widetilde{V}$ are $B \to K^*$ form factors. In the large energy limit $(\Lambda_{QCD}, m_{\varphi,K^*}) \ll m_B)$, these form factors can be expressed in terms of two universal form factors [41]. The relative magnitudes between the two universal form factors are uncertain in the QCDf and shown crucial to explain the polarization puzzle. The polarization fractions satisfy $1 - f_L = O(1/m_b^2), f_\perp/f_\parallel = 1 + O(1/m_b)$ indicating the hierarchy $A_0 \gg A_{+1} \gg A_{-1}$.

Electroweak penguin contribution to the $B \to \varphi K^*$ decay is color suppressed. An enhanced electromagnetic penguin contribution is proposed in Ref. [35] to explain the polarization puzzle in the same $b \to s$ penguin dominated decay $B \to \rho^0 K^*$. However, it only lowers the f_L of $B \to \varphi K^*(892)$ by 0.05, not enough to account for the large transverse amplitude observed in $B \to \varphi K^*(892)$ decay.

Beyond the naive factorization, several models based on SM QCD factorization (QCDf) [36–39] are also proposed. Assuming that there is a single explanation for the large transverse amplitude, there are two plausible SM QCDf solutions, penguin annihilation [17] and rescattering [36–39].

Ref. [17] shows that the longitudinal dominance persists formally in the QCDf. However, the contributions of QCD penguin annihilation (illustrated by Fig. 1.4) that are formally power suppressed in the $1/m_b$ expansion can be numerically tuned to be the order $O(1)$. In this case, the observed large transverse amplitudes can be accommodated with large theoretical uncertainties, such as those from the CKM matrix elements, decay constants and transition form factors. Besides, in QCDf the penguin annihilation is not calculable due to the divergences parameterized in terms of unknown parameters, that depend on the K^* final-state wave function. It is interesting to extend the polarization measurements to other K^* spin resonances, such as tensor $K_2^*(1430)$ and axial-vector $K_1(1270)$.

The other SM solution is based on the existence of large nonperturbative SM rescattering (see Fig. 1.5) contributions that are not suppressed by $O(1/m_b)$ [36–39]. It has been suggested that rescattering effects involving charm intermediate states can produce large transverse polarization f_T in $B \to \varphi K^*$. A particular realization of this scenario is [37,39] to consider the decay $B^+ \to D_s^{*+}\overline{D}^{*0}$, generated by the operator $\bar{b}\mathcal{O}'c\bar{c}\mathcal{O}'s$. Since the final-state vector mesons D_s^{*+} and $\overline{D}^{*0}$ are heavy, the transverse polarization can be large. The state $D_s^{*+}\bar{D}^{*0}$ can rescatter to $\varphi K^*(892)^+$. If the f_T is reduced in the scattering process,

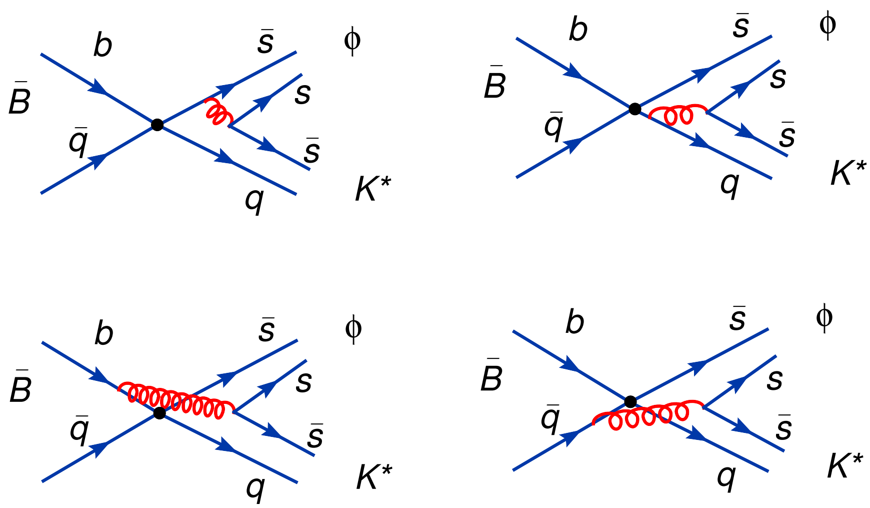

Figure 1.4: The penguin annihilation diagrams.

this will lead to large f_T/f_L in $B^+ \to \varphi K^*(892)^+$ (A similar rescattering effect can take place for $B^0 \to \varphi K^*(892)^0$.) These proposals are viable but not convincing, as the rescattering calculation also depends on a set of parameters that are specific to the $K^*(892)$ final state and virtually impossible to calculate within QCDf.

The NP contributions are only considered assuming that the naive SM predictions are generally correct but their extensions in the SM such as penguin annihilation and rescattering are not satisfactory. There have been several hints of such NP scenarios in the $b \to s$ FCNC, such as right-handed currents [17, 20, 21], scalar or tensor couplings [22, 23], R-parity violating SUSY [24, 25], nonuniversal Z' couplings [26] and generalized four quark operators [27, 28]. Just as the SM QCD attempts, some of the NP predictions accommodate

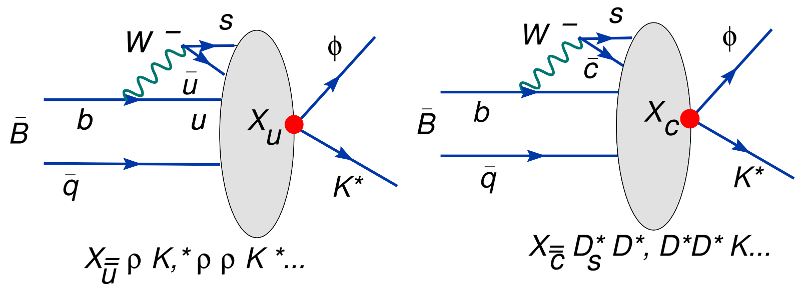

Figure 1.5: The rescattering diagrams.

the experimental findings, and some others do not. However, as the NP mechanism itself is not clear and the hadronic matrix elements of the new operators in NP are subject to similar QCD uncertainties, none of these NP predictions is conclusive. On the other hand, if one or some processes reflected true NP, similar effects would be seen in other decays $B \to \varphi K_J^*$.

For example, right-handed currents [17, 20, 21] generated by $\bar{s}\gamma_\mu(1+\gamma_5)b\bar{s}\gamma^\mu(1\pm\gamma^5)s$ contribute constructively to the CP-odd amplitude $A_\perp$, while destructively to the CP-even amplitude $A_{\|,0}$. It leads to the distinct polarization signature $f_\perp \gg f_\|$, in contradiction to the experimental finding $f_\perp = 0.22 \pm 0.05 \pm 0.02 \approx f_\|$ [15].

Another example considers tree level scalar interactions [22] $b \to sH \to ss\bar{s}$ in a generalized Higgs doublet model. The Higgs coupling to a flavor changing current between two down-type quarks is estimated as $\xi_{ij} = \lambda_{ij}\sqrt{m_i m_j}/v$ using the ansatz [51, 52] . It has been analyzed phenomenologically that the coupling λ_{sb} for $b \to sH$ transition could be as large as $O(10)$ [52]. The coupling λ_{ss} for $H \to s\bar{s}$ can be order of $\tan\beta \sim m_t/m_b$ in the type II Higgs-doublet model due to the potential enhancement in $\tan\beta$. The scalar interaction calculation depends on unknown parameters such as $\zeta = \lambda_{bs}/\lambda_{sb}$. With various ζ assumptions, a set of predictions on the polarizations and branching fractions can be made and the large f_T can be realized numerically.

To summarize, there are many mechanisms proposed to resolve the polarization anomaly observed in $B \to \varphi K^*$, both within and beyond the SM. However, none of them is conclusive or satisfactory. They are all model and parameter dependent and their predications are associated with large theoretical uncertainties from the complicated QCD dynamics. Therefore, to distinguish these models and help resolve the polarization puzzle, it is necessary to extend the polarization study on $B \to \varphi K^*(892)$ to other K^* final states.

1.3.3 New Search Window

To provide input to resolve the polarization puzzle in $B \to \varphi K^*(892)$, several amplitude and angular analyses on decays $B \to \varphi K_J^{(*)}$, including the $K_J^{(*)}$ mesons listed in Table 1.4 are performed. The J refers to the spin of the $K\pi(\pi)$ system. For $J \neq 0$, the decay amplitudes for $B^0 \to \varphi K_J^{*0}$ or $B^+ \to \varphi K_J^{(*)+}$ and $\overline{B}^0 \to \varphi \overline{K}_J^{*0}$ or $B^- \to \varphi K_J^{(*)-}$ decays are sums of complex amplitudes $A_{J\lambda}$ and $\overline{A}_{J\lambda}$, respectively. The $\lambda = \pm 1,\, 0$ is the spin projection of the φ meson onto the direction opposite to the B meson flight direction in the φ rest frame. The CP −even and CP −odd amplitudes $A_{\| J}$ and $A_{\perp J}$ can be transformed from $A_{J\pm 1} = (A_{J\|} \pm A_{J\perp})/\sqrt{2}$.

The branching fraction polarization parameters, strong phases and CP asymmetries can

Table 1.4: Summary of $K\pi(\pi)$ resonances and $\overline{D}^0$ meson described in this thesis, with the mean and width taken from PDG [56].

Resonance	J^P	Mean (MeV)	Width (MeV)
$K_0^*(1430)$	0^+	1425 ± 50	270 ± 80
$K^*(892)^0$	1^-	896.00 ± 0.25	50.3 ± 0.6
$K^*(892)^+$	1^-	891.66 ± 0.26	50.8 ± 0.9
$K^*(1410)^+$	1^-	1414 ± 15	232 ± 21
$K^*(1680)^0$	1^-	1717 ± 27	322 ± 110
$K_1(1270)^+$	1^+	1272 ± 7	90 ± 20
$K_1(1400)^+$	1^+	1403 ± 7	174 ± 13
$K_2^*(1430)^0$	2^+	1432.4 ± 1.3	109 ± 5
$K_2^*(1430)^+$	2^+	1425.6 ± 1.5	98.5 ± 2.7
$K_2(1770)^+$	2^-	1773 ± 8	186 ± 14
$K_2(1820)^+$	2^-	1816 ± 13	276 ± 35
$K_3^*(1780)^0$	3^-	1776 ± 7	159 ± 21
$K_4^*(2045)^0$	4^+	2045 ± 9	198 ± 30
$\overline{D}^0$	0^+	1864.5 ± 0.4	1.6×10^{-9}

be measured for each decay mode. They can be expressed as six CP-averaged and six CP-violating parameters, as summarized in Table 1.5. The π in the definitions of $\phi_{\perp J}$ and $\Delta\phi_{\perp J}$ accounts for the sign flip $A_{\perp J} = -\overline{A}_{\perp J}$ if CP is conserved. The phases δ_{0J} are extracted from the interference (see Sec. 3.3) between decays $B \to \varphi K_J^{(*)}$ and $\varphi K_0^*(1430)$.

The parameterization in Table 1.5 is motivated by the negligible CP violation expected in these decays. Therefore, the polarization parameters specific to either B (superscript "$-$") or $\overline{B}$ (superscript "$+$") are the CP-averaged parameters with small CP-violating corrections which are either multiplicative (for rates) or additive (for phases):

$$\mathcal{B}_J^{\pm} = \mathcal{B}_J \cdot (1 \pm \mathcal{A}_{CPJ})/2 \tag{1.13}$$

$$f_{LJ}^{\pm} = f_{LJ} \cdot (1 \pm \mathcal{A}_{CPJ}^{0}) \tag{1.14}$$

$$f_{\perp J}^{\pm} = f_{\perp J} \cdot (1 \pm \mathcal{A}_{CPJ}^{\perp}) \tag{1.15}$$

$$\phi_{\parallel J}^{\pm} = \phi_{\parallel J} \pm \Delta\phi_{\parallel J} \tag{1.16}$$

$$\phi_{\perp J}^{\pm} = \phi_{\perp J} \pm \Delta\phi_{\perp J} + \frac{\pi}{2} \pm \frac{\pi}{2} \tag{1.17}$$

$$\delta_{0J}^{\pm} = \delta_{0J} \pm \Delta\delta_{0J}. \tag{1.18}$$

All quantities in Eq. (1.13-1.18) are expected to be negligible in the SM with a single dominant penguin contribution in the decay amplitude. However, new particles in the penguin loops, such as charged Higgs or SUSY particles, may introduce additional phases and asymmetries between the B and $\overline{B}$ decay amplitudes.

Meanwhile, the SM highly suppressed decay $B^0 \to \varphi\overline{D}^0$ can also be studied in the same final states as decays $B^0 \to \varphi(K^+\pi^-)$. An annihilation diagram with external OZI-

Table 1.5: Definitions of real parameters measurable with the $B^0 \to \varphi K_J^{(*)}$ decays. The branching fraction $\mathcal{B}$ is calculated as a ratio of the average partial decay widths for B^0 (Γ) and $\overline{B}^0$ ($\bar{\Gamma}$) and the total width Γ_{total}, where any difference in the B^0 and $\overline{B}^0$ widths is neglected. This definition allows for differences between the B and $\overline{B}$ decay amplitudes, $A_{J\lambda}$ and $\overline{A}_{J\lambda}$, as discussed in the text. For those decay modes with limited statistics, not all of these measurements are feasible, such as the CP asymmetries. The detail of the results are given in section. 4.1.

	CP −Averaged Parameters
$\mathcal{B}_J$	$\frac{1}{2}(\bar{\Gamma}_J + \Gamma_J)/\Gamma_{\text{total}}$
f_{LJ}	$\frac{1}{2}(\lvert\overline{A}_{J0}\rvert^2/\Sigma\lvert\overline{A}_{J\lambda}\rvert^2 + \lvert A_{J0}\rvert^2/\Sigma\lvert A_{J\lambda}\rvert^2)$
$f_{\perp J}$	$\frac{1}{2}(\lvert\overline{A}_{J\perp}\rvert^2/\Sigma\lvert\overline{A}_{J\lambda}\rvert^2 + \lvert A_{J\perp}\rvert^2/\Sigma\lvert A_{J\lambda}\rvert^2)$
$\phi_{\parallel J}$	$\frac{1}{2}(\arg(\overline{A}_{J\parallel}/\overline{A}_{J0}) + \arg(A_{J\parallel}/A_{J0}))$
$\phi_{\perp J}$	$\frac{1}{2}(\arg(\overline{A}_{J\perp}/\overline{A}_{J0}) + \arg(A_{J\perp}/A_{J0}) - \pi)$
δ_{0J}	$\frac{1}{2}(\arg(\overline{A}_{00}/\overline{A}_{J0}) + \arg(A_{00}/A_{J0}))$
	CP −violating Parameters
$\mathcal{A}_{CPJ}$	$(\bar{\Gamma}_J - \Gamma_J)/(\bar{\Gamma}_J + \Gamma_J)$
$\mathcal{A}_{CPJ}^0$	$(\lvert\overline{A}_{J0}\rvert^2/\Sigma\lvert\overline{A}_{J\lambda}\rvert^2 - \lvert A_{J0}\rvert^2/\Sigma\lvert A_{J\lambda}\rvert^2)/(\lvert\overline{A}_{J0}\rvert^2/\Sigma\lvert\overline{A}_{J\lambda}\rvert^2 + \lvert A_{J0}\rvert^2/\Sigma\lvert A_{J\lambda}\rvert^2)$
$\mathcal{A}_{CPJ}^\perp$	$(\lvert\overline{A}_{J\perp}\rvert^2/\Sigma\lvert\overline{A}_{J\lambda}\rvert^2 - \lvert A_{J\perp}\rvert^2/\Sigma\lvert A_{J\lambda}\rvert^2)/(\lvert\overline{A}_{J\perp}\rvert^2/\Sigma\lvert\overline{A}_{J\lambda}\rvert^2 + \lvert A_{J\perp}\rvert^2/\Sigma\lvert A_{J\lambda}\rvert^2)$
$\Delta\phi_{\parallel J}$	$\frac{1}{2}(\arg(\overline{A}_{J\parallel}/\overline{A}_{J0}) - \arg(A_{J\parallel}/A_{J0}))$
$\Delta\phi_{\perp J}$	$\frac{1}{2}(\arg(\overline{A}_{J\perp}/\overline{A}_{J0}) - \arg(A_{J\perp}/A_{J0}) - \pi)$
$\Delta\delta_{0J}$	$\frac{1}{2}(\arg(\overline{A}_{00}/\overline{A}_{J0}) - \arg(A_{00}/A_{J0}))$

suppressed φ production is required, such as the quark diagrams in Fig. 1.6.

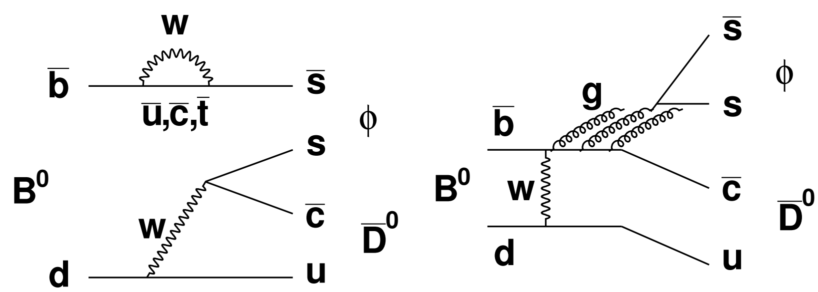

Figure 1.6: Quark diagrams for decays $B \to \overline{D}\varphi$.

In a summary, decays $B \to \varphi K_J^{(*)}$ are analyzed in four regions:

- Decays $B^0 \to \varphi K_J^{*0}(K^+\pi^-)$ in the $K\pi$ mass range (1.13 - 1.53 GeV), with two $(K\pi)$ resonances, tensor $K_2^*(1430)$ (2^+) and scalar $K_0^*(1430)$ (0^+).

- Decays $B^0 \to \varphi K_J^{*0}(K^+\pi^-)$ and $B^0 \to \varphi \overline{D}^0 \to (K^+K^-)(K^+\pi^-)$ in the $K\pi$ mass range (1.60 - 2.15 GeV), with four $(K\pi)$ resonances, scalar $\overline{D}^0$ (0^+), vector $K^*(1680)$ (1^-), and tensors $K_3^*(1780)$ (3^-) and $K_4^*(2045)$ (4^+).

- Decays $B^\pm \to \varphi K_J^\pm(K^+\pi^+\pi^-)$ in the $K\pi\pi$ mass range (1.10 - 2.15 GeV), with six $(K\pi\pi)$ resonances, vector $K^*(1410)$ (1^-), axial-vectors $K_1(1270)$ (1^+) and $K_1(1400)$ (1^+), and tensors $K_2^*(1430)$ (2^+), $K_2(1770)$ (2^-) and $K_2(1820)$ (2^-).

- Decays $B^\pm \to \varphi K_J^{*\pm}(K_S^0\pi^+/K^+\pi^0)$ in in the $K\pi$ mass range (1.10 - 1.60 GeV), with two $(K\pi)$ resonances, tensor $K_2^*(1430)$ and scalar $K_0^*(1430)$.

Chapter 2

The *BABAR* Experiment

The *BABAR* Experiment is a high energy experiment based on the *BABAR* high energy particle detector operating at the Positron Electron Project II (PEP-II) e^+e^- collider at the Stanford Linear Accelerator Center (SLAC).

The primary goal of the *BABAR* experiment is the extensive study of CP asymmetries in the decays of neutral B mesons. In addition to this, a sensitive measurement of the CKM matrix element V_{ub} can be made, and a number of rare B meson decays (such as $B \to \varphi K\pi(\pi)$) may be measured, together enabling good constraints on fundamental parameters of the SM and limits on the physics beyond the SM. A range of other physics may also be studied, including other B physics, the physics of charm and tau leptons, and two-photon physics. These versatile physics goals are reflected in the technical designs of the accelerator and each subsystem of the *BABAR* detector, to be described in this chapter.

2.1 PEP-II Asymmetric B Factory

The electron and positron beams are accelerated to the energies of 9.0 and 3.1 GeV respectively by the 3-km long SLAC linear accelerator (LINAC). After the acceleration, the beams are then independently injected into the two 2.2-km-diameter PEP-II storage rings, high-energy ring (HER) for electrons and the low-energy ring (LER) for positrons. The beams collide head-on at interaction region 2 (IR2) of PEP-II, where the *BABAR* detector is located, as shown in Fig. 2.1.

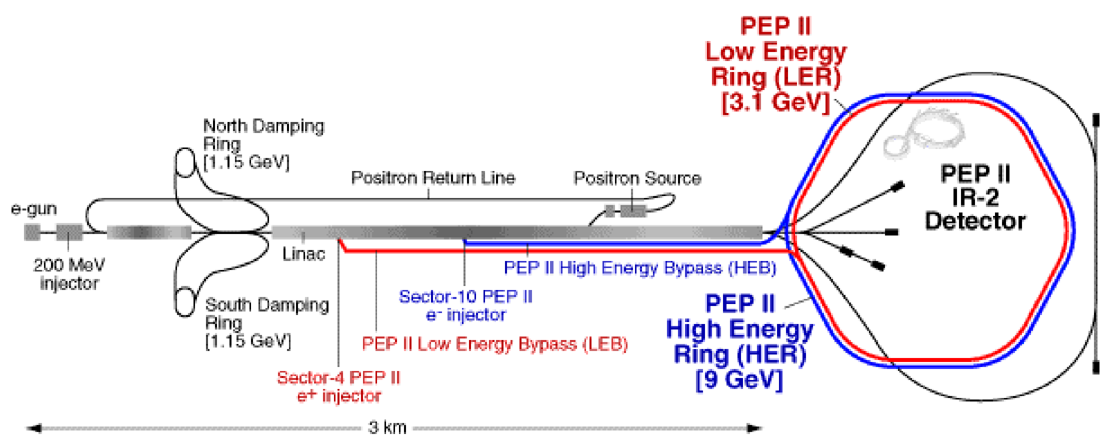

Figure 2.1: Schematic view of LINAC and PEP-II rings.

Electrons are produced by a polarized electron gun, in which polarized laser light knocks electrons off the surface of a semiconductor. They are then drawn towards the linac by an applied electric field. Part of the electron beams are diverted from the linac and collide with tungsten, producing a large number of e^+e^- pairs. The positrons are collected and sent back along a separate line to the start of the linac. Because the beams tend to spread out in the transverse directions, they are made to circulate through small storage rings called damping rings, where their transverse motion is reduced by a combination of synchrotron radiation and applied electric magnetic field. After that, the focused beams are fed back to the linac, accelerated to their desired energies, and enter the PEP-II from the beam switchyard.

The PEP-II makes use of a series of magnets to steer the beams through the storage rings. Each beam circulates in its own vacuum chamber except in the IR2. A pair of dipole magnets (B1) on each side of the e^+e^- interaction point (IP) are used to align the beams before collision and pairs of quadrapole magnets (Q1) provide final focusing in the vertical direction. Immediately after the collision, the e^+e^- beams are separated in the horizontal plane by the B1 and Q1 magnets before they return to the storage rings for the next collision.

Table 2.1 shows some important parameters of PEP-II. The most critical ones are luminosity, beam energies, and the position, angles and size of the luminous area. The high beam currents and the large number of closely-spaced bunches achieved by PEP-II produce the desired high luminosity. For the majority of the data taking, the center-of-mass energy of the e^+e^- beams is chosen as 10.58 GeV, corresponding to the mass of $\Upsilon(4S)$ resonance, which decays exclusively to pairs of B mesons ($B^0\overline{B}^0$ and B^+B^-). The kinematic constraints yield exceptionally clean isolation of the B mesons with large signal-to-background ratios. The unequal e^-e^+ beams energies result in a Lorentz boost of $\beta\gamma = 0.56$ to the $\Upsilon(4S)$. This allows us to reconstruct the displaced decay vertices of the B mesons separately, and, thus to measure the relative travel distance of the two B decays. The ability to measure this distance is crucial to measure the CP violation in B-mesons. For this reason the PEP-II collider is commonly referred as an e^-e^+ asymmetric B factory.

Table 2.1: PEP-II beam parameters. Values are given both for the design and for typical colliding beam operation in 2006. HER and LER refer to the high energy e^- and low energy e^+ beams respectively. σ_{Lx}, σ_{Ly} and σ_{Lz} refer to the horizontal, vertical and longitudinal r.m.s. size of the luminous region.

Parameters	Design	Typical
Energy HER/LER (GeV)	9.0/3.1	9.0/3.1
Current HER/LER (A)	0.75/2.15	1.7/2.9
Number of bunches	1658	1722
Bunch spacing (ns)	4.2	4.1
σ_{Lx} (μm)	3.3	2.9
σ_{Ly} (μm)	9	10
σ_{Lz} (μm)	3	10
Luminosity (10^{33}cm^{-2}s^{-1})	3	10
Luminosity (pb^{-1}/d)	135	700

The PEP-II B Factory ran from 1998 to 2008 and produced 475 million $B\overline{B}$ pairs. It was designed to operate at a luminosity of 3×10^{33}cm^{-2}s^{-1} and above. With the surpassed design *BABAR* achieved a peak luminosity of greater than $1.2 \times 10^{34}\mathrm{cm}^{-2}\mathrm{s}^{-1}$ later on. Fig. 2.2 shows the integrated PEP-II-delivered and *BABAR*-recorded luminosity over the lifetime of *BABAR* experiment. While 81% of the data is recorded at the $\Upsilon(4S)$ resonance, 6% and 2% of the data are recorded at the $\Upsilon(3S)$ and $\Upsilon(2S)$ resonance respectively. The rest of the data is taken at 40 MeV lower the resonance for background study.

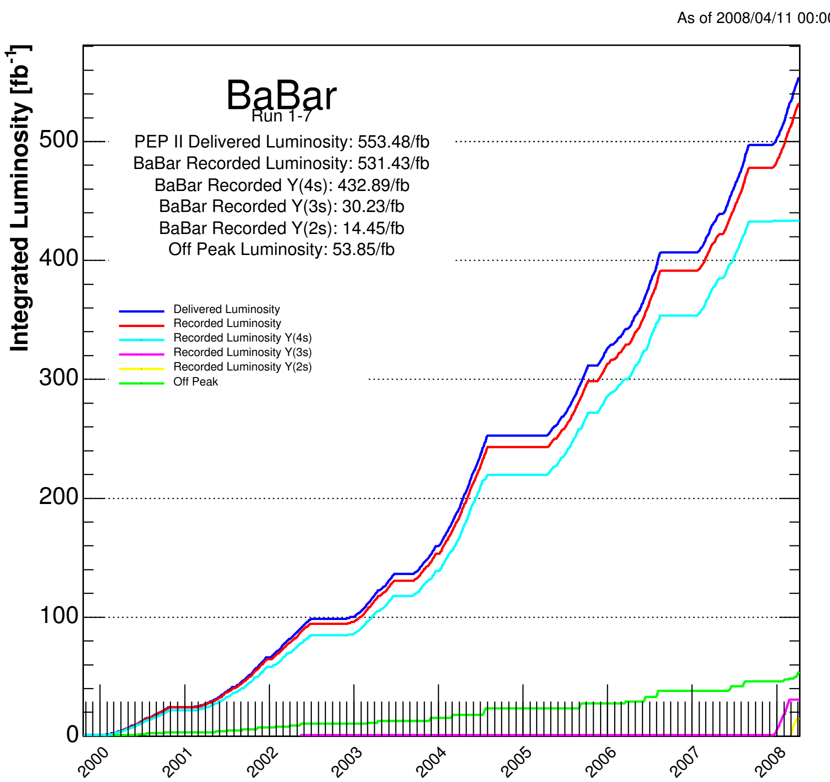

Figure 2.2: Total integrated luminosity delivered by the PEP-II and recorded by *BABAR* over the lifetime of the experiment.

2.2 The *BABAR* Detector

The *BABAR* detector operates at the IR2 of PEP-II. Fig. 2.3 shows the longitudinal section through the center and an end view with the principal dimensions. To maximize the asymmetric acceptance for the boosted $\Upsilon(4S)$ decays, the whole detector is offset relative the beam-beam IP by 0.37m in the boost direction. As indicated in the two plots, the right handed coordinate system is anchored on the main tracking system, the drift chamber, with the z-axis coinciding with its principal axis. This axis is offset relative to the beam axis by about 20 mrad in the horizontal plane. The positive y-axis points upward and the positive x-axis points away from the center of the PEP-II storage rings.

From the inside out, the *BABAR* detector consists of five subsystems: silicon vertex tracker (SVT), drift chamber (DCH), detector of internally reflected Cherenkov light system (DIRC), electromagnetic calorimeter (EMC) and instrumented flux return (IFR). The SVT, DCH, DIRC, and EMC are located inside a magnetic field of 1.5 T provided by the *BABAR* magnetic system composed of a superconducting solenoid, a segmented flux return and a field compensating or bucking coil. Each subsystem is discussed individually in the following subsections.

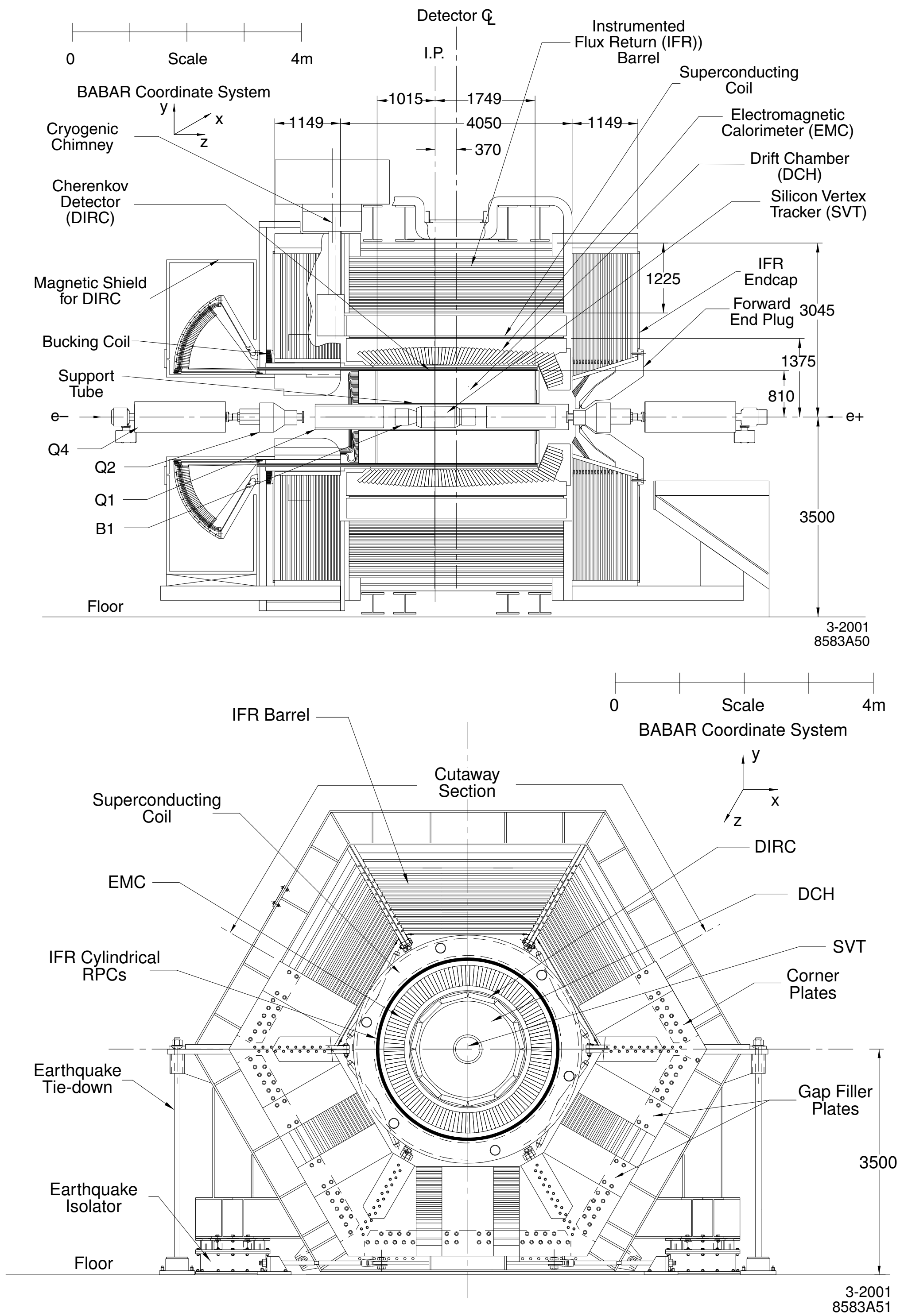

Figure 2.3: The longitudinal (top) and end (bottom) view of the *BABAR* detector.

2.2.1 The Silicon Vertex Tracker

Being the innermost layer of the *BABAR* detector, the silicon vertex tracker (SVT) is a five-layer double-sided Silicon (Si) detector. It is designed primarily to provide precise reconstruction of the charged particle trajectories and decay vertices near the IP, as required by the physics goals outlined earlier. For instance, to measure the CP violation in $\Upsilon(4S) \rightarrow B^0\overline{B}^0$, the SVT must be able to precisely measure the roughly 250 μm average separation between the B meson decay vertices. Additionally, it provides a precise measurement of track angle required to perform charge particle identification using the DIRC (see Sec. 2.2.3) and EMC (see Sec. 2.2.4) for high momentum tracks.

Mechanically, the SVT consists of 340 separate Si wafers, arranged in 5 co-axial roughly cylindrical layers, see Fig. 2.4. Each layer is divided in azimuth into between 6 and 18 modules, arranged symmetrically around the cylinder z axis. The modules in the inner three layers are tilted by 5 degrees in azimuth (ϕ), allowing an overlap region between the adjacent modules. Two types of linear implants (strips) are built on the wafer, oriented orthogonally to each other on each side, with the ϕ (z) measuring strips parallel (transverse) to the beam axis. The signals from the ϕ and z strips are routed to the electronics through the fanout circuits and then digitalized through the Front End Electronics (FEE). The digitalized signals are then transmitted to the $matching\ cards$, from where they are routed to more conventional cables. Just outside the detector, signals are $multiplexed$ by the MUX modules, converted into optical signals and transmitted to the $Readout\ Modules$ (ROMs).

The SVT is connected to the *BABAR* online detector control and monitoring system via the industry standard CAN bus.

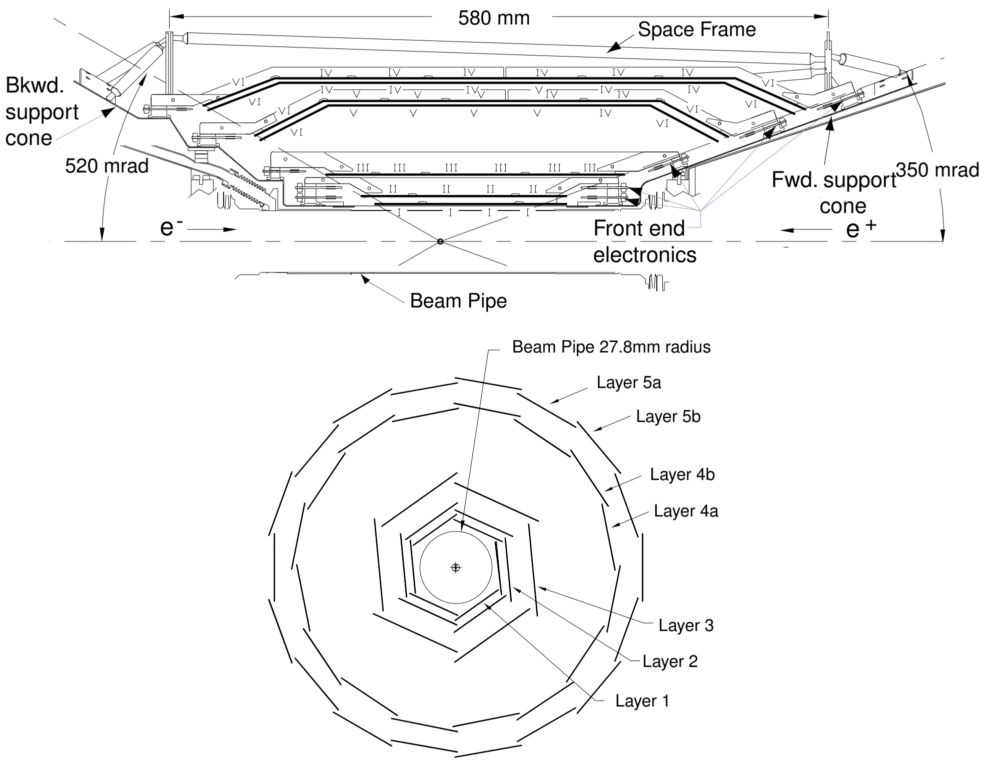

Figure 2.4: The longitudinal (top) and transverse (bottom) schematic view of SVT. The roman numbers label the six different types of sensors.

The knowledge of the relative positions and orientations of the 340 wafers is essential to the precise reconstruction of the charged tracks. Though the wafer positions can be measured accurately during the construction, they can shift due to mechanical and thermal stress during and after the detector installation. They cannot be measured using the con-

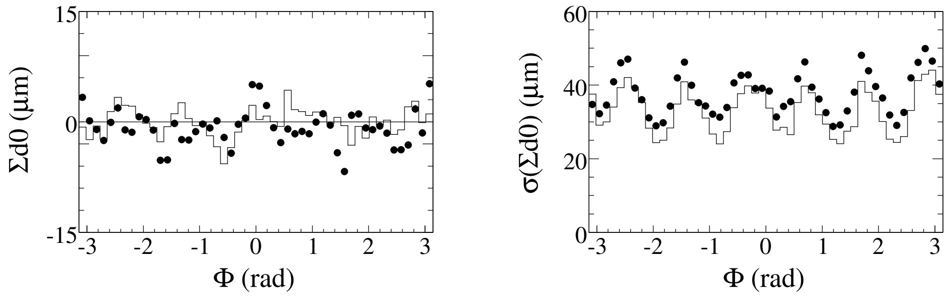

Figure 2.5: ϕ-dependence of the mean (left) and σ (right) of the $\mu^+\mu^-$ track d_0 mismatch. The *BABAR* data are shown as points, Monte Carlo simulation as histograms.

ventional survey techniques once the detector has been installed as the SVT is confined. Instead, they are determined from the SVT signal readout, through a procedure called SVT local alignment [55]. It uses the track data recorded during normal *BABAR* running, filtered and prescaled to produce a fixed sample ($e^+e^- \rightarrow e^+e^-$, $\mu^+\mu^-$ and cosmic rays) that roughly uniformly illuminates all the wafers. Track-based information is combined with direct measurements of the relative positions and orientations of Si wafers made during the construction to produce a statistically correct and systematically robust measure of the consistency (χ^2) of a wafer's position and orientation within the detector.

The performance of the SVT local alignment is validated through self-consistency tests. For example, Fig. 2.5 shows the ϕ-dependence of the $\mu^+\mu^-$ tracks transverse impact parameter d_0 mismatch on the left and its resolution on the right. The plotted points are the mean and the σ of a Gaussian fit to Σd_0 in each ϕ bin, respectively. The d_0 mean shows some structure at the level of a few microns RMS, coming from track fit biases due to dead electronics in the inner layers of the SVT, which are partially simulated in the MC. The d_0

resolution (σ) shows a periodic variation due to the six-fold symmetry of the inner layers of the SVT (see Fig. 2.4), which modulates the extrapolation of the hit error according to the distance from the innermost hit to the production point.

2.2.2 The Drift Chamber

Being right outside the SVT, the drift chamber (DCH) is the main tracking device of *BABAR*, designed to detect the charged particles and measure their momentum and angles precisely and efficiently. Measurements from the DCH complement the reconstruction and vertex measurements of the SVT for most of the charged tracks initiated from the SVT. However, for the particles that decay outside the SVT (like K_S^0), the DCH provides the sole reconstruction information. For low momentum charged particles, the DCH also supplies particle identification by measuring the ionization energy loss dE/dx with a resolution of 7%, allowing the π/K separation up to 700 MeV/c. In addition, the DCH provides one of the principal triggers (discussed in Sec. 2.3) for *BABAR*.

The DCH is a 2.8 m long cylinder, with an inner (outer) radius of 23.6 (80.9) cm, shown in Fig. 2.6. It consists of 7104 hexagonal drift cells ($1.2 \times 1.8\mathrm{cm}^2$), arranged in 40 cylindrical layers, providing 40 spatial and dE/dx measurements for charged particles with $p_T > 180$ MeV/c. The 40 layers are grouped by four into ten superlayers (see Fig. 2.7), with the same wire orientation and equal number of cells in each layer of a superlayer. Each drift cell consists of one sense wire surrounded by six field wires, with the field wires held

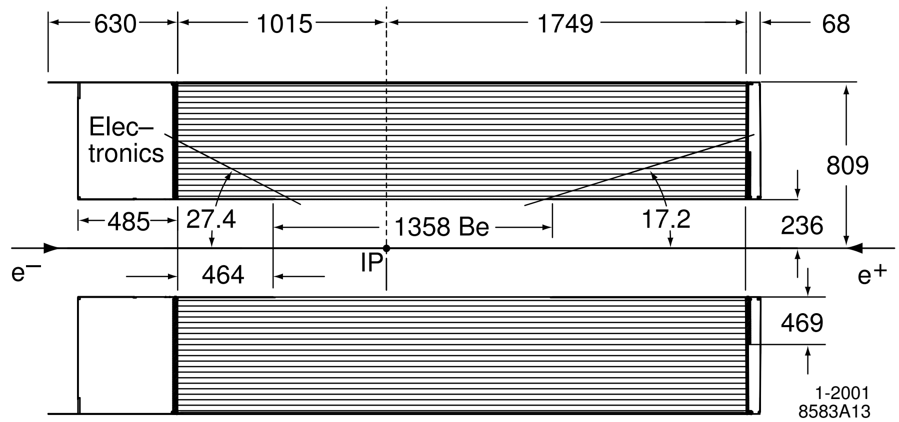

Figure 2.6: Longitudinal section of the DCH with principal dimensions (measured in mm); the chamber center is offset by 370 mm from the interaction point.

at ground potential and the sense wire subject to a positive high voltage of 1960 V at the normal operation. The cells are placed in a 5.2m^3 helium-isobutane (80:20) gas mixture. Helium is chosen to provide the most ionization per radiation length (X_0), and the isobutane chosen to absorb photons and prevent photoelectric electrons.

High energetic charged particles ionize the helium gas while transversing the DCH. The ionized electrons drift toward the sense wire under the electric field. When the $E_e > E_{\texttt{ionization}}$, a chain reaction with an avalanche gain of about 5×10^4 takes place. Electrons are collected on the wire in less than 1 ns, while the ions drift to the field wires, producing the electronic signal (voltage) to be shaped, amplified and digitalized by the DCH readout system. The calculated isochrones and drift paths for ions in adjacent cells of layer 3 and 4 of an axial superlayer are presented in Fig. 2.8. The position measurement is obtained by the Time-To-Distance (T2D) relation, which is determined from samples of $e^+e^- \rightarrow \mu^+\mu^-$

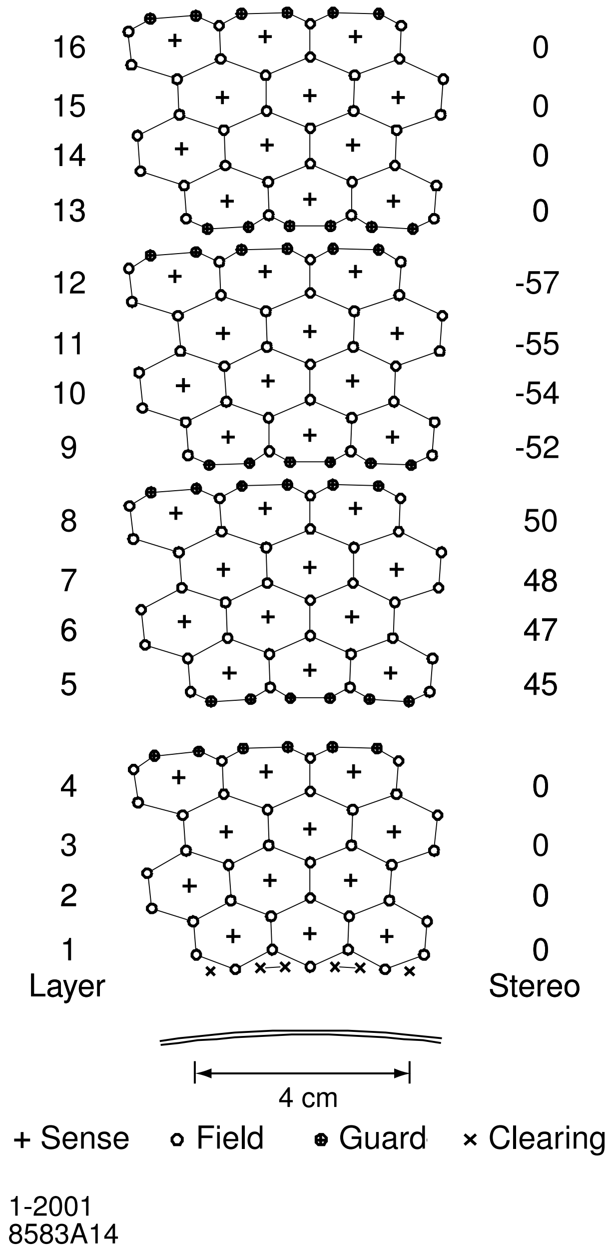

Figure 2.7: Schematic layout of drift cells for the four innermost superlayers. Lines are added between field wires to aid in visualization of the cell boundaries. The diameters of the sense wire and the field wires are 20 μm and 120 μm respectively. The numbers on the right side give the stereo angles (mrad) of sense wires in each layer. The 1 mm-thick beryllium inner wall is shown inside of the first layer.

events. On the other hand, the ionization energy loss dE/dx for charged particles is derived from measurement of total charge deposited in each drift cell.

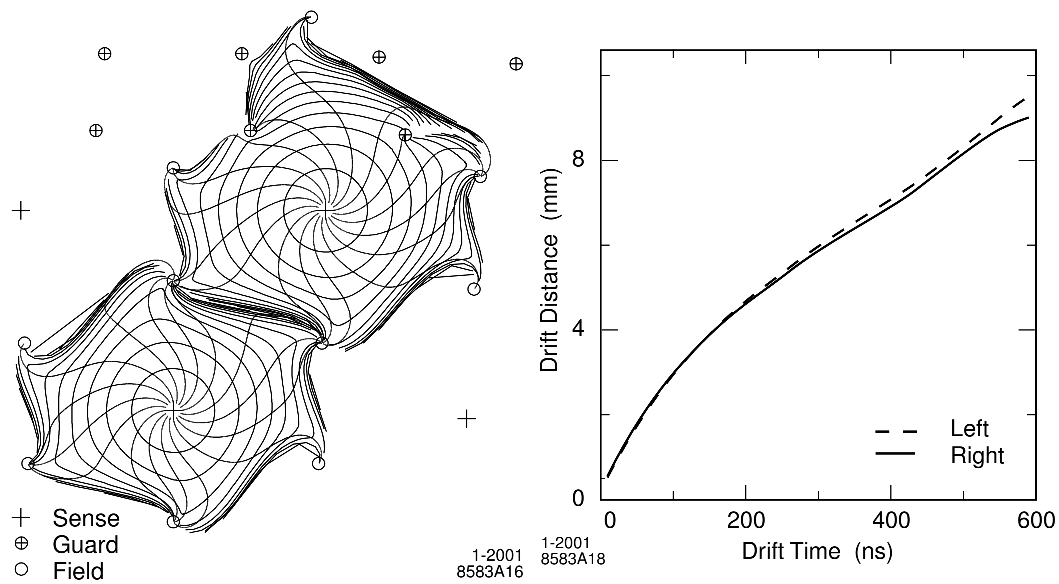

Figure 2.8: Left: Drift cell isochrones, the contours of equal drift times of ions in cells of layers 3 and 4 of an axial superlayer. The isochrones are spaced by 100 ns. Right: The drift time versus distance relation for left and right half of a cell, obtained from the data averaged over all cells in a single layer.

2.2.3 The DIRC

The detector of internally reflected Cherenkov Radiation (DIRC) [57] is a new kind of ring imaging Cherenkov detector, designed to provide the particle identification for *BABAR*. A π/K separation of 4σ or greater is achieved for all tracks 4.2 GeV/c from B-meson decays using a fixed π Cherenkov threshold.

Fig. 2.9 shows a schematic view of the DIRC geometry illustrating the principles of production, transport, and imaging of the light. The radiator consists of 144 long, straight bars of synthetic quartz (refraction index n = 1.473) with rectangular cross section arranged in a 12-sided polygonal barrel. As charged particles pass through with a velocity $v > c/n$, Cherenkov radiation is emitted at a constant Cherenkov angle θ_c with respect to the particle trajectory, given by $\cos\theta_c = 1/n\beta$ ($\beta = v/c$). The radiated photons propagate at group velocity of $-c/(n - \lambda dn/d\lambda)$. As $\beta n > \sqrt{2}$, some photons will always be captured and transported to one or both ends of the bar through total internal reflection. The photon radiation rate $\sim \sin^2\theta_c$ makes roughly a few photons close to threshold.

A mirror is placed on the forward end of the bar to reflect the photons backward where photon detectors are instrumented. Once photons arrive at the instrumented end, most of them emerge into a water-filled expansion region (standoff box). A fused silica wedge at the exit of the bar reflects photons at large angles relative to the bar axis to reduce the size of the required detection surface. It recovers those photons that would otherwise be lost due to internal reflection at the fused silica/water interface. The photons are detected by an array of densely packed photomultiplier tubes (PMTs), each surrounded by reflecting light catcher cones to capture the light that would otherwise miss the active area of the PMT. The expected Cherenkov light pattern at this surface is essentially a conic section, where the cone opening angle is the Cherenkov production angle modified by refraction at the exit from the fused silica window. The Cherenkov angles θ_c can be derived from the position and the arrival time of the PMT signals.

The DIRC reconstruction calculates for each charged track, together with an estimation of the Cherenkov angle and its error, a confidence level for each of the five mass hypotheses e, μ, π, K and p. The probability for a kaon in the DIRC acceptance to be given the largest confidence level for the kaon hypothesis is of order 95% or larger for all dip angles and all momenta above the kaon threshold, while the fraction of pions misidentified as kaons is lower than 3% up to momenta of 3 GeV/c.

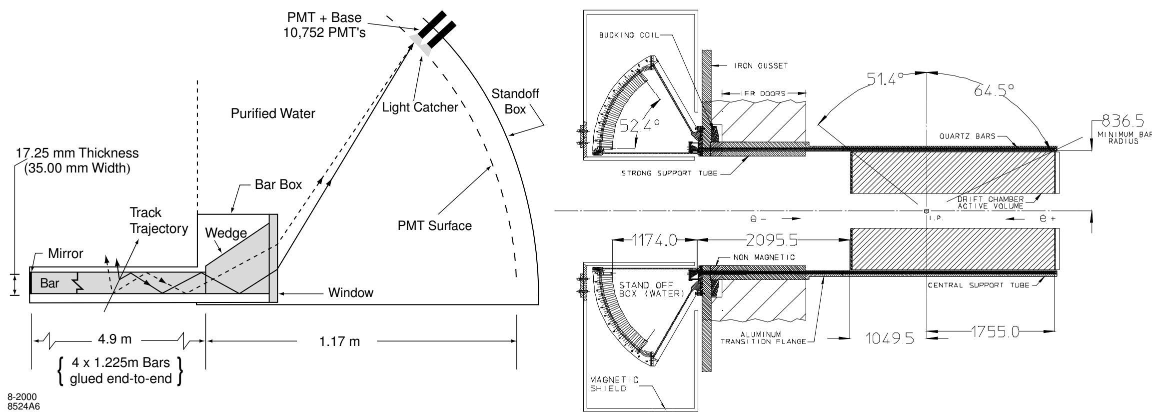

Figure 2.9: Left: Schematics of the DIRC fused silica radiator bar and imaging region. Not shown is a 6mrad angle on the bottom surface of the wedge (see text for detail). Right: Elevation view of the nominal DIRC system geometry. All dimensions are given in mm.

2.2.4 The Electromagnetic Calorimeter

The electromagnetic calorimeter (EMC) is designed to identify the electrons and photons by measuring their corresponding electromagnetic showers. It is designed to provide the measurements with excellent efficiency for both the energy and the angular resolution over the energy range (20 MeV - 9 GeV). The upper bound of 9 GeV is set to measure QED processes, like $e^+e^- \to \gamma\gamma$, for calibration and luminosity determination. The lower bound is set to reconstruct the the low energy π^0s and η^0s from B-decays, such as $B \to \varphi K^+\pi^0(\gamma\gamma)$ in this analysis. Below energies of 2 GeV, the π^0 mass resolution is dominated by the energy resolution while the angular resolution becomes dominant at higher energies.

The energy resolution (measured in GeV) in a calorimeter can be empirically described by a sum of an energy dependent and a constant term $\frac{\sigma E}{E} = \frac{a}{E^{1/4}} \oplus b$. Under ideal conditions values of a and b can be close to 1-2%. The angular resolution is determined by the transverse crystal size and the distance from the interaction point. It is empirically parameterized as $\sigma_\theta = \sigma_\phi = c/\sqrt{E} \oplus d$. A position resolution of a few mm will translate into an angular resolution of a few mrad, corresponding to $c \approx 3$ mrd and $d \approx 1$ mrad. This capacity allows the detection of the photons from the π^0 and η decays, as well as from the electromagnetic and radiative processes.

The physics requirements stated above led to the EMC design based on 6,580 tapered trapezoidal thallium-doped cesium iodide(CsI(Il)) crystals, which have high light yield (50,000 γ/MeV) and short radiation length (1.85 cm). The crystals are arrayed in a cylindrical barrel and a conical forward endcap, as shown in Fig. 2.10. This structure enables a full coverage in azimuth and extends in polar angle from 15.8 to 141.8 degrees, corresponding to a solid-angle coverage of 90% in the center-of-mass system. The energy of the entering particles can be absorbed totally by the crystals and channeled to an electronic readout package at the rear of the crystal. The electronic package consists of two silicon PIN diodes, each of which is directly connected to a low-noise preamplifier.

For low energy photons the energy resolution is calibrated by a 6.13 MeV radioactive source. For high energy photons, *BABAR* uses Bhabha events ($e^+e^- \rightarrow e^+e^-(\gamma)$) for calibration. The EMC energy deposit can be matched up with the charged track information from DCH for the electron identification.

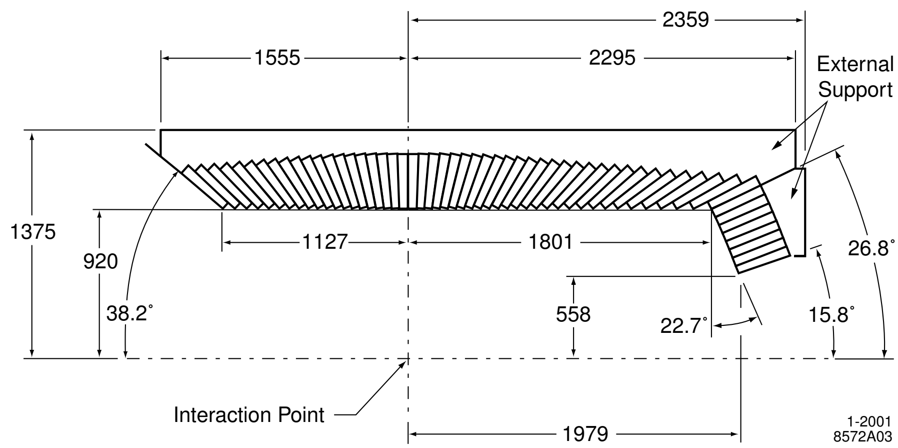

Figure 2.10: A longitudinal cross section of the EMC (only the top half is shown) indicating the arrangement of the 56 crystal rings. The detector is axially symmetric around the z-axis. All dimensions are given in mm.

2.2.5 The Instrumented Flux Return

The Instrumented Flux Return (IFR) is designed to identify muons and neutral hadrons (primarily K_L^0 and neutrons) over a wide range of momenta and angles. The muon identification is crucial for the study of various decays, such as the b flavor tagging for the semi-leptonic neutral B decays, and other rare B, D, and τ decays involving leptons. The K_L^0 identification also plays an important role in the study of some exclusive B decays, especially for the CP eigenstates like $B^0 \to J/\psi K_L^0$, where $J/\psi \to \mu^+\mu^-$.

The IFR uses the steel flux return of the magnet as a muon filter and hadron absorber. It is instrumented with single gap resistive plate chambers (PRC) with two-coordinate readout in the gaps of the finely segmented steel of the barrel and the end doors of the flux return, as shown in Fig. 2.11. RPCs detect streamers from ionizing particles via capacitive readout strips. The position resolution depends on the segmentation of the readout. The RPCs started to degrade and failed to deliver the required efficiency after a few years' running. In the summer of 2004 and 2006, the RPCs in the barrel region were replaced with Limited Streamer Tube (LST) detectors.

The LSTs consist of graphite coated PVC channels of cross-sectional area 2.5$\mathtt{cm}^2$ with a wire running the length of the channel. When a voltage of 5 kV is applied and the tube is held at ground, the chamber is at the edge of breakdown. A passing muon will ionize and start an avalanche of electrons moving towards the anode wire. This produces a signal on the wire that can be read on top of the high voltage. Strip detectors are also positioned perpendicular to the tubes to allow for 2-D position readout.

For the muon identification, charged tracks reconstructed in the tracking system SVT and DCH are extrapolated to the IFR to project their intersections with the RPC planes. For each readout plane, all clusters detected within a predefined distance from the predicted intersection are associated with the track. A number of variables are defined for each IFR cluster associated with a charged track. Complicated selection criteria based on these variables is implemented to provide the muon separation from other particles.

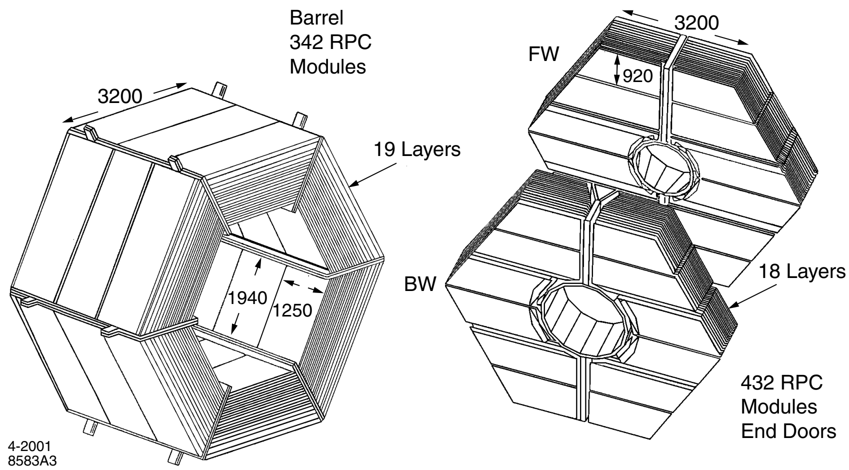

Figure 2.11: Overview of the IFR: Barrel sectors and forward (FW) and backward (BW) end doors; The shape and dimension (in mm) of the RPC modules are indicated.

K_L^0's and other remaining neutral hadrons interact in the steel of the IFR and can be identified as clusters that are not associated with a charged track. Information on neutral showers in the EMC is also used to match with the neutral hadrons detected in the IFR.

2.3 BABAR Trigger and Data Acqusition

The BABAR trigger is designed to select events of interest ($e^+e^- \rightarrow \Upsilon(4S)$), l^+l^-, $q\bar{q}$ etc.) with a high, stable and well-understood efficiency and to reject background events, especially the beam-induced background (~20 kHz), to keep the total event rate under 120 Hz. *BABAR* uses a two level trigger system, the Level 1 (L1) in hardware followed by the Level 3 (L3) in software.

The L1 trigger decision is based on the p_T threshold for charged tracks in the DCH, showers in the EMC, and tracks detected in the IFR. The DCH trigger (DCT) and the EMC trigger (EMT) both satisfy all trigger requirements independently with high efficiency, thus providing a high degree of redundancy. The IFR trigger (IFT) is used to trigger on $\mu^+\mu^-$ and cosmic rays, mostly for diagnostic purposes. During normal operation, the L1 has a typical rate of 1 kHz and yields $> 99.9\%$ efficiency for the $B\overline{B}^0$ events selection.

The L3 receives the output from L1, refines and augments the selection used in L1 to achieve better rejection of background and Bhabha events. The output from the L3 trigger is a set of classification decisions for luminosity determination, diagnostic and calibration purposes. At design luminosity the L3 filter acceptance for physics is ~90 Hz, while ~30 Hz contain the other special event categories. The L3 algorithms comply with the same software conventions and standards used in all other *BABAR* software, thereby simplifying its design, testing and maintenance.

2.4 Particle Reconstruction

Excellent particle identification (PID) over a large range of solid angle and momentum is essential to fulfill the physics goals, such as to enable the quark and lepton flavor tagging in the CP violation measurements. It is achieved with all subsystems contributing, the SVT and DCH measure the momenta and dE/dx for charged tracks, the DIRC measures the velocity $\beta = v/c$ by cherenkov radiation, and the EMC and IFR provide additional signatures for the charged electrons, muons and the neutral hadrons.

2.4.1 Charged Particle Identification

The *BABAR* reconstructs 5 stable charged particles e, μ, π, K, p. A charged particle trajectory is a directional 1-D object in 3-D space. Position measurement in a single active element of a tracking detector is referred to as a hit. A collection of hits presumably from one particle forms a track, being reconstructed to estimate the momentum and trajectory.

The offline charged track reconstruction uses the standard pattern recognition algorithms in both the SVT and DCH. It starts with a proto-track seed in the DCH far from the beamline and searches for nearby hits which approximately lie on a line to form a consistent straight track. Tracks found in the DCH (SVT) are extrapolated into the SVT (DCH) respectively, and hits consistent with the original fit are added. The SVT hits which cannot be added to the DCH tracks are passed to two complementary standalone tracking finding algorithms to reconstruct the low p_T tracks. In the end, an attempt is made to combine tracks that are only found by one tracking system and thus recover tracks scattered in the material of the support tube. The track finding and fitting procedures make use of Kalman filter algorithm [58] that takes into account the detailed distribution of material in the detector and the full map of the magnetic field.

For the charged tracks with $p_T > 150$ MeV/c the momentum measurements obtained from the SVT and DCH are associated with the DIRC Cherenkov angle θ_C measurement to determine their mass and identification. The left plot of Fig. 2.12 shows the relation between the fitted θ_C and the lab frame momentum from an inclusive sample of multihadron events. The π/K separation is achieved over a wide momentum range (1.7 - 4) GeV/c.

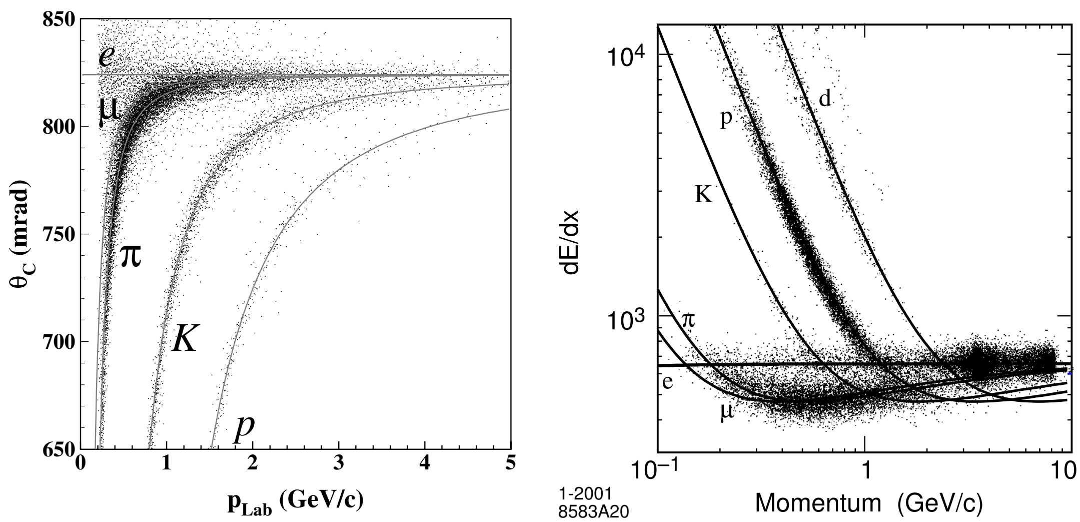

Figure 2.12: Left: The fitted Cherenkov angle of tracks from an inclusive sample of multihadron events plotted against the momentum of the tracks at the entrance to the DIRC bar box. The grey lines are the predicted values of the θ_C for the different particle species. Right: dE/dx measurement in the DCH as a function of track momenta. The data includes large samples of beam background triggers, as evident from the high rate of protons. The curves show the Bethe-Bloch predictions derived from selected control samples of particles of different masses.

The particle identification (especially the π/K separation) below 700 MeV/c relies mainly on the dE/dx measurements in the DCH and SVT, as the kaons fail to produce

Cherenkov light due to insufficient velocity. The ionization energy loss dE/dx is given by Bethe-Bloch equation [56]

$$-\frac{dE}{dx} = \frac{4\pi n z^2 e^4}{m_e v^2}[\mathtt{ln}\frac{2m_e v^2}{I(1-(v/c)^2)} - (\frac{v}{c})^2] \tag{2.1}$$

where n is the number of electrons per cm^3 in the stopping substance, m_e is the electron mass, ze and v are the charge and velocity of the incoming particle and I is the mean excitation potential of the atoms of the stopping substance. The right plot of Fig. 2.12 shows the momentum dependence of dE/dx for particles transversing the DCH.

Electrons lose energy mainly in the EMC (see Sec. 2.2.4) by creating electromagnetic showers. The measured electromagnetic shower is used to derive the electron energy, which can be matched up with the charge track information from the DCH to provide the electron PID. Muons lose little energy in the EMC and are identified in the IFR (see Sec. 2.2.5).

2.4.2 Neutral Particle Reconstruction

Neutral particles except photons are generally reconstructed through their decay products, most of which can be directly detected as charged stable particles or photons. This section describes the reconstruction of π^0 and K^0_S that are relevant to this analysis.

The K^0_S candidates with a proper decay length about 3 cm are reconstructed through $K^0_S \to \pi^+\pi^-$, with the invariant mass measurement $|m_{\pi^+\pi^-} - m_{K^0}| < 12$ MeV. A vertex-constrained fit is performed to require that the two tracks originate from a common vertex and require that the lifetime significance of the K^0_S be $\tau/\sigma_\tau > 5$, where τ and σ_τ are the K^0_S

lifetime and its uncertainty determined from the vertex-constrained fit. Besides, the cosine of the angle between the flight direction from the interaction point and the momentum direction is required to be > 0.995. The K_S^0 selection efficiency requirement is $\approx 90\%$.

The neutral π^0 is reconstructed through $\pi^0 \to \gamma\gamma$ with the photons being detected in the EMC (see Sec. 2.2.4). Fig. 2.13 shows $\gamma\gamma$ invariant mass in $B\overline{B}$ events. The π^0 candidates are selected using various kinematic cuts, such as invariant mass $0.120 < m_{\gamma\gamma} < 0.150$ GeV, lateral moment $\mathrm{LAT}_\gamma < 0.8$, and photon energy $E_\gamma > 30$ MeV. The mass of a π^0 candidate meeting this criterion is then constrained to the nominal value [56] and, when combined with other tracks or neutrals to form a B candidate, to originate from the B candidate vertex. This improves the mass and energy resolution of the parent particle K_J^*.

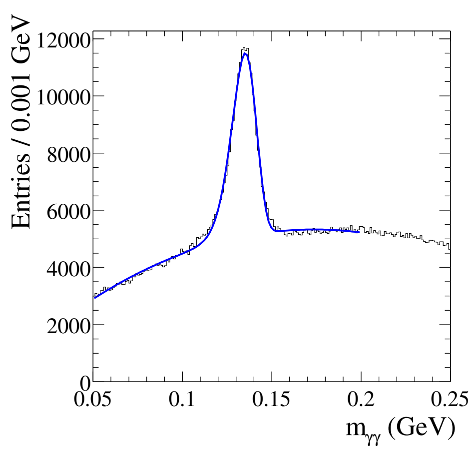

Figure 2.13: Two-photon invariant mass in $B\overline{B}$ events. The energies of the photons and π^0 are required to exceed 30 MeV and 300 MeV, respectively. The solid line is a fit to data.

Chapter 3

Analysis Strategy

This chapter summaries the analysis techniques that are used in the analysis on rare charmless decays $B \to \varphi K_J^{(*)}$. The $K_J^{(*)}$ can be reconstructed by $K\pi$ and $K\pi\pi$ decays. Four K_J^* resonances are considered in the $K\pi$ final state: scalar $(K\pi)_0^*$, vector $K^*(1680)$ and tensors $K_2^*(1430)$, $K_3^*(1780)$ and $K_4^*(2045)$. Five $K_J^{(*)}$ resonances are considered in the $K\pi\pi$ final state: axial-vector $K_1(1270)$ and $K_1(1400)$, vector $K^*(1410)$ and tensors $K_2^*(1430)$, $K_2(1770)$ and $K_2(1820)$ (see. Table 1.4).

The phenomenological signatures to search for these decays are layed out first. The helicity structure for each $B \to \varphi K_J^{(*)}$ decay channel can be extracted from the angular distributions based on three angles, see Fig. 3.1. The combination of the angular and $K\pi(\pi)$ invariant mass distributions makes it possible to experimentally distinguish the various $K_J^{(*)}$ resonances. The effect of interference between different K_J^* resonances on the angular and amplitude measurements is discussed.

Experimental techniques on selecting the signal decays $B \rightarrow \varphi K_J^{(*)}$ from the *BABAR* reconstructed event-store database are described after that. The signal events are selected based on the track information such as charge and four-momentum. Particle identification requirements are also imposed on the final states $\varphi \rightarrow K^+K^-$ and $K_J^{(*)} \rightarrow K^+\pi^-, K_S^0\pi^+$ and $K^+\pi^+\pi^-$. The dominant background decays $e^+e^- \rightarrow q\bar{q}$ are rejected or reduced by kinematic observables $m_{\rm ES}$ and ΔE and the event shape parameter $\mathcal{F}$. Since these decays are rare decays with branching fractions on the order of a few per million B-decays, preliminary cuts on kinematic observables $m_{K\overline{K}}$ and $m_{K\pi(\pi)}$ are also used to optimize the signal to background ratio. The three angles $\cos\theta_1$, $\cos\theta_2$ and Φ are also extracted from the four-momentum of the final state tracks.

In the end, an unbinned extended maximum-likelihood fit based on $N_{\tt cand}$ candidates data sample is developed to simultaneously measure the signal yield, CP asymmetries and angular parameters such as f_L. For each event in the datasample, there are nine (eight) primary observables $m_{\rm ES}$, ΔE, $\mathcal{F}$, $m_{K\pi\pi}$, m_{KK}, $\mathcal{H}_1$, $\mathcal{H}_2$, (Φ), $Q\}$. Analyses at *BABAR* are done using a blind technique. Numerical values of all physics parameters are kept hidden until the analysis method is determined, validated and fixed.

3.1 Angular Distributions

The helicity amplitudes $A_{J\lambda}$ are extracted from the angular distributions of decays $B \to \varphi K_J^{(*)}$ based on three angles (θ_1, θ_2, Φ), as shown in Fig. 3.1. For the decays $B \to \varphi K_J^*(K\pi)$, the θ_1 is the angle between the direction of the K meson from the $K_J^* \to K\pi$ and the direction opposite the B in the $K_J^{(*)}$ rest frame. The azimuthal angle Φ is defined as the angle between the decay planes of the two mesons φ and K_J^*. For the decays $B \to \varphi K_J^{(*)}(K\pi\pi)$, the θ_1 is the angle between the normal to the three-body decay plane (pointed out in Ref. [64]) of $K_J^{(*)} \to K\pi\pi$ and the direction opposite the B in the $K_J^{(*)}$ rest frame. The azimuthal angle Φ is defined as the angle between the decay plane of φ meson and the plane of the B meson decay axis and the normal to the three-body decay plane $K_J^{(*)} \to K\pi\pi$. In both final states, the θ_2 is the angle between the direction of K^+ and $\varphi \to K^+K^-$ and the direction opposite the B in the φ rest frame. The helicities are defined as $\mathcal{H}_i = \cos\theta_i$ ($i = 1, 2$).

3.1.1 Angular Formalism of Decays $B \to \varphi K_J^*(K\pi)$

Consider a general two-body B-decay to spin J_1 X_1 and spin J_2 X_2, where both X_i ($i = 1, 2$) decay to two pseudoscalars through parity conserving strong interactions. The parity of both X_i ($i = 1, 2$) is $P_i = (-1)^{J_i}$. Following the two-body decay formalism [64],

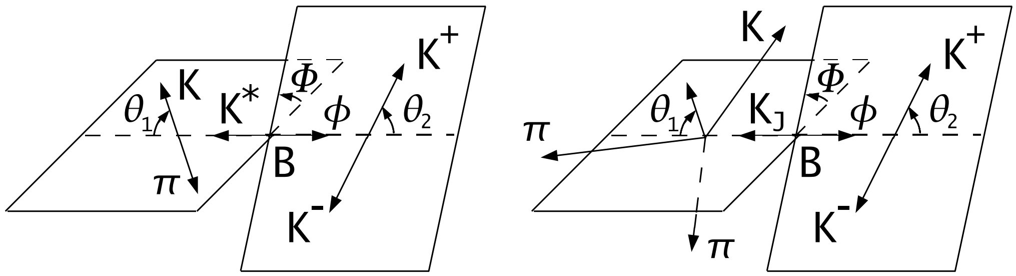

Figure 3.1: Definition of decay angles given in the rest frames of the decaying parents. Left plot: two-body decay of $K^* \to K\pi$; right plot: three-body decay of $K_J \to K\pi\pi$. In the two-body decay, the two decay planes are defined as the actual decay planes. In the three-body decay of K_J, the plane is replaced the plane consisting of K_1's flight line in B's restframe and the decay norm of the K_J's decay plane.

differential decay width of this decay is written as:

$$\frac{1}{\Gamma}\frac{d^3\Gamma}{d\cos\theta_1 d\cos\theta_2 d\Phi} = \frac{1}{\sum|A_\lambda|^2}\left|\sum_\lambda A_\lambda Y_{J_1}^{\lambda}(\theta_1, 0)\, Y_{J_2}^{-\lambda}(\pi-\theta_2, -\Phi)\right|^2. \qquad (3.1)$$

The suming index λ is the helicity value of both X_i and takes the value between $(-j, +j)$, with j being the smaller of J_1 and J_2. The Y_J^λ are the spherical harmonic functions.

For the $B \to \varphi K_J^*$ decays, $J_1 = J$ (K_J^*) and $J_2 = 1$ (φ). The angular distribution for a vector-scalar decay $B \to \varphi(K\pi)_0^*$ is proportional to $\mathcal{H}_1^2\mathcal{H}_2^2$. For $J \neq 0$, the decay amplitude can be expressed with the help of six real terms α_{iJ}:

$$\alpha_{1J} = \tfrac{|A_0|^2}{\Sigma|A_\lambda|^2} = f_{LJ}, \qquad (3.2)$$

$$\alpha_{2J} = \frac{|A_\parallel|^2 + |A_\perp|^2}{\Sigma|A_\lambda|^2} = \frac{|A_{+1}|^2 + |A_{-1}|^2}{\Sigma|A_\lambda|^2} = (1 - f_L),$$

$$\alpha_{3J} = \frac{|A_\parallel|^2 - |A_\perp|^2}{\Sigma|A_\lambda|^2} = 2\cdot\frac{\Re e(A_{+1}A_{-1}^*)}{\Sigma|A_\lambda|^2} = (1 - f_L - 2\cdot f_\perp),$$

$$\alpha_{4J} = \frac{\Im m(A_\perp A_\parallel^*)}{\Sigma|A_\lambda|^2} = \frac{\Im m(A_{+1}A_{-1}^*)}{\Sigma|A_\lambda|^2} = \sqrt{f_\perp\cdot(1 - f_L - f_\perp)}\cdot\sin(\phi_\perp - \phi_\parallel),$$

$$\alpha_{5J} = \frac{\Re e(A_{\parallel} A_0^*)}{\Sigma |A_\lambda|^2} = \frac{\Re e(A_{+1} A_0^* + A_{-1} A_0^*)}{\sqrt{2} \cdot \Sigma |A_\lambda|^2} = \sqrt{f_L \cdot (1 - f_L - f_\perp)} \cdot \cos(\phi_\parallel),$$

$$\alpha_{6J} = \frac{\Im m(A_\perp A_0^*)}{\Sigma |A_\lambda|^2} = \frac{\Im m(A_{+1} A_0^* - A_{-1} A_0^*)}{\sqrt{2} \cdot \Sigma |A_\lambda|^2} = \sqrt{f_\perp \cdot f_L} \cdot \sin(\phi_\perp).$$

From Eq. (3.1) the angular distribution of the vector-vector decay $B \to \varphi K^*(892)$ $(J = 1)$ is

$$\frac{8\pi}{9\Gamma} \frac{d^3\Gamma}{d\mathcal{H}_1 d\mathcal{H}_2 d\Phi} = \mathcal{P}^{\text{4body}}_{J^P=1^-}(\mathcal{H}_1, \mathcal{H}_2, \Phi) = \alpha_{1J} \times \mathcal{H}_1^2 \mathcal{H}_2^2 \tag{3.3}$$

$$+\alpha_{2J} \times (1 - \mathcal{H}_1^2)(1 - \mathcal{H}_2^2)$$

$$+\alpha_{3J} \times (1 - \mathcal{H}_1^2)(1 - \mathcal{H}_2^2) \cos 2\Phi$$

$$+\alpha_{4J} \times (1 - \mathcal{H}_1^2)(1 - \mathcal{H}_2^2) \sin 2\Phi$$

$$+\alpha_{5J} \times \sqrt{1 - \mathcal{H}_1^2}\, \mathcal{H}_1 \sqrt{1 - \mathcal{H}_2^2}\, \mathcal{H}_2 \cos \Phi$$

$$+\alpha_{6J} \times \sqrt{1 - \mathcal{H}_1^2}\, \mathcal{H}_1 \sqrt{1 - \mathcal{H}_2^2}\, \mathcal{H}_2 \sin \Phi.$$

The angular distribution of the vector-tensor B decays $B \to \varphi K_2^*(1430)$ $(J = 3)$ is

$$\frac{32\pi}{15\Gamma} \frac{d^3\Gamma}{d\mathcal{H}_1 d\mathcal{H}_2 d\Phi} == \mathcal{P}^{\text{4body}}_{J^P=2^+}(\mathcal{H}_1, \mathcal{H}_2, \Phi) = \alpha_{1J} \times (3\mathcal{H}_1^2 - 1)^2 \mathcal{H}_2^2 \tag{3.4}$$

$$+\alpha_{2J} \times 12\, \mathcal{H}_1^2 (1 - \mathcal{H}_1^2)(1 - \mathcal{H}_2^2)$$

$$+\alpha_{3J} \times 12\, \mathcal{H}_1^2 (1 - \mathcal{H}_1^2)(1 - \mathcal{H}_2^2) \cos 2\Phi$$

$$+\alpha_{4J} \times 12\, \mathcal{H}_1^2 (1 - \mathcal{H}_1^2)(1 - \mathcal{H}_2^2) \sin 2\Phi$$

$$+\alpha_{5J} \times (2\sqrt{3})(3\mathcal{H}_1^2 - 1)\sqrt{1 - \mathcal{H}_1^2}\, \mathcal{H}_1 \sqrt{1 - \mathcal{H}_2^2}\, \mathcal{H}_2 \cos \Phi$$

$$+\alpha_{6J} \times (2\sqrt{3})\,(3\mathcal{H}_1^2 - 1)\sqrt{1-\mathcal{H}_1^2}\,\mathcal{H}_1\,\sqrt{1-\mathcal{H}_2^2}\,\mathcal{H}_2\,\sin\Phi.$$

Due to the relatively low statistics, the angular distributions of decays $B \to \varphi K_3^*(1780)$ ($J = 3$) and $B \to \varphi K_4^*(2045)$ ($J = 4$) are simplified by integrating out the Φ angle. It leads to a partial angular distribution for decay $B \to \varphi K_3^*(1780)$ as

$$\frac{16}{21\Gamma}\,\frac{d^2\Gamma}{d\mathcal{H}_1 d\mathcal{H}_2} = \mathcal{P}^{\text{4body}}_{J^P=3^-}(\mathcal{H}_1,\mathcal{H}_2) = \alpha_{1J} \times (5\mathcal{H}_1^3 - 3\mathcal{H}_1)^2\,\mathcal{H}_2^2 + \alpha_{2J} \times \frac{3}{2}\,(5\mathcal{H}_1^2 - 1)^2(1-\mathcal{H}_1^2)\,(1-\mathcal{H}_2^2). \tag{3.5}$$

The partial angular distributions for decay $B \to \varphi K_4^*(2045)$ is given as:

$$\frac{256}{27\Gamma}\,\frac{d^2\Gamma}{d\mathcal{H}_1 d\mathcal{H}_2} = \mathcal{P}^{\text{4body}}_{J^P=4^+}(\mathcal{H}_1,\mathcal{H}_2) = \alpha_{1J} \times (35\mathcal{H}_1^4 - 30\mathcal{H}_1^2 + 3)^2\,\mathcal{H}_2^2 + \alpha_{2J} \times 40\,\mathcal{H}_1^2(3 - 7\mathcal{H}_1^2)^2(1-\mathcal{H}_1^2)\,(1-\mathcal{H}_2^2). \tag{3.6}$$

3.1.2 Angular Formalism of Decays $B \to \varphi K_J^{(*)}(K\pi\pi)$

Consider a general two-body B-decay to spin J_1 X_1 and spin J_2 X_2. Particle X_1 and X_2 decay to three and two pseudoscalars through parity-conserving strong interactions, respectively. Following the three-body decay formalism [65], the differential decay width of $B \to X_1\,X_2$ can be written as

$$\frac{1}{\Gamma}\frac{d^3\Gamma}{d\cos\theta_1 d\cos\theta_2 d\Phi} \propto \frac{1}{\sum|A_\lambda|^2}\sum_m |R_m|^2\,\left|\,\sum_\lambda A_\lambda d^{J_1}_{\lambda,m}(\theta_1)\,Y^{-\lambda}_{J_2}(\pi-\theta_2,-\Phi)\right|^2, \tag{3.7}$$

where the normalization factor is omitted for simplicity (in general it would include a combination of the $|R_m|^2$ parameters). The index m runs from $-J_2$ to $+J_2$ and λ runs from $-j$ and $+j$ (with j again being the smaller of J_1 and J_2).

Compared to the four body B-decays described in the previous section, one additional phenomenological amplitude R_m is required to describe the three-body decay X_1. It depends on the X_1 spin eigenvalue m but not on λ. The interferences between different R_m amplitudes vanish as the decay width is integrated over the rotation angle around the normal to the decay plane. There are $2J_1 + 1$ real parameters $|R_m|^2$. Additional symmetry considerations could put constraints on $|R_m|^2$ values, as discussed below and in Ref. [65].

It is found that for even (odd)parity of X_1 only odd (even) values of m contribute, that is $P_1 = (-1)^{m+1}$ [65]. This results in only $m = 0$ contributing to the decays with $J_1^{P_1} = 1^-$, such as $B \to \varphi K^*(1410)$. Thus, the Eq. (3.7) reduces to Eq. (3.1) due to the simple relationship of the $d^J_{\lambda,m}$ functions with $m = 0$ and the spherical harmonics Y^λ_J. In a general case of $J_1^{P_1} \neq 1^-$ quantum numbers, more than one $|R_m|^2$ parameters contributes, such as B decays to φ and $K_1(1270)$ (1^+), $K_1(1400)$ (1^+), $K_2^*(1430)$ (2^+), $K_2(1770)^+$ and $K_2(1820)$ (2^-). In these cases similar three complex amplitudes $A_{J\lambda}$ are needed as in the four body final states decays. But three new real terms α_i may appear in the angular distribution in addition to those shown in Eq. (3.2),

$$\begin{aligned}
\alpha_{7J} &= \frac{\Re e(A_\perp A_\parallel^*)}{\Sigma|A_\lambda|^2} = \frac{|A_{+1}|^2 - |A_{-1}|^2}{2\cdot\Sigma|A_\lambda|^2} = \sqrt{f_\perp\cdot(1-f_L-f_\perp)}\cdot\cos(\phi_\perp-\phi_\parallel) \\
\alpha_{8J} &= \frac{\Im m(A_\parallel A_0^*)}{\Sigma|A_\lambda|^2} = \frac{\Im m(A_{+1}A_0^* + A_{-1}A_0^*)}{\sqrt{2}\cdot\Sigma|A_\lambda|^2} = \sqrt{f_L\cdot(1-f_L-f_\perp)}\cdot\sin(\phi_\parallel) \\
\alpha_{9J} &= \frac{\Re e(A_\perp A_0^*)}{\Sigma|A_\lambda|^2} = \frac{\Re e(A_{+1}A_0^* - A_{-1}A_0^*)}{\sqrt{2}\cdot\Sigma|A_\lambda|^2} = \sqrt{f_\perp\cdot f_L}\cdot\cos(\phi_\perp).
\end{aligned} \tag{3.8}$$

To simplify the formalism, one can redefine some of the parameters

$$r_m \equiv \frac{|R_m|^2 - |R_{-m}|^2}{|R_m|^2 + |R_{-m}|^2}\,, \tag{3.9}$$

$$r_{02} \equiv \frac{|R_0|^2}{|R_2|^2 + |R_{-2}|^2}\,. \tag{3.10}$$

From Eq. (3.7) the angular distribution of decay $B \to \varphi K_2^*(1430)(K\pi\pi)$ is written as

$$\begin{aligned}
\frac{64\pi}{45\Gamma}\frac{d^3\Gamma}{d\cos\theta_1 d\cos\theta_2 d\Phi} = \mathcal{P}^{\text{5body}}_{J^P=2^+}(\mathcal{H}_1,\mathcal{H}_2,\Phi) = \alpha_{1J} \times 4\mathcal{H}_1^2(1-\mathcal{H}_1^2)\,\mathcal{H}_2^2 \\
+\alpha_{2J} \times \frac{1}{3}(4\mathcal{H}_1^4 - 3\mathcal{H}_1^2 + 1)\,(1-\mathcal{H}_2^2) \\
-\alpha_{3J} \times \frac{1}{3}(-4\mathcal{H}_1^4 + 5\mathcal{H}_1^2 - 1)\,(1-\mathcal{H}_2^2)\,\cos 2\Phi \\
+\alpha_{4J} \times \frac{2}{3}(-4\mathcal{H}_1^4 + 5\mathcal{H}_1^2 - 1)\,(1-\mathcal{H}_2^2)\,\sin 2\Phi \\
-\alpha_{5J} \times \frac{8}{\sqrt{6}}\mathcal{H}_1\sqrt{1-\mathcal{H}_1^2}(2\mathcal{H}_1^2-1)\,\mathcal{H}_2\sqrt{1-\mathcal{H}_2^2}\,\cos\Phi \\
+\alpha_{6J} \times \frac{8}{\sqrt{6}}\mathcal{H}_1\sqrt{1-\mathcal{H}_1^2}(2\mathcal{H}_1^2-1)\,\mathcal{H}_2\sqrt{1-\mathcal{H}_2^2}\,\sin\Phi \\
+\alpha_{7J} \times r_1\frac{4}{3}\mathcal{H}_1(2\mathcal{H}_1^2-1)\,(1-\mathcal{H}_2^2) \\
+\alpha_{8J} \times r_1\frac{8}{\sqrt{6}}\mathcal{H}_1^2\sqrt{1-\mathcal{H}_1^2}\,\mathcal{H}_2\sqrt{1-\mathcal{H}_2^2}\,\sin\Phi \\
-\alpha_{9J} \times r_1\frac{8}{\sqrt{6}}\mathcal{H}_1^2\sqrt{1-\mathcal{H}_1^2}\,\mathcal{H}_2\sqrt{1-\mathcal{H}_2^2}\,\cos\Phi.
\end{aligned} \tag{3.11}$$

For the vector–axial-vector decays $B \to \varphi K_1(K\pi\pi)$, the angular distribution is

$$\begin{aligned}
\frac{16\pi}{9\Gamma}\frac{d^3\Gamma}{d\cos\theta_1 d\cos\theta_2 d\Phi} = \mathcal{P}^{\text{5body}}_{J^P=1^+}(\mathcal{H}_1,\mathcal{H}_2,\Phi) = \alpha_{1J} \times (1-\mathcal{H}_1^2)\,\mathcal{H}_2^2 \\
+\alpha_{2J} \times \frac{1}{4}(1+\mathcal{H}_1^2)\,(1-\mathcal{H}_2^2)
\end{aligned} \tag{3.12}$$

$$-\alpha_{3J} \times \frac{1}{4}(1-\mathcal{H}_1^2)\,(1-\mathcal{H}_2^2)\,\cos 2\Phi$$

$$+\alpha_{4J} \times \frac{1}{2}(1-\mathcal{H}_1^2)\,(1-\mathcal{H}_2^2)\,\sin 2\Phi$$

$$-\alpha_{5J} \times \sqrt{2}\mathcal{H}_1\sqrt{1-\mathcal{H}_1^2}\,\mathcal{H}_2\sqrt{1-\mathcal{H}_2^2}\,\cos\Phi$$

$$+\alpha_{6J} \times \sqrt{2}\mathcal{H}_1\sqrt{1-\mathcal{H}_1^2}\,\mathcal{H}_2\sqrt{1-\mathcal{H}_2^2}\,\sin\Phi$$

$$+\alpha_{7J} \times r_1\mathcal{H}_1\,(1-\mathcal{H}_2^2)$$

$$+\alpha_{8J} \times r_1\sqrt{2}\mathcal{H}_1\sqrt{1-\mathcal{H}_1^2}\,\mathcal{H}_2\sqrt{1-\mathcal{H}_2^2}\,\sin\Phi$$

$$-\alpha_{9J} \times r_1\sqrt{2}\mathcal{H}_1\sqrt{1-\mathcal{H}_1^2}\,\mathcal{H}_2\sqrt{1-\mathcal{H}_2^2}\,\cos\Phi.$$

For the vector-tensor decays $B \to \varphi K_2(K\pi\pi)$, the angular distribution is

$$\frac{64\pi(1+r_{02})}{45\Gamma}\frac{d^3\Gamma}{d\cos\theta_1 d\cos\theta_2 d\Phi} = \mathcal{P}^{\text{5body}}_{J^P=2^-}(\mathcal{H}_1,\mathcal{H}_2,\Phi) \tag{3.13}$$

$$= \alpha_{1J} \times [(1-\mathcal{H}_1^2)^2 \;+\; r_{02}\,\frac{2}{3}(3\mathcal{H}_1^2-1)^2]\,\mathcal{H}_2^2$$

$$+\alpha_{2J} \times [\frac{1}{3}(1-\mathcal{H}_1^4) \;+\; r_{02}\,2\mathcal{H}_1^2(1-\mathcal{H}_1^2)]\,(1-\mathcal{H}_2^2)$$

$$-\alpha_{3J} \times [\frac{1}{3}(1-\mathcal{H}_1^2)^2 \;-\; r_{02}\,2\mathcal{H}_1^2(1-\mathcal{H}_1^2)]\,(1-\mathcal{H}_2^2)\,\cos\,2\Phi$$

$$+\alpha_{3J} \times [\frac{2}{3}(1-\mathcal{H}_1^2)^2 \;-\; r_{02}\,4\mathcal{H}_1^2(1-\mathcal{H}_1^2)]\,(1-\mathcal{H}_2^2)\,\sin\,2\Phi$$

$$-\alpha_{5J} \times [\frac{4}{\sqrt{6}}\mathcal{H}_1(1-\mathcal{H}_1^2)^{\frac{3}{2}} \;-\; r_{02}\,\frac{8}{\sqrt{6}}\mathcal{H}_1\sqrt{1-\mathcal{H}_1^2}(3\mathcal{H}_1^2-1)]\,\mathcal{H}_2\sqrt{1-\mathcal{H}_2^2}\cos\,\Phi$$

$$+\alpha_{6J} \times [\frac{4}{\sqrt{6}}\mathcal{H}_1(1-\mathcal{H}_1^2)^{\frac{3}{2}} \;-\; r_{02}\,\frac{8}{\sqrt{6}}\mathcal{H}_1\sqrt{1-\mathcal{H}_1^2}(3\mathcal{H}_1^2-1)]\,\mathcal{H}_2\sqrt{1-\mathcal{H}_2^2}\sin\,\Phi$$

$$+\alpha_{7J} \times r_1\frac{4}{3}\mathcal{H}_1(2\mathcal{H}_1^2-1)\,(1-\mathcal{H}_2^2)$$

$$+\alpha_{8J} \times r_1\frac{8}{\sqrt{6}}\mathcal{H}_1^2\sqrt{1-\mathcal{H}_1^2}\,\mathcal{H}_2\sqrt{1-\mathcal{H}_2^2}\,\sin\Phi$$

$$-\alpha_{9J} \times r_1 \frac{8}{\sqrt{6}} \mathcal{H}_1^2 \sqrt{1-\mathcal{H}_1^2}\, \mathcal{H}_2 \sqrt{1-\mathcal{H}_2^2}\, \cos\Phi.$$

The r_m terms in Eqs. (3.11–3.13) would vanish if there was a symmetry with respect to the inversion of the normal to the $K_J^{(*)}$ decay plane, that is between the m and $-m$ terms. As was pointed out in Ref. [65], examples of such cases are two identical pseudoscalar particles or pions in an isotropic spin eigenstate, such as a sequential decay like $K_1 \to \rho K \to \pi\pi K$. However, in the more general case $-J < r_m < J$, R_m depends on the three-body decay dynamics. The r_{02} term in Eq. (3.13) is also a priori unknown, the understanding of which also depends on the dynamics of a specific three-body decay $K_J^{(*)} \to K\pi\pi$.

3.2 Invariant Mass Distributions

The differential decay widths given in Eq. (3.1) and (3.7) are parameterized as functions of helicity angles. However, they also depend on the invariant mass $m_{K\pi(\pi)}$ of the $K\pi(\pi)$ resonance. Without considering interference between different modes, this mass dependence decouples from the angular dependence. Nonetheless, this dependence is important to separate different $K\pi(\pi)$ states. The interference effects are discussed in Sec. 3.3.

3.2.1 $K\pi$ Invariant Mass Distributions

A relativistic spin-J Breit-Wigner (B-W) complex amplitude R_J can be used to parameterize a spin-J resonance mass [56] of nominal mass m_0 and width Γ

$$R_J(m) = \frac{m_J \Gamma_J(m)}{(m_J^2 - m^2) - i m_J \Gamma_J(m)} = \sin\delta_J e^{i\delta_J}, \tag{3.14}$$

where

$$\cot\delta_J = \frac{m_J^2 - m^2}{m_J \Gamma_J(m)}. \tag{3.15}$$

For the $K_J^* \to K\pi$ with $J = 0, 1, 2, 3, 4$, the $K\pi$ mass distributions are given by

$$\Gamma_0(m) = \Gamma \frac{m_0}{m} \left[\frac{q}{q_0}\right], \tag{3.16}$$

$$\Gamma_1(m) = \Gamma \frac{m_0}{m} \frac{1 + r^2 q_0^2}{1 + r^2 q^2} \left[\frac{q}{q_0}\right]^3, \tag{3.17}$$

$$\Gamma_2(m) = \Gamma \frac{m_0}{m} \frac{9 + 3r^2 q_0^2 + r^4 q_0^4}{3 + 3r^2 q^2 + r^4 q^4} \left[\frac{q}{q_0}\right]^5 \tag{3.18}$$

$$\Gamma_3(m) = \Gamma_0 \frac{m_0}{m} \frac{-45 + 243 r^2 q_0^2 - 30 r^4 q_0^4 + r^6 q_0^6}{-45 + 243 r^2 q^2 - 30 r^4 q^4 + r^6 q^6} \left[\frac{q}{q_0}\right]^7, \tag{3.19}$$

$$\Gamma_4(m) = \Gamma_0 \frac{m_0}{m} \frac{(r^4 q_0^4 - 45 r^2 q_0^2 + 105)^2 + 25 r^2 q_0^2 (2r^2 q_0^2 - 21)^2}{(r^4 q^4 - 45 r^2 q^2 + 105)^2 + 25 r^2 q^2 (2r^2 q^2 - 21)^2} \left[\frac{q}{q_0}\right]^9. \tag{3.20}$$

The 'q' is the momentum of a daughter particle in the resonance system after its two-body decay (q_0 is evaluated at m_0), and the r is the interaction radius. For the m_{KK} distribution of φ resonance, the same parametrization with $\Gamma_1(m_{KK})$ is used. The invariant amplitude $M_J(m)$ is proportional to $R_J(m)$:

$$M_J(m) \propto \frac{m}{q} R_J(m) \tag{3.21}$$

The parameterization of the scalar $(K\pi)^{*0}_0$ mass distribution requires more attention. Studies of $K\pi$ scattering were performed by the LASS experiment [68, 69]. It was found that the scattering is elastic up to about 1.5 GeV and can be parameterized with the amplitude:

$$R_0(m) = \sin\delta_0 e^{i\delta_0}, \tag{3.22}$$

where

$$\delta_0 = \Delta R + \Delta B. \tag{3.23}$$

ΔR represents a resonant $K_0^*(1430)$ contribution and ΔB represents a non-resonant contribution. The mass dependence of ΔB is described by means of an effective range parameterization of the usual type

$$\cot\Delta B = \frac{1}{aq} + \frac{1}{2}rq, \tag{3.24}$$

where a is the scattering length and r is the effective range. The mass dependence of ΔR is described by means of a Breit-Wigner parameterization of the form

$$\cot\Delta R = \frac{m_0^2 - m^2}{m_0\Gamma_0(m)}, \tag{3.25}$$

where m_0 is the resonance mass, and $\Gamma_0(m)$ is defined as

$$\Gamma_0(m) = \Gamma_0\frac{m_0}{m}\left(\frac{q}{q_0}\right). \tag{3.26}$$

The invariant amplitude $M_0(m)$ can be expressed as,

$$M_0(m) \propto \frac{m}{q\cot\Delta B - iq} + \; e^{2i\Delta B}\frac{\Gamma_0 m_0^2/q_0}{(m_0^2 - m^2) - im_0\Gamma_0(m)}\,. \tag{3.27}$$

The resulting $(K\pi)_0^{*0}$ invariant mass distribution is shown in Fig. 3.2.1, along with the phase and distributions for the other resonances. Measurements of the LASS experiment are used

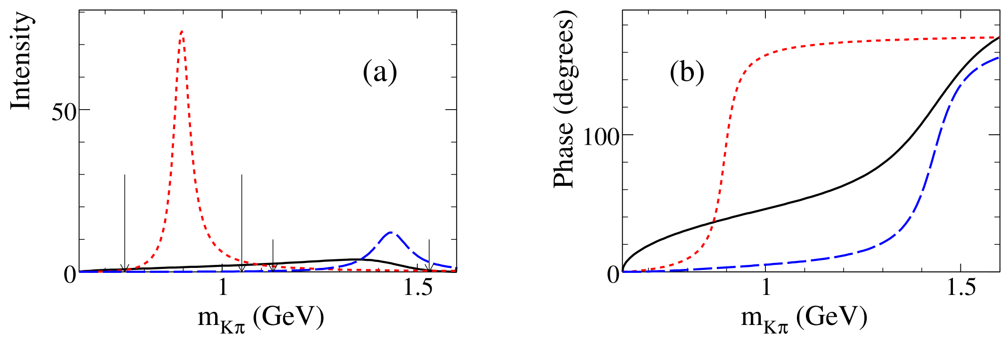

Figure 3.2: Intensity $|M_J(m_{K\pi})|^2$ (a) and phase arg($M_J(m_{K\pi})$) (b) of the invariant amplitudes for $J = 0$ (solid), $J = 1$ (dashed), and $J = 2$ (long-dashed) $K\pi$ contributions as a function of the invariant $K\pi$ mass $m_{K\pi}$. The taller two arrows indicate the low $m_{K\pi}$ region, while the shorter two arrows indicate the high $m_{K\pi}$ region. The relative intensity of the amplitudes is taken from the results described in Table 4.1, while the absolute intensity is shown in arbitrary units.

for the parameters of the $J = 0$ contribution and for the interaction radius [68–70]. The values of m_0, Γ_0, a, and b used in this analysis are listed in Table 3.1. They are different from those quoted in Ref. [68, 69] due to better handling of the fit to the LASS data [70]. The two sets of values are consistent within errors and lead to similar results.

In order to properly account for the three-body kinematics in the analysis of decays $B \to \varphi K\pi$, the amplitude squared $|M_J(m)|^2$ is multiplied by the phase-space factor:

$$F_{\text{Dalitz}}(m_{K\pi}) = 2 \times m_{K\pi} \times \left[m^2_{\max}(m_{K\pi}) - m^2_{\min}(m_{K\pi})\right] , \tag{3.28}$$

where $m^2_{\max}$ and $m^2_{\min}$ are the maximum and minimum values of the Dalitz plot range

Table 3.1: Parameters in the $m_{K\pi}$ distribution for $(K\pi)^*_0$ from the LASS experiment [68,69].

parameter	notation	value
resonance mass	m_0	$1435 \pm 5 \pm 5$
resonance width	Γ_0	$279 \pm 6 \pm 21$
scattering length	a	$1.95 \pm 0.09 \pm 0.06$
effective range	r	$1.76 \pm 0.36 \pm 0.67$

of $m^2_{\varphi K}$ at any given value of $m_{K\pi}$ (see kinematics section of Ref. [56]) with a uniform population on the Dalitz plot over $m^2_{\varphi K}$. The $2 \times m_{K\pi}$ factor comes from the $d(m^2_{K\pi})$ transformation. Due to slow dependence of the factor in Eq. (3.28) on $m_{K\pi}$ in any small range of $m_{K\pi}$, the difference of this approach from the quasi-two-body approximation (without the Dalitz plot phase-space factor) is small.

3.2.2 $K\pi\pi$ Invariant Mass Distributions

The three-body decays $K_J^{(*)} \to K\pi\pi$ of $K_J^{(*)}$ usually proceed through two-body sequential decays. The Breit-Wigner model described in the previous subsection is only an approximation to describe the $K\pi\pi$ invariant mass amplitude. Since most of the three body decays of $K_J^{(*)}$ have contributions from the subchannel $K^*(892)\pi$ (except for the K_2), the $K\pi\pi$ invariant mass amplitudes are parameterized with the spin-J $K^*(892)\pi$ Breit-Wigner shapes defined in Eqs. (3.14). The $K_1(1400)$ and $K^*(1410)$ decay dominantly through the

$K^*(892)\pi$ subchannel, while the $K_1(1270)$ also decays through two other subchannels $K\rho$ and $K_0^*(1430)$. The decays of $K_2(1820)$ and $K_2(1770)$ are not known. The only input is that the $K_2(1770)$ decays dominantly through $K_2^*(1430)\pi$. However, no additional Breit-Wigner models are implemented for these three types sequential decays. Instead, the Geant Based [71] Monte Carlo simulation data is used to tune on the interaction radius r to match the tail of the shape in those two cases.

In the $K^*(892)\pi$ mass B-W parameterization, J reflects the orbital angular momentum of K^* around π in the $K_J^{(*)} \to K^*(892)\pi$ decay. Unlike the two-body decays $K_J^* \to K\pi$, J is not fixed in the three-body decays $K_J^{(*)} \to K\pi\pi$, or necessarily equal to the spin of the K_J^*. Rather, the values of J are constrained by the parity conservation in the decays $K_J^* \to K\pi\pi$. From partial wave analysis, one can obtain $J = 1$ for the decay $K^*(1410) \to K^*(892)\pi$, and $J = 2$ for the decays $K_2^*(1430) \to K^*(892)\pi$ and $K_2 \to K_2(1430)^*\pi$. For the axial-vector decays $K_1 \to K^*(892)\pi$, $J = 0,\ 2$ with the S-wave expected to dominate.

3.3 Interference Effects

The differential decay widths of $B \to \varphi K_J^{(*)}$ described by Eqs. (3.1) and (3.7) involve interference terms between different $K_J^{(*)}$ resonances. These interference terms have unique angular and mass dependences which cannot be factorized in the full distribution. They play important roles in the angular measurements. The effects to the branching fraction measurements have a strong dependence on the relative size of the two interfering amplitudes. Maximum interference effects are observed for the two decays with equal branching fractions.

In the lower $K\pi$ mass range ($1.13 < m_{K\pi} < 1.53$ GeV) or ($1.10 < m_{K\pi} < 1.60$ GeV) of decays $B \to \varphi K_J^*$, the overlap between the $S-$wave $(K\pi)_0^*$ and $D-$wave $K_2^*(1430)$ contributions is large, while the overlap between the $P-$wave $K^*(892)$ and $D-$wave $K_2^*(1430)$ contributions is negligible, as shown in Fig. 3.2.1. From the previous results in [15], the yields of decays $B \to \varphi K_2^*(1430)$ and $B \to \varphi(K\pi)_0^*$ are expected to be close, which leads to a non-negligible interference effect in both the angular and branching fraction measurements.

Non-trivial interference effects are also present between the $\varphi K^*(1680)^0$, $\varphi K_3^*(1780)^0$ and $\varphi K_4^*(2045)^0$ in the higher $K\pi$ mass range ($1.60 < m_{K\pi} < 2.10$ GeV) of decays $B^0 \to \varphi K_J^{*0}$, and between $\varphi K_1(1270)$ and $\varphi K_1(1400)$, $\varphi K_2(1770)$ and $\varphi K_2(1820)$ in the decays $B^+ \to \varphi K^+\pi^+\pi-$. However, there is no prediction of the branching fraction of any of these modes, these interference effects are temporarily ignored. If enough signal events are observed, the fit would be remodeled to include the interference terms. Otherwise, the interference effects will be accounted in the systematic uncertainties.

The interference between decays $B \to \varphi K_2^*(1430)$ and $\varphi(K\pi)_0^*$ is discussed as the following. However the formalism can be easily adapted to describe the interference between any two $K_J^{(*)}$ resonances. The mass and angular amplitude for spin state $J = 0, 2$

are parametrized as

$$A_0(m_{K\pi},\theta_1,\theta_2,\Phi) = Y_0^0(\mathcal{H}_1,\Phi)Y_1^0(-\mathcal{H}_2,0)M_0(m_{K\pi})A_{00} \tag{3.29}$$

$$A_2(m_{K\pi},\theta_1,\theta_2,\Phi) = \sum_{\lambda=0,\pm1} Y_2^{\lambda}(\mathcal{H}_1,\Phi)Y_1^{-\lambda}(-\mathcal{H}_2,0)M_2(m_{K\pi})A_{2\lambda}. \tag{3.30}$$

The interference term appears as $2\Re e(A_0(m_{K\pi},\theta_1,\theta_2,\Phi)A_2^*(m_{K\pi},\theta_1,\theta_2,\Phi))$. The resulting two interference terms, properly normalized, are defined as

$$\frac{2\Re e(A_J A_0^*)}{\sqrt{\Sigma|A_{J\lambda}|^2}|A_{00}|} = \sum_{i=1}^{3}\beta_{iJ}(m_{K\pi})\, f_{iJ}(\mathcal{H}_1,\,\mathcal{H}_2,\,\Phi)\,. \tag{3.31}$$

For $J=2$, the angular dependent terms f_{iJ} are defined as

$$f_{1J} = (3\mathcal{H}_1^2-1)\mathcal{H}_2^2 \tag{3.32}$$

$$f_{2J} = \sqrt{6}\sqrt{1-\mathcal{H}_1^2}\,\mathcal{H}_1\sqrt{1-\mathcal{H}_2^2}\,\mathcal{H}_2\cos\Phi \tag{3.33}$$

$$f_{3J} = -\sqrt{6}\sqrt{1-\mathcal{H}_1^2}\,\mathcal{H}_1\sqrt{1-\mathcal{H}_2^2}\,\mathcal{H}_2\sin\Phi \tag{3.34}$$

Only the f_{10J} term Eq. (3.32) remains if the Φ angle is integrated out. The mass dependent terms $\beta_{iJ}(m_{K\pi})$ are defined for $i=1,2,3$ as:

$$\beta_{1J}(m_{K\pi}) = \sqrt{f_{LJ}}\,\Re e(M_J(m_{K\pi})M_0^*(m_{K\pi})e^{-i\delta_{0J}}) \tag{3.35}$$

$$\beta_{2J}(m_{K\pi}) = \sqrt{1-f_{LJ}f_{\perp J}}\,\Re e(M_J(m_{K\pi})M_0^*(m_{K\pi})e^{i\phi_{\parallel J}}e^{-i\delta_{0J}}) \tag{3.36}$$

$$\beta_{3J}(m_{K\pi}) = \sqrt{f_{\perp J}}\,\Im m(M_J(m_{K\pi})M_0^*(m_{K\pi})e^{i\phi_{\perp J}}e^{-i\delta_{0J}}). \tag{3.37}$$

The $K\pi$ invariant mass distributions $M_0(m_{K\pi})$ and $M_2(m_{K\pi})$ are described by the LASS shape parameterization Eq. (3.27) and relativistic Breit-Wigner function Eq. (3.18) respectively. The δ_{0J} is defined as the relative phase between the $S-$wave and $D-$wave $K\pi$

invariant mass amplitudes. The main difference now is that the interference terms β_i have a different dependence on mass to the α_i in Eq. (3.2). This dependence now includes the phase of the resonance amplitude as a function of mass and becomes crucial in resolving the phase ambiguities.

From Eq. (3.2), for any given set of values $(\phi_{\parallel J}, \phi_{\perp J}, \Delta\phi_{\parallel J}, \Delta\phi_{\perp J})$ a simple transformation of phases, for example $(2\pi - \phi_{\parallel J}, \pi - \phi_{\perp J}, -\Delta\phi_{\parallel J}, -\Delta\phi_{\perp J})$, gives rise to another set of values that satisfy the decay rates Eqs. (3.1) and (3.7) in an identical manner. This results in a four-fold ambiguity (two-fold for each of B^0 and $\overline{B}^0$ decays). At any given value of $m_{K\pi}$ the distributions, including the interference terms in Eqs. (3.36) and (3.37), are still invariant under the above transformations if one flips the sign of the phase, arg$(M_J(m_{K\pi})M_0^*(m_{K\pi})e^{-i\delta_{0J}^{\pm}})$. At a given value of $m_{K\pi}$ this phase has to be determined from the data that leads to the ambiguity as well. However, the mass dependence of this phase is unique, given that the parameters $\delta_{0J}^{\pm}$ are constant. Therefore, the two ambiguous solutions for each B^0 and $\overline{B}^0$ decay can be fully resolved from the $m_{K\pi}$ dependence of the angular distributions in Eq. (3.31).

This technique of resolving the two ambiguous solutions in $B \to VV$ decays has been introduced in the analysis of $B^0 \to J/\psi K^{*0}$ decays [**?**]. It is based on Wigner's causality principle [76], where the phase of a resonant amplitude increases with increasing invariant mass, see Eq. (3.14). As a result, both the P-wave and D-wave resonance phase shifts increase rapidly in the vicinity of the resonance, while the corresponding S-wave increases only gradually, as seen in Fig. 3.2.1.

3.4 Event Reconstruction

3.4.1 Data and Monte Carlo Samples

The analyses on decays $B^0 \to \varphi K_J^{*0}(K^+\pi^-)$ in the lower $K\pi$ mass range $(1.13-1.53)$ GeV and decays $B^+ \to \varphi K_J^{(*)+}$ are based on the complete data sample of about 465 million $B\overline{B}$ pairs recorded at *BABAR*, corresponding to an integrated luminosity of 426 $\mathtt{fb}^{-1}$. The analysis on decays $B^0 \to \varphi K_J^{*0}(K^+\pi^-)$ in the higher $K\pi$ mass range $(1.60-2.10)$ GeV is based on the data taken during 1999-2006 of 384 million $B\overline{B}$ pairs and an integrated luminosity of 347 $\mathtt{fb}^{-1}$, shown in Fig. 2.2.

The raw data recorded by the detector is processed by dedicated reconstruction farms, with the output written to an event-store database. Inside the database the reconstructed events are grouped into collections, which are the basic units for *BABAR* users to perform analysis. The most general one is the collection called `AllEvents`, which contains all events passing a loose physics selection. The events of interests are further refined on the analysis level by creating exclusive skims, being the subsets of the `AllEvents` collection. For the analyses on decays $B \to \varphi K\pi$, our selection is based on skims BFourHHHH, BFourHHHK and BFourHHHP (see Table 3.2) which retain all B-decay candidates with four tracks ($K^{\pm}$ or $\pi^{\pm}$), neutral particles K_S^0 and neutral particles π^0. For the analysis

$B \to \varphi K\pi\pi$, skim InclPhi, which selects all B-decay candidates with a high-momentum φ meson is used. The BFourHHHX skim covers the complete $K\pi$ mass spectrum allowed in the $B \to \varphi K\pi$ phase space, while the φ momentum requirement in InclPhi skim limits the $K\pi\pi$ mass spectrum in the phase space. But this limit does not affect the analysis described here.

Table 3.2: List of topologies and skims used in analysis on $B \to \varphi K_J^{(*)}$.

topology	final state	skim
$B \to h^+h^-h^+h^-$	$B^0 \to \varphi K^{*0}(K^+\pi^-)$	BFourHHHH
$B \to h^+h^-h^\pm K_S^0$	$B^+ \to \varphi K^{*+}(K^0\pi^+)$	BFourHHHK
$B \to h^+h^-h^\pm \pi^0$	$B^+ \to \varphi K^{*+}(K^+\pi^0)$	BFourHHHP
$B \to \varphi X$	$B^+ \to \varphi K_J^{(*)+}(K^+\pi^+\pi^-)$	InclPhi

In addition to the data recorded from the detector, a large number of Monte Carlo (MC) events are generated to simulate detector data, for the purpose of both detector study and the physics measurements. The event generators are used to simulate various physics processes, such as `EvtGen+Jetset` for the $B\overline{B}$ physics and the $usdc$ continuum events. The simulation of the trajectories of the final state particles in the detector is based on `Geant4` [71], while the detector response is simulated with digitization. Table 3.3 summarizes the important MC samples used in the analyses described here.

Table 3.3: Summary of MC samples. The polarization f_L is quoted when relevant. The longitudinal and transverse modes are grouped together.

Decay channel	Mode number	Generated Events (k)	f_L
B^+B^- generic	1235	641198	–
$B^0\overline{B}^0$ generic	1237	652510	–
Weighted $B^0 \to D\,X$ and D^*X	2222	70122	–
$B^0 \to \varphi K^*(892)^0$, ln (tr)	2296 (2297)	292 (292)	1.0 (0.0)
$B^0 \to \varphi K_2^*(1430)^0$, ln (tr)	6840 (6931)	619 (619)	1.0 (0.0)
$B^0 \to \varphi K_2^*(1430)^0$, angle3	6932	619	0.741
$B^0 \to \varphi K_2^*(1430)^0$, angle4	6964	619	0.5
$B^0 \to \varphi K_0^*(1430)^0$	6924	619	–
$B^0 \to \varphi K^*(1680)^0$, ln (tr)	7239 (7240)	704 (704)	1.0 (0.0)
$B^0 \to \varphi K_3^*(1780)^0$, ln (tr)	7241 (7242)	704 (704)	1.0 (0.0)
$B^0 \to \varphi K_4^*(2045)^0$, ln (tr)	7243 (7244)	704 (704)	1.0 (0.0)
$B^+ \to \varphi K^*(1410)^+$, ln (tr)	7249 (7250)	778 (778)	1.0 (0.0)
$B^+ \to \varphi K_2^*(1430)^+$, ln (tr)	7251 (7252)	778 (778)	1.0 (0.0)
$B^+ \to \varphi K_1(1270)^+$, ln (tr)	7816 (7817)	778 (778)	1.0 (0.0)
$B^+ \to \varphi K_1(1400)^+$, ln (tr)	7960 (7961)	778 (778)	1.0 (0.0)
$B^+ \to \varphi K_2(1770)^+$, ln (tr)	8254 (8255)	827 (827)	1.0 (0.0)
$B^+ \to \varphi K_2(1820)^+$, ln (tr)	8256 (8257)	827 (827)	1.0 (0.0)

3.4.2 Kinematic Selections

In the reconstruction the charged tracks (except those from $K^0_S \to \pi^+\pi^-$) are produced by the CompositionTools (Table 3.4). The electrons are vetoed by demanding that the charged tracks have DIRC, EMC, and IFR signatures inconsistent with electrons. Further pion and Kaon PID requirements are based on a likelihood selection developed from dE/dx and Cherenkov angle information from the tracking detectors and DIRC, respectively. The typical efficiency of PID requirements is >95% for charged tracks in our final states. The K^0_S and π^0 selections, discussed in Sec. 2.4.2, yield purity 92% (88%) and 90% (68%), respectively, in the signal sample (combinatorial background) based on MC studies.

The B meson candidatesare identified kinematically using two nearly independent variables, the energy-substituted mass and energy constraint:

$$m_{\rm ES} = [(s/2 + \mathbf{p}_i \cdot \mathbf{p}_B)^2/E_i^2 - \mathbf{p}_B^2]^{1/2} , \tag{3.38}$$

$$\Delta E = (E_i E_B - \mathbf{p}_i \cdot \mathbf{p}_B - s/2)/\sqrt{s} , \tag{3.39}$$

where $(E_i, \mathbf{p}_i)$ is the initial state four-momentum, obtained from the beam momenta, and $(E_B, \mathbf{p}_B)$ is the four-momentum of the reconstructed B candidate. For signal events $m_{\rm ES}$ peaks at the B mass and ΔE near zero. The typical $m_{\rm ES}$ resolution is 2.6 MeV and is dominated by the beam energy uncertainties. The ΔE resolution is dominated by the energy and momentum measurements of the decay products. It is typically 34 and 20 MeV for the subchannels with and without a π^0, respectively. The requirement of $m_{\rm ES} > 5.25$ GeV and $|\Delta E| < 0.1$ GeV is applied to retain sidebands for later fitting of parameters to describe

Table 3.4: List of tracks produced by CompositionTools and used in the reconstruction code. The d and z represent the closest distance of the track from the nominal beam spot in the $x-y$ plane and z direction respectively.

particle	particle list	Requirement
$h^{\pm}$ from $K_J^{(*)}$	GoodTracksVeryLoose(GVL)	$p < 10$ GeV/c $d < 1.5$ cm $z < 10$ cm
$K^{\pm}$ from φ	GoodTracksLoose(GL)	all GVL requirements $p_T > 100$ MeV/c $>$ 12 DCH hits
rest of event	GoodTracksVeryLoose	
	CalorNeutral	Any neutral cluster in the EMC

the backgrounds. For decays $B^+ \to \varphi K_J^{(*+)} \to (K^+K^-)(K^+\pi^+\pi^-)$, tighter requirement $|\Delta E| \leq 0.08$ GeV is applied to optimize the signal to background ratio.

The dominant light quark-antiquark ($q\bar{q}$) background is rejected by the cut $|\cos\theta_T| < 0.8$, where θ_T is the angle between the B-candidate thrust axis and that of the rest of the event, calculated in the c.m. frame. The distribution of $|\cos\theta_T|$ is sharply peaked near 1 for combinations drawn from the jet-like $q\bar{q}$ pairs and is nearly uniform for the isotropic B-meson decays. The angle θ_T is the most powerful of the event shape variables. Further use of the event topology is made via the construction of a Fisher discriminant $\mathcal{F}$, which is subsequently used as a discriminating variable in the likelihood fit.

Our Fisher discriminant is an optimized linear combination of the remaining event shape information excluding $\cos\theta_T$. The variables entering the Fisher discriminant are the angles with respect to the beam axis of the B momentum and B thrust axis and the zeroth and second angular moments $L_{0,2}$ of the energy flow about the B thrust axis, all calculated in the $\Upsilon(4S)$ center-of-mass frame. The moments are defined by

$$L_j = \sum_i p_i \times |\cos\theta_i|^j \ , \tag{3.40}$$

where θ_i is the angle with respect to the B thrust axis of track or neutral cluster i, p_i is its momentum, and the sum excludes the B candidate. The coefficients used to combine these variables are chosen to maximize the separation (difference of means divided by quadrature sum of errors) between the signal and continuum background distributions of L_j, and are determined from studies of signal MC and off-peak data. The optimization of $\mathcal{F}$ has been studied for a variety of signal modes, and find that the optimal sets of coefficients are nearly identical for all. Because the information contained in $\mathcal{F}$ is correlated with $|\cos\theta_T|$, the separation between signal and background is dependent on the $|\cos\theta_T|$ requirement made prior to the formation of $\mathcal{F}$. The events with badly formed Fisher discriminant in the tails of the distributions are rejected by the cut $|\mathcal{F}| \leq 2$, as shown in Fig. 3.16.

The φ and $K_J^{(*)}$ candidates are selected with requirements on their invariant masses loose enough to retain sidebands for later fitting. The K^+K^- invariant mass selection follows $0.990 \leq m_2 \equiv m_{K^+K^-} \leq 1.050$ (GeV). The $K\pi$ and $K\pi\pi$ invariant mass selections are the following:

- $B^0 \to \varphi K_J^{*0} \to (K^+K^-)(K^+\pi^-)$: $1.13 \leq m_1 \equiv m_{K\pi} \leq 1.53$ (GeV), or $1.60 \leq m_1 \equiv m_{K\pi} \leq 2.15$ (GeV);
- $B^+ \to \varphi K_J^{*+} \to (K^+K^-)(K_S^0\pi^+)$: $1.10 \leq m_{K\pi} \leq 1.60$ GeV;
- $B^+ \to \varphi K_J^{*+} \to (K^+K^-)(K^+\pi^0)$: $1.10 \leq m_{K\pi} \leq 1.60$ GeV, $\cos\theta_1 \equiv \mathcal{H}_1 \leq 0.6$;
- $B^+ \to \varphi K_J^{*+} \to (K^+K^-)(K^+\pi^+\pi^-)$: $1.10 \leq m_{K\pi\pi} \leq 2.15$ GeV.

The signal candidates that have decay products with invariant mass within 12 MeV of the nominal mass values for D_s^+ or $D^+ \to \varphi\pi^+$ are removed. This kinematic cut introduces acceptance effects in the $\mathcal{H}_1$ distribution, see more detail in Ref. [15], and is accounted for in the maximum likelihood fit parameterization.

The B candidate vertex is fitted and requirement of $\chi^2_{\text{vertex}} < 50$ is applied. Occasionally, more than one candidate are reconstructed for an event. It happens in $(5\% - 9\%)$ of $\varphi K^+\pi^-$, 8% of $\varphi K^0_S\pi^+$, 3% of $\varphi K^+\pi^0$ and 15% of $\varphi K^+\pi^+\pi^-$ events. Only one candidate is selected per event based on the lowest value of the χ^2 of the charged-track vertex fit in decays $B^0 \to \varphi K^+\pi^-$ and $B^+ \to \varphi K^+\pi^+\pi^-$, or the χ^2 of invariant mass consistency of the K^0_S or π^0 for decays $B^+ \to \varphi K^0_S\pi^+/K^+\pi^0$.

3.5 Background Estimation

The events passing the selections described in the previous section contain the potential signal modes described in Table 3.5. The dominant background is from the $e^+e^- \to q\bar{q}$ decays. The background from the B-meson decays, namely $B-$background, is generally found small due to selection on the narrow φ resonance, particle identification on three kaons and good momentum resolution (in particular for ΔE). Some level of random B background is inevitable and can be treated as combinatorial background.

The nonresonant contribution is taken into account naturally in the fit with both $K\overline{K}$ and $K\pi(\pi)$ contributions allowed to vary. The $K\overline{K}K^{(*)}_J$ contribution is modeled as $f_0(K\pi)^{*0}_0$ or $f_0K^*(1680)^0$ in the lower or higher mass ranges of B^0-decays, and $f_0K_1(1400)^+$ in the B^+-decays. The $\varphi K\pi(\pi)$ contribution is a part of the S-wave $K\pi$ in the $\varphi K^0_S\pi^+$ and $\varphi K^+\pi^0$ final states, while $\varphi K^{*0}\pi^+$ decay is assumed for the $B^+ \to \varphi K^+\pi^+\pi^-$ mode.

To estimate the effect of the $B-$meson decays which could mimic signal, a full

GEANT4-based MC simulation of the $\Upsilon(4S) \to B\overline{B}$ events with a size three times of that from data is studied. The categories of events which may have ΔE and $m_{\rm ES}$ distributions similar to signal are fitted. The signal yields are found to be consistent with 0. These events are later embedded into the data sample, with the observed variations to the fit results are accounted for as systematic errors.

The selected signal $B \to \varphi K_J^{(*)}$ events contain a small fraction of incorrectly reconstructed candidates. Misreconstruction occurs when at least one candidate track belongs to the decay products of the other B from the $\Upsilon(4S)$ decay, which happens in about 5% of the cases in the decays $B \to \varphi K^+\pi^-$ and $B \to \varphi K^+\pi^0$, about (7 - 12)% in decays $B \to \phi K^0_S\pi^+$, and about (11 - 22)% in five-body decays $B \to \varphi K^+\pi^+\pi^-$. The distributions that show peaks for correctly reconstructed events have substantial tails, with large uncertainties in MC simulation, when misreconstructed events are included. These tails and incorrect angular dependence would reduce the power of the distributions to discriminate between the background and the collection of correctly and incorrectly reconstructed events. Therefore, only the correctly reconstructed candidates is represented in the signal PDF and both the correctly reconstructed and misreconstructed MC events are included to calculate the reconstruction efficiency.

3.6 Extended Maximum Likelihood Fit

The events passing the selection criteria described in Sec. 3.4 are grouped into five final states, shown in Table 3.5. For each selected event, nine (eight) primary observables $\vec{x}_i$= $\{$ $m_{\rm ES}$, ΔE, $\mathcal{F}$, $m_{K\pi\pi}$, m_{KK}, $\mathcal{H}_1$, $\mathcal{H}_2$, (Φ), $Q\}$ are constructed as used as the input to the unbinned, extended maximum-likelihood (ML) fits [14] to extract the measurements in Table 1.5. Due to the relatively low statistics, the angular analyses in all decay modes are simplified except for $B^0 \to \varphi K^+\pi^-$ in the range ($1.13 < m_{K\pi} < 1.53$ GeV). The simplified angular analysis is also called partial angular analysis, since the observable Φ is excluded as being integrated it out from the angular distributions in Eqs. (3.1) and (3.7).

3.6.1 Likelihood Functions

The extended likelihood function for a sample of $N_{\tt cand}$ candidates can be written as:

$$\mathcal{L}_m = \exp\left(-\sum_j n_j\right) \prod_i^{N_{\tt cand}} \left(\sum_{j,k} n_j^k\, \mathcal{P}_j^k(\vec{\rm x}_i;\ \mu^k,\ \vec{\zeta},\ \vec{\xi}).\right) \tag{3.41}$$

The index $m = 1 - 5$ represents five final states, listed in Table 3.5; the index j for the event types used in our data model for each final state, the signal decays $B \to \varphi K_J^{(*)}$, B-Backgrounds, and the dominant $q\bar{q}$ combinatorial background, listed in Table 3.5; and the superscript k corresponds to the value of the flavor sign $Q = \pm 1$, which allows for a CP-violating difference between the B^0 and $\overline{B}^0$ decay amplitudes (A and $\overline{A}$). The n_j^k is the event yield for a given event type j and flavor k, and the $\mathcal{P}_j^k(\vec{\rm x}_i;\, \mu^k,\, \vec{\zeta};\, \vec{\xi})$ is the probability density function (PDF) to be discussed in the next subsection.

The polarization parameters $\vec{\zeta}$ are only relevant for the signal PDF. In the full angular analysis, $\vec{\zeta} \equiv \{f_{LJ}, f_{\perp J}, \phi_{\parallel J}, \phi_{\perp J}, \delta_{0J}, \mathcal{A}^0_{CPJ}, \mathcal{A}^{\perp}_{CPJ}, \Delta\phi_{\parallel J}, \Delta\phi_{\perp J}, \Delta\delta_{0J}\}$, while in the partial angular analysis $\vec{\zeta} \equiv \{f_{LJ}, \delta_{0J}, \mathcal{A}^0_{CPJ}, \Delta\delta_{0J}\}$. The remaining PDF parameters $\vec{\xi}$, in all five final states are left free to vary in the fit for the combinatorial background and are fixed to the values extracted from MC simulation and calibration $B \to \overline{D}\pi$ decays for the other event types.

Due to the non-negligible interference effects, the $B \to \varphi K_2^*(1430)$ and $B \to \varphi(K\pi)_0^*$ modes are combined using the fraction μ^k. The yield and asymmetry, $n_{\rm sig}$ and $\mathcal{A}_{CP}$, of the $B^0 \to \varphi K_2^*(1430)$ and those $B^0 \to \varphi(K^+\pi^-)_0^{*0}$ modes are parameterized by applying the fraction μ^k of the $\varphi(K\pi)_J$ yield to n_1^k. Hence, $n_{\rm sig} = n_1^+ \times \mu^+ + n_1^- \times \mu^-$, $\mathcal{A}_{CP} = (n_1^+ \times \mu^+ - n_1^- \times \mu^-)/n_{\rm sig}$, and the $\varphi(K^\pm\pi^\mp)_0^{*0}$ yield is $n_1^+ \times (1-\mu^+) + n_1^- \times (1-\mu^-)$. This treatment is necessary to include interference between the two decay modes as discussed below. The interferences between the other final states are ignored due to low statistics.

For decays in $(K^+K^-K^+\pi^-)$ final states two ML fits based on likelihood functions $\mathcal{L}_1$ and $\mathcal{L}_2$ are implemented for the lower (1.13 - 1.53 GeV) and higher (1.60 - 2.15 GeV) $K\pi$ invariant mass ranges. Since the $K_2^*(1430)^+$ meson contributes to three $K^0\pi^+$, $K^+\pi^0$, and $K^+\pi^+\pi^-$ final states and $(K\pi)_0^{*+}$ contributes to two $K\pi$ final states, a joint fit is implemented to the data of all three final states. The total likelihood is defined as $\mathcal{L} = \prod_{i=3,4,5} \mathcal{L}_i$. In the joint fit all signal parameters other than the signal yields in Table 1.5 are

Table 3.5: The datasets passing the preliminary kinematic selections. Aside from the $B-$decay event types listed here, there exists a common combinatorial background $q\bar{q}$ in each final state. The $\varphi(K\pi)_{0,2}$ is the sum of $\varphi K_2^*(1430)$ and $\varphi(K\pi)_0^*$ modes. †: The $\varphi K_2(1770)^+$ mode is also considered in place of $\varphi K_2(1820)^+$.

	Final State	$m_{K\pi(\pi)}$ Range	$N_{\texttt{cand}}$	Signal	B-Background
1	$K^+K^-K^+\pi^-$	(1.13 - 1.53) GeV	7050	$\varphi(K\pi)^0_{0,2}$	$f_0(K\pi)^{*0}_0$
2	$K^+K^-K^+\pi^-$	(1.60 - 2.15) GeV	38808	$\varphi K^*(1680)^0$ $\varphi K_3^*(1780)^0$ $\varphi K_4^*(2045)^0$ $\varphi\overline{D}^0$	$f_0K^*(1680)^0$ $\varphi K^+\pi^-$ $f_0\overline{D}^0$
3	$K^+K^-K^0_S\pi^+$	(1.10 - 1.60) GeV	1943	$\varphi(K\pi)^+_{0,2}$	$f_0K^*(892)^+$
4	$K^+K^-K^+\pi^0$	(1.10 - 1.60) GeV	2511	$\varphi(K\pi)^+_{0,2}$	$f_0K^*(892)^+$
5	$K^+K^-K^+\pi^+\pi^-$	(1.10 - 2.10) GeV	4145	$\varphi K_1(1270)^+$ $\varphi K_1(1400)^+$ $\varphi K^*(1410)^+$ $\varphi K_2^*(1430)^+$ $\varphi K_2(1820)^{+\dagger}$	$f_0K_1(1400)^+$ $\varphi K^+\pi^+\pi^-$

constrained to be the same when they appear in multiple channels. Any isospin violation is negligible and thus is ignored.

The corresponding $\varphi K_2^*(1430)^+$ and $\varphi(K\pi)_0^+$ yields $n^k_{\mathtt{sig}J}$ in different final states are related by the relative efficiencies Eqs. (3.42-3.44), taking into account the isospin relationship, daughter branching fractions, and reconstruction efficiency corrections.

$$\begin{aligned} r_1 &= \frac{\mathcal{E}_{\mathtt{sig2}}(K^0_S\pi^+)}{\mathcal{E}_{\mathtt{sig2}}(K^+\pi^0)} = \frac{n_{\mathtt{sig2}}(K^0_S\pi^+)}{n_{\mathtt{sig2}}(K^+\pi^0)} \qquad (3.42)\\ r_2 &= \frac{\mathcal{E}_{\mathtt{sig0}}(K^0_S\pi^+)}{\mathcal{E}_{\mathtt{sig0}}(K^+\pi^0)} = \frac{n_{\mathtt{sig0}}(K^0_S\pi^+)}{n_{\mathtt{sig0}}(K^+\pi^0)} \qquad (3.43)\\ r_3 &= \frac{\mathcal{E}_{\mathtt{sig2}}(K^+\pi^+\pi^-)}{\mathcal{E}_{\mathtt{sig2}}(K^+\pi^0)} = \frac{n_{\mathtt{sig2}}(K^+\pi^+\pi^-)}{n_{\mathtt{sig2}}(K^+\pi^0)} \qquad (3.44)\end{aligned}$$

In the joint fit only two parameters are floated. One is the combined yield $n^k_{\mathtt{tot}}$ of the $\varphi K^*_{0,2}(1430)$ modes in $K^0_S\pi^+$ and $K^+\pi^0$ final states. And the other is the $\varphi K_2^*(1430)$ yield fraction μ^k in the $K^0_S\pi^+$ final state. The yields $n^k_{\mathtt{sig}J}$ in the final state $K^0_S\pi^+$ can be written as:

$$\begin{aligned} n^k_{\mathtt{sig2}} &= \frac{n_{\mathtt{tot}}\ \mu^k\ r_1\ r_2}{\mu^k\ (r_2-r_1)+r_1(r_2+1)} \qquad (3.45)\\ n^k_{\mathtt{sig0}} &= \frac{n_{\mathtt{tot}}\ (1-\mu^k)\ r_1\ r_2}{\mu^k\ (r_2-r_1)+r_1(r_2+1)} \qquad (3.46)\end{aligned}$$

In the joint fit implementation, the input parameters are defined as:

$$a_1 = n_{\mathtt{tot}}\,, a_2 = \frac{n^+_{\mathtt{tot}}}{n^+_{\mathtt{tot}}+n^-_{\mathtt{tot}}}\,, a_3 = \mu^+\,, a_4 = \mu^-. \qquad (3.47)$$

With two additional constants $c_1 = r_2 - r_1\,, c_2 = r_1(r_2+1)$, the yields $n_{\mathtt{sig}J}$ in $K^0_S\pi^+$ final state and the overall CP asymmetries $\mathcal{A}_{CPJ}$ can be written as:

$$n_{\mathtt{sig2}} = r_1 r_2 a_1 [\frac{a_2 a_3}{(c_1 a_3 + c_2)} + \frac{(1-a_2)a_4}{c_1 a_4 + c_2}] \tag{3.48}$$

$$n_{\mathtt{sig0}} = r_1 r_2 a_1 [\frac{a_2(1-a_3)}{(c_1 a_3 + c_2)} + \frac{(1-a_2)(1-a_4)}{c_1 a_4 + c_2}] \tag{3.49}$$

$$\mathcal{A}_{CP2} = \frac{2\, a_2 a_3 (c_1 a_4 + c_2)}{c_2[a_2(a_3 - a_4) + a_4] + c_1 a_3 a_4} - 1 \tag{3.50}$$

$$\mathcal{A}_{CP0} = \frac{2\, a_2 (1-a_3)(c_1 a_4 + c_2)}{a_2(1-a_3)(c_1 a_4 + c_2) + (1-a_2)(1-a_4)(c_1 a_3 + c_2)} - 1 \tag{3.51}$$

The yields $n_{\mathtt{sig}J}$ in other final states can be obtained from the Eqs. (3.42-3.44).

In all three ML fits the $-2\ln\mathcal{L}$ functions are minimized using MINUIT [77] in the ROOT framework [78]. The statistical error on a parameter is given by its change when the quantity $-2\ln\mathcal{L}$ increases by one unit. The statistical significance is taken as the square root of the difference between the value of $-2\ln\mathcal{L}$ for zero signal and the value at its minimum. This procedure has been tested with simulated samples, where good agreement with the statistical expectations is found.

3.6.2 PDF Parametrization

The PDF $\mathcal{P}_j^k(\vec{\mathrm{x}}_i;\, \mu^k,\, \vec{\zeta};\, \vec{\xi})$ for a given $B \to \varphi K\pi(\pi)$ candidate i is taken to be a joint PDF for the helicity angles, resonance masses, and Q, and the product of the PDFs for each of the remaining variables $\{m_{\mathrm{ES}}, \Delta E, \mathcal{F}\}$. The assumption of negligible correlations in the selected data sample among the discriminating variables, except for resonance masses and helicity angles where relevant, has been validated by evaluating the correlation coefficients.

This assumption was further tested with the MC simulation.

Double-Gaussian functions are used for the parameterization for signal ΔE and $m_{\rm ES}$ PDFs. Low-degree polynomials are used for the background PDFs as required by the data. In the case of $m_{\rm ES}$ an empirical threshold ARGUS function [79] is used:

$$f(x) \propto x\sqrt{1-x^2}\,\exp[-\xi_1(1-x^2)]\ , \tag{3.52}$$

where $x \equiv m_{\rm ES}/E_{\rm beam}$ and ξ_1 is a parameter that is determined from the fit with a typical value of about 25.

The Fisher distribution $\mathcal{F}$ is described well by a Gaussian function with different widths to the left and right of the mean for both the signal and background. For the combinatorial background distribution, A second Gaussian function with a larger width is used to account for a small tail in the signal $\mathcal{F}$ region. This additional component of the PDF is important because it prevents the background probability from becoming too small in the region where signal lies. Fig. 3.3 shows the PDF parametrizations of the $m_{\rm ES}$, ΔE, and $\mathcal{F}$for the B-decay and $q\bar{q}$ events.

A relativistic spin-J B-W amplitude parameterization is used for the resonance masses [56, 72, 73], except for the $(K\pi)^{*0}_0$ $m_{K\pi}$ amplitude, which is parameterized with the LASS function [68–70]. The latter includes the $K^*_0(1430)^0$ resonance together with a nonresonant component. The detailed treatment of the invariant mass distribution is discussed in Section 3.2. No additional correction to the $K\pi$ invariant mass parameterization is found to be necessary because resolution effects of only a few MeV are negligibly small

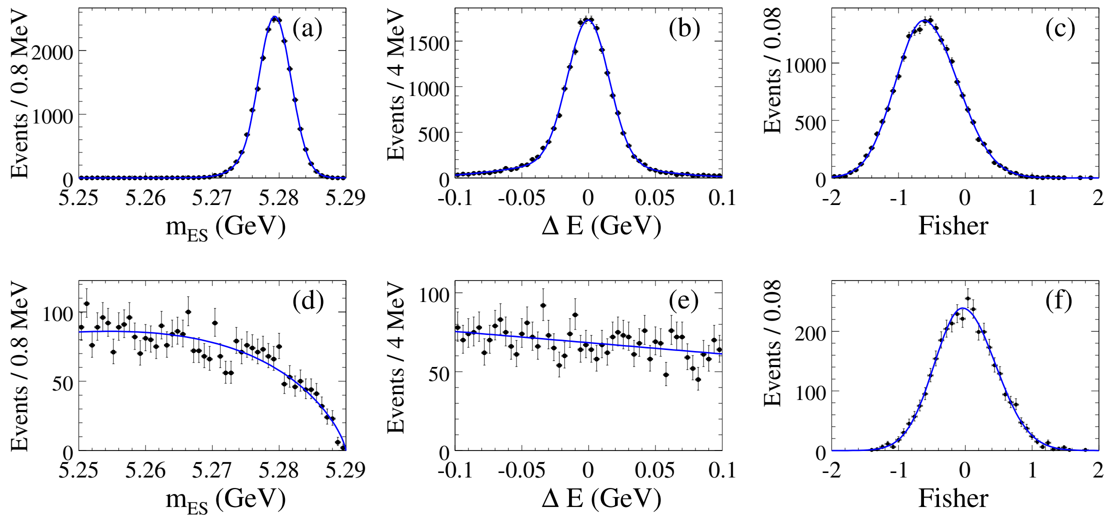

Figure 3.3: PDF parameterizations of $m_{\rm ES}$, ΔE and $\mathcal{F}$ for $B^0 \to \varphi K^+\pi^-$ signal MC (top row) and the combinatorial backgrounds.

compared with the resonance widths. On the other hand, the resolution effects are included in the $m_{K\overline{K}}$ parameterization.

For the combinatorial background we establish the functional forms and initial parameter values of the PDFs with data from sidebands in $m_{\rm ES}$ or ΔE. The main background parameters (excluding the resonance-mass central values and widths) are then redefined by allowing them to vary in the final fit so that they are determined by the full data sample. The background parameterizations for candidate masses include resonant components to account for resonance production in the background. The background shape for the helicity parameterization is also separated into contributions from combinatorial background and from real mesons, both fit by low-degree polynomials.

Fig. 3.4 shows the PDF parameterizations of $m_{K\overline{K}}$ for the mesons φ, $f_0(980)$, and $q\bar{q}$

combinatorial background in the final states $K^+K^-K^+\pi^-$ ($1.13 < m_{K\pi} < 1.53$ GeV) for example. Fig. 3.5 shows the PDF parameterization of $m_{K\pi}$ for the mesons $K^*(892)^0$, $(K\pi)_0^{*0}$, $K_2^*(1430)^0$, $K^*(1680)^0$, $K_3^*(1780)^0$, $K_4^*(2045)^0$ and $\overline{D}^0$ in the MC simultion, and the $q\bar{q}$ combinatorial background in the lower ($1.13 < m_{K\pi} < 1.53$ GeV) and higher ($1.60 < m_{K\pi} < 2.10$ GeV) mass ranges of the data from sidebands. Fig. 3.6 shows the PDF parameterizations of $m_{K\pi\pi}$ for the mesons $K_1(1270)^+$, $K_1(1400)^+$, $K^*(1410)^+$, $K_2^*(1430)^+$ and $K_2(1820)^+$ in the MC simultion, and $q\bar{q}$ combinatorial background for the data from sidebands in the final states $K^+K^-K^+\pi^+\pi^-$.

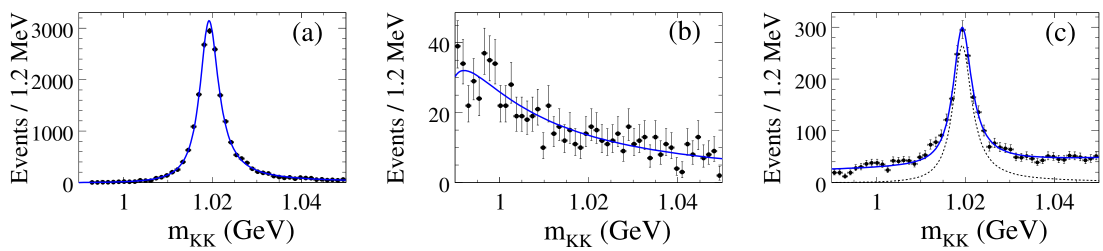

Figure 3.4: PDF parameterizations of $m_{K\overline{K}}$ for φ (a), $f_0(980)$ (b), and combinatorial background (c) in the lower $K^+\pi^-$ mass range of (1.13$-$1.53 GeV. The dashed line in (c) represents the contribution from the real φ.

The mass-helicity PDF is the ideal distribution from Eqs. (3.29–3.31), multiplied by an empirically-determined acceptance function $\mathcal{G}(\mathcal{H}_1, \mathcal{H}_2, \Phi) \equiv \mathcal{G}_1(\mathcal{H}_1) \times \mathcal{G}_2(\mathcal{H}_2)$, which is a parameterization of the relative reconstruction efficiency as a function of helicity angles. It was found with detailed MC simulation that resolution effects in the helicity angles introduce negligible effects in the PDF parameterization and fit performance, and they are therefore ignored. The angles between the final state particles and their parent resonances

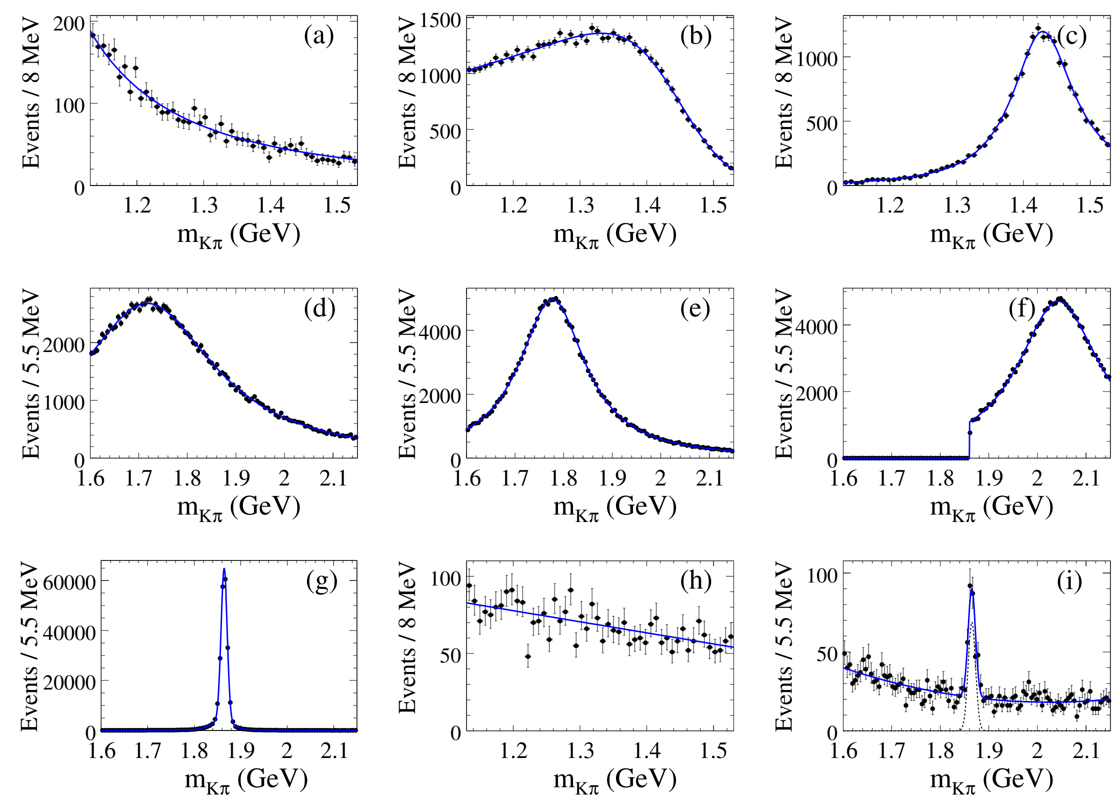

Figure 3.5: PDF parameterizations of $m_{K\pi}$ for resonances $K^*(892)^0$ (a), $(K\pi)^{*0}_0$ (b), $K^*_2(1430)^0$ (c), $K^*(1680)^0$ (d), $K^*_3(1780)^0$ (e), $K^*_4(2045)^0$ (f), $\overline{D}^0$ (g), and $q\bar{q}$ combinatorial background in the lower (h) and higher (i) mass ranges. The dashed line in (i) represents the contribution from the real $\overline{D}^0$ meson. The cut off at 1.86 Gev in (f) is due to the incorrect modelling in the MC. This effect is accounted for the branching fraction calculation and PDF model. The decay width of the D^0 is 1.6×10^{-9} MeV, while the width in (g) for the D^0 meson is mainly due to the detector resolution.

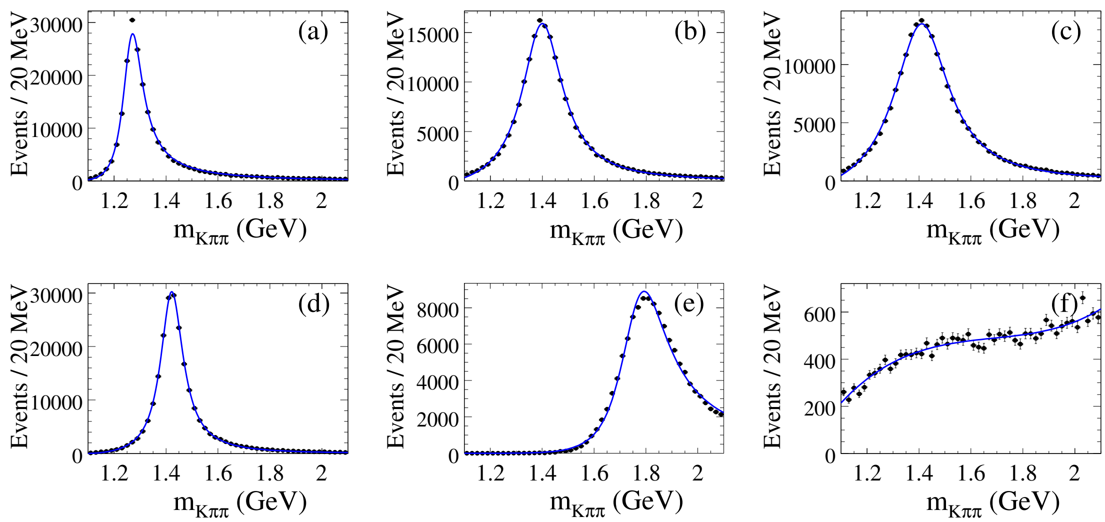

Figure 3.6: PDF parameterizations of $m_{K\pi\pi}$ for resonances $K_1(1270)^+$ (a), $K_1(1400)^+$ (b), $K^*(1410)^+$ (c), $K_2^*(1430)^+$ (d) and $K_2(1820)^+$ (e) in MC simulation, and $q\bar{q}$ combinatorial background (f) for the data from sidebands.

are related to their momenta. The signal acceptance effects parameterized with the function $\mathcal{G}(\mathcal{H}_1, \mathcal{H}_2, \Phi)$ are due to kinematic correlations, whereas the detector geometry correlations are negligible. Therefore, the above uncorrelated parameterization as a function of two helicity angles was found to be appropriate and was validated with detailed MC simulation.

Momentum in the laboratory frame is strongly correlated with detection efficiency, which leads to the acceptance effects in the helicity observables $\mathcal{H}_i$. It is most evident for the large values of $\mathcal{H}_1$ corresponding to the slow π from the K^* meson. However, these acceptance effects are not present for the Φ angle; there is no correlation with the actual direction with respect to the detector, which is random for the B decays. The acceptance effects for the two helicity angles $\mathcal{H}_1$ and $\mathcal{H}_2$ are shown in Fig. 3.7. The acceptance functions are obtained from the fit to the signal MC helicity distribution, with the known relative components of longitudinal and transverse amplitudes generated with MC. The $D^{\pm}_{(s)}$-meson veto causes the sharp acceptance dips around 0.8 in the $\mathcal{G}_1(\mathcal{H}_1)$ function in the $B^0 \to \varphi K^+\pi^-$ analysis.

Fig. 3.8- 3.9 show the PDF parameterizations of $\mathcal{H}_1$ for the decays $B^0 \to \varphi K^{*0}_J(K^+\pi^-)$ and $B^+ \to \varphi K^{*+}_J(K^+\pi^+\pi^-)$ in the MC simultion. The PDF parameterizations of $\mathcal{H}_1$ for the $q\bar{q}$ combinatorial background in all final states for the data from sidebands are shown in Fig. 3.10. The PDF parameterizations of $\mathcal{H}_2$ are independent of the K^{*0}_J resonances, shown in Fig. 3.11.

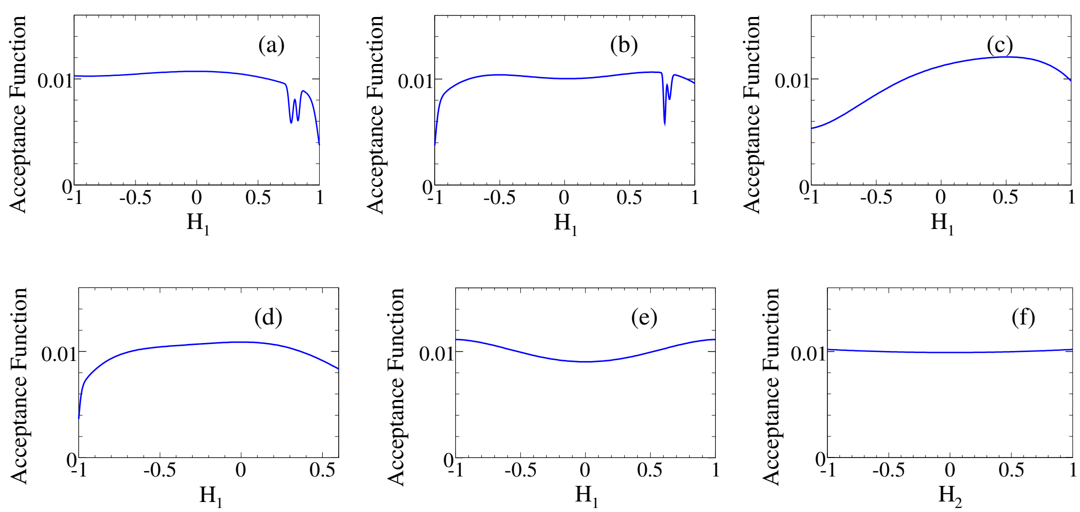

Figure 3.7: Angular acceptance functions for $\mathcal{H}_1$ in $\varphi K^+\pi^-$ ($1.13 < m_{K\pi} < 1.53$ GeV) (a), in $\varphi K^+\pi^-$ ($1.60 < m_{K\pi} < 2.10$ GeV) (b), in $\varphi K^0_S\pi^+$ (c), in $\varphi K^+_S\pi^0$ (d), in $\varphi K^+\pi^+\pi^-$ (e),and for $\mathcal{H}_2$ (f). These plots show only relative efficiency between different helicity points with arbitrary y-axis units. The $D^{\pm}_{(s)}$-meson veto causes the sharp acceptance dips near $\mathcal{H}_1 = 0.8$ seen in (a) and (b).

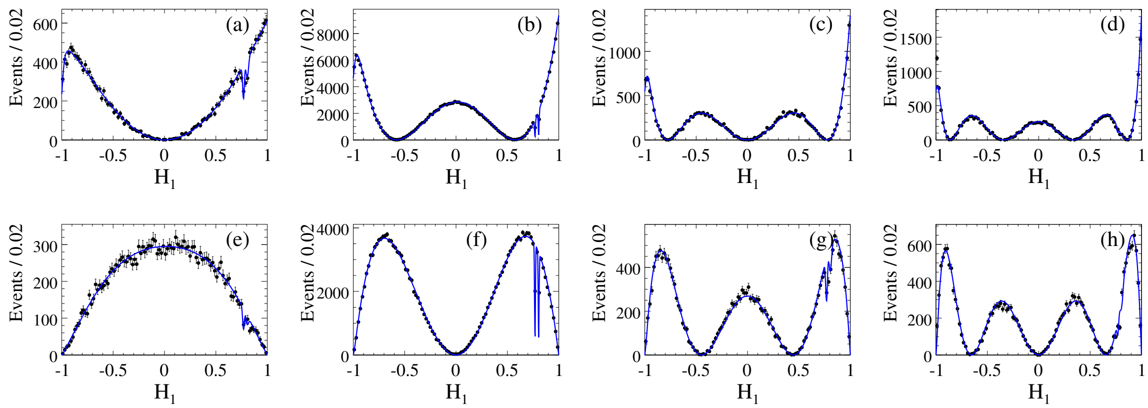

Figure 3.8: PDF parameterization of $\mathcal{H}_1$ for the longitudinal (top row) and transverse (bottom row) mode for decays $B^0 \to \varphi K_J^{*0}(K^+\pi^-)$, where the spin and parity of K_J^{*0} are $J^P = 1^-\, 2^+,\, 3^-\, 4^+$, for mesons $K^*(1680)^0$ (a,e), $K_2^*(1430)^0$ (b,f), $K_3^*(1780)^0$ (c,g), and $K_4^*(2045)^0$ (d,h) respectively. The dots with error bars represent the MC simulation data, while the solid lines show the angular distributions with acceptance effects applied.

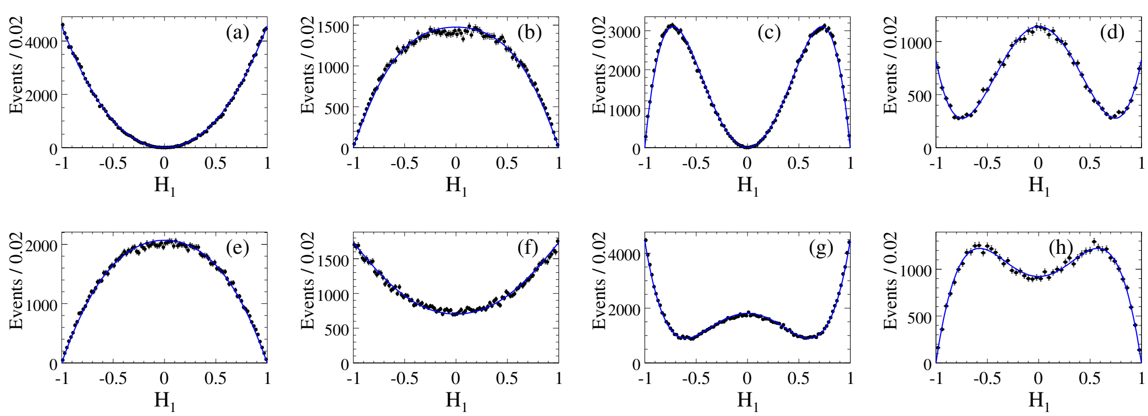

Figure 3.9: PDF parameterization of $\mathcal{H}_1$ for the longitudinal (top row) and transverse (bottom row) mode for decays $B^+ \to \varphi K_J^{*+}(K^+\pi^+\pi^-)$, where the spin and parity of K_J^{*+} are $J^P = 1^-\, 1^+,\, 2^+\, 2^-$, for mesons $K^*(1410)^0$, $K_1(1270)^+$, $K_2^*(1430)^+$ and $K_2(1820)^+$ respectively. The dots with error bars represent the MC simulation data, while the solid lines show the angular distributions with acceptance effects applied.

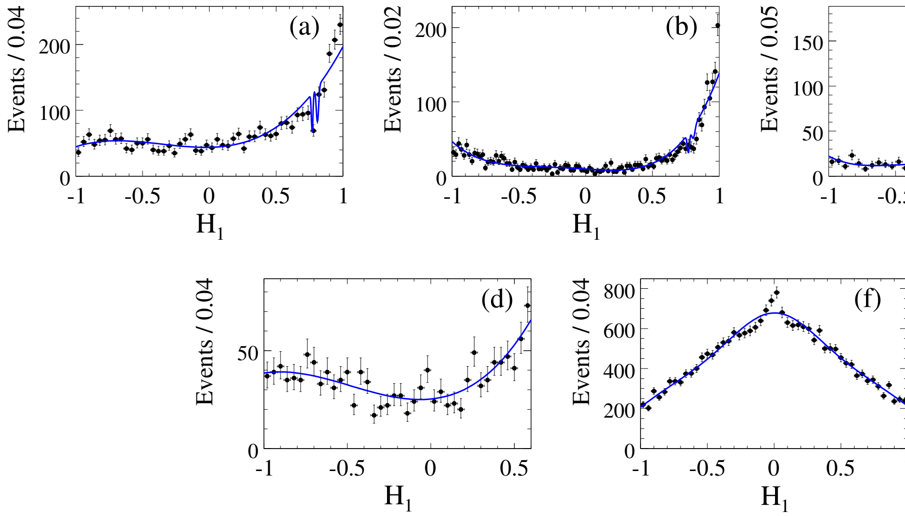

Figure 3.10: PDF parameterization of $\mathcal{H}_1$ for the $q\bar{q}$ combinatorial background in the lower (a) and higher (b) mass ranges in the final states $K^+K^-K^+\pi^-$, in the final states $K^+K^-K^0_S\pi^+$ (c), $K^+K^-K^+\pi^0$ (d) and $K^+K^-K^+\pi^+\pi^-$ (e). The dots with error bars represent the data from the sidebands, while the solid line for the fit results.

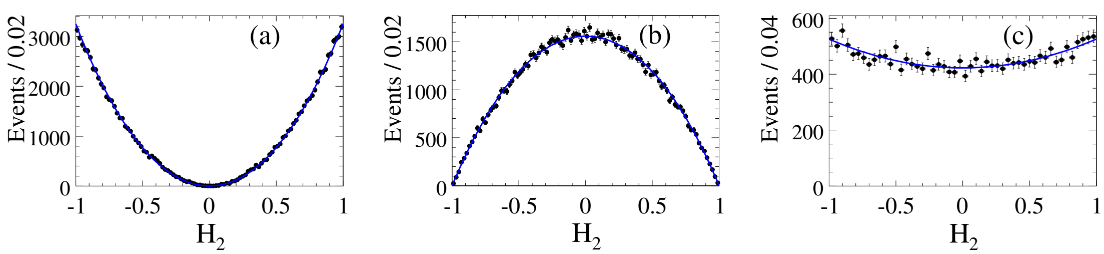

Figure 3.11: PDF parameterization of $\mathcal{H}_2$ for the longitudinal (a) and transverse (b) modes of decays $B^0 \to \varphi K_2^*(1430)^0$ in MC simulation, and the $q\bar{q}$ combinatorial background (c) in the final state $K^+K^-K^+\pi^-$ for the data from sidebands.

The interference between the $J = 2$ and the S-wave $(K\pi)$ contributions is modeled with the term $2\Re e(A_J A_0^*)$ in Eq. (3.31) with the four-dimensional angular and $m_{K\pi}$ dependence, as discussed in detail in Section 3.3. About 13800 φK_2^* and φK_0^* events are generated with $\delta_0 = 0, \pi/4, \pi/2$ and π, with PDFs shown in Fig. 3.12. It has been shown in the decays $B^0 \to J/\psi(K\pi)_0^{*0}$ and $B^\pm \to \pi^\pm(K\pi)_0^{*0}$ [74, 75] that the amplitude behavior as a function of $m_{K\pi}$ is consistent with that observed by LASS except for a constant phase shift. Integrating the probability distribution over $(\mathcal{H}_1, \mathcal{H}_2, \Phi)$, the interference term $2\Re e(A_J A_0^*)$ should vanish. However, the interference contribution becomes non-zero with the introduction of the detector acceptance effects on $(\mathcal{H}_1, \mathcal{H}_2)$. The total yield of the two modes is corrected before calculating the branching fractions. The effect can be estimated by comparing the integral of $B \to \varphi K_2^*(1430)$, $B \to \varphi(K\pi)_0^*$ and the interference probability contribution. The interference term contribution to the total yield is found to be 3.5% in the $B^0 \to \varphi K^+\pi^-$ mode, 3% in the $B^+ \to \varphi K_S^0\pi^+$ mode and 10% in the $B^+ \to \varphi K^+\pi^0$ mode. The yields of $\varphi(K\pi)_{0,2}$ are thus scaled by 96.5%, 97% and 90% in the $K^+\pi^-$, $K_S^0\pi^+$ and $K^+\pi^0$ final states, respectively, while calculating the branching fractions.

The parameterization of the nonresonant signal-like contribution $B \to f_0 K^* \to (K^+K^-)K^*$ is identical to the signal in the primary kinematic observables $m_{\rm ES}$, ΔE, and $\mathcal{F}$, but is different in the angular and $m_{K\overline{K}}$ distributions. For $B \to f_0 K^*$, the ideal angular distribution is uniform in Φ and $\mathcal{H}_2$ and is proportional to $\mathcal{H}_1^2$, due to angular momentum conservation. A coupled-channel B-W function is used to model the K^+K^- mass

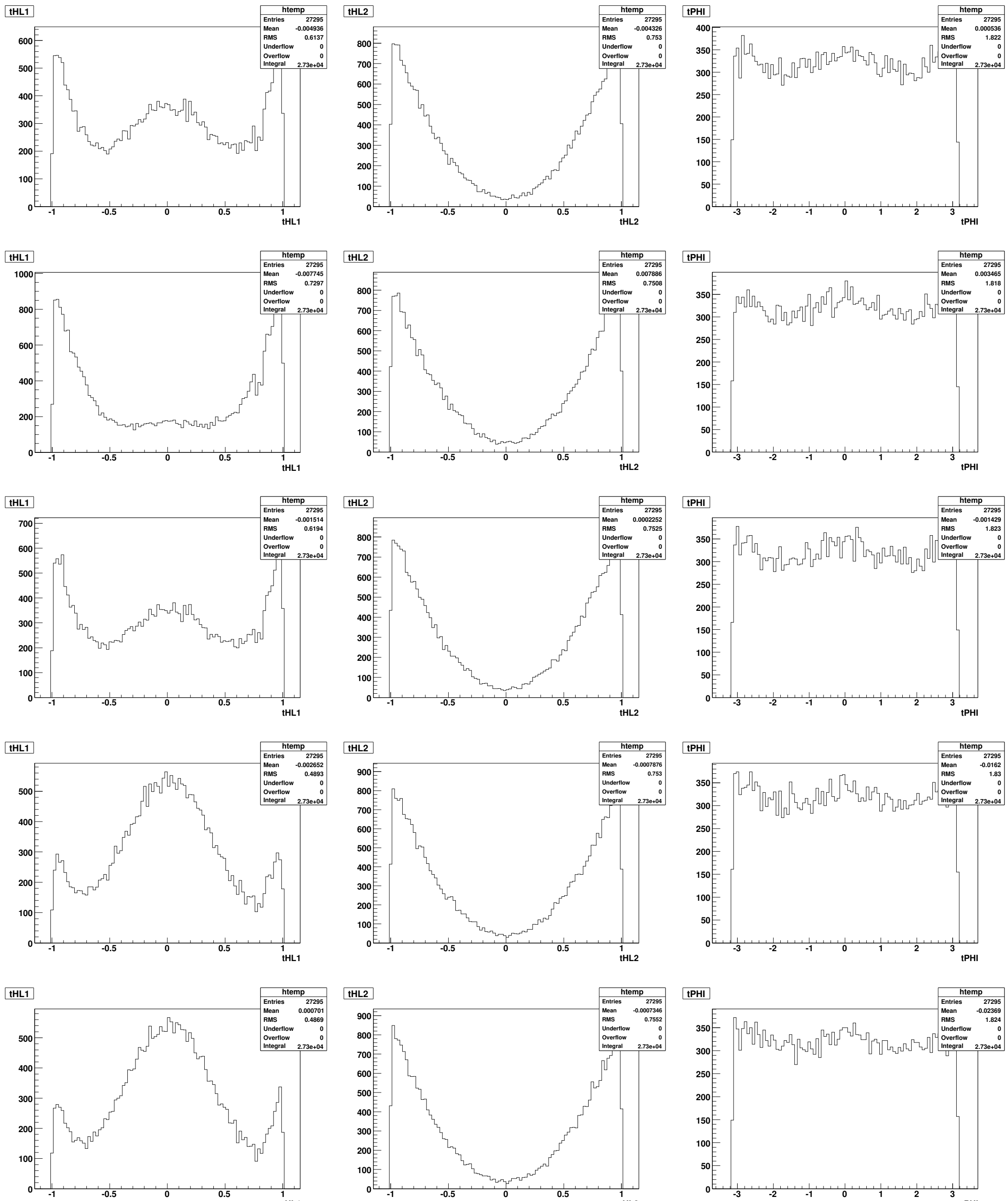

Figure 3.12: Interference effects on angular PDFs in higher-mass region. $\cos\theta_1$, $\cos\theta_2$ and ϕ distributions are shown from left to right for each δ_0. The first row shows the distributions without interference. Second, third, fourth and fifth rows show the distributions with $\delta_0 =$ 0, $\pi/4$, $\pi/2$ and π respectively.

distribution for the f_0 [72, 73]. The broad invariant mass distribution of f_0 compared to the narrow φ resonance was found to account well for any broad $m_{K\overline{K}}$ contribution. This PDF parameterization is further varied as part of the systematic uncertainty studies. The $m_{K\pi(\pi)}$ distribution in f_0K^* is parameterized as a $(K\pi)^{*0}_0$ in the lower mass range and $K^*(1680)^0$ in the higher mass range of B^0 decays, and as $K^*(892)^+$ and $K_1(1400)^+$ in the $K_S\pi^+/K^+\pi^0$ and $K^+\pi^+\pi^-$ final states.

3.6.3 Fit Validation

The analysis selection and fit performance are validated in a number of cross-check analyses. Fits on the data collected below the $\Upsilon(4S)$ resonance and on GEANT-based [71] MC simulation of about three times the statistics of the data sample for both $q\overline{q}$ production (continuum) and generic $\Upsilon(4S) \to B\overline{B}$ decays are performed to To test the treatment of combinatorial background in the PDF. The contribution of several dozen exclusive B meson decays which could potentially mimic the signal is also tested with statistics of more than an order of magnitude greater than their expectation. No significant bias in the background treatment was found. Systematic uncertainties associated with this treatment are discussed in the next chapter.

To test the signal PDF parameterization and the overall fit performance, a large number of MC experiments are generated. Each one represents a statistically independent modeling of the fit to the data. The signal events are taken from the generated MC samples, while background is generated from the PDF with the total sample size corresponding to the on-resonance data sample. Signal-like events are embedded according to expectation. The fit performance is studed based on the $(x^{\rm fitted} - x^{\rm generated})/\sigma(x)$ distributions (x pull distributions), where x denotes one of the signal parameters. The mean of the $(x^{\rm fitted} - x^{\rm generated})$ distribution is taken as the systematic error due to the fit bias, listed in Sec. 4.3 in the next chapter. In general, the results of the MC experiments are found to be in good agreement with the expectations and the error estimates to be correct.

Figs. 3.13 show the $(x^{\rm fitted} - x^{\rm generated})/\sigma(x)$ distributions for the parameters $\{n_{{\rm sig}J}$, $\mathcal{A}_{CPJ}$, f_{L2}, $f_{\perp 2}$, $\phi_{\parallel 2}$, $\delta_{02}\}$, in the lower mass range of decays $B^0 \to \varphi K^+\pi^-$. The means and widths of most of these distributions are within about 5% of the expected values of zero and one, which results in negligibly small uncertainty in the fit result. The large mean (about 0.2) in the polarization f_{L2} pull distribution is mainly because the generated value is so close to the physical boundary (1.0) that the $(x^{\rm fitted} - x^{\rm generated})$ distribution becomes asymmetrical rather than Gaussian. As shown in Table 4.6, the fit bias of f_{L2} dominates the systematic error. The large means (around ± 0.2) in the signal yields $n_{{\rm sig}J}$ pull distributions of $\varphi K_2^*(1430)^0$ and $(K\pi)_0^{*0}$ are due to the large correlation between the two modes. The mean of the pull distribution of the total yield remains within 5%.

Figs. 3.14 show the $(x^{\rm fitted} - x^{\rm generated})/\sigma(x)$ distributions for the parameters $n_{{\rm sig}J}$ in the higher mass range of decays $B^0 \to \varphi K^+\pi^-$. The signal events according to the upper limits on the measured yields are embedded to avoid the physical fit boundaries on the

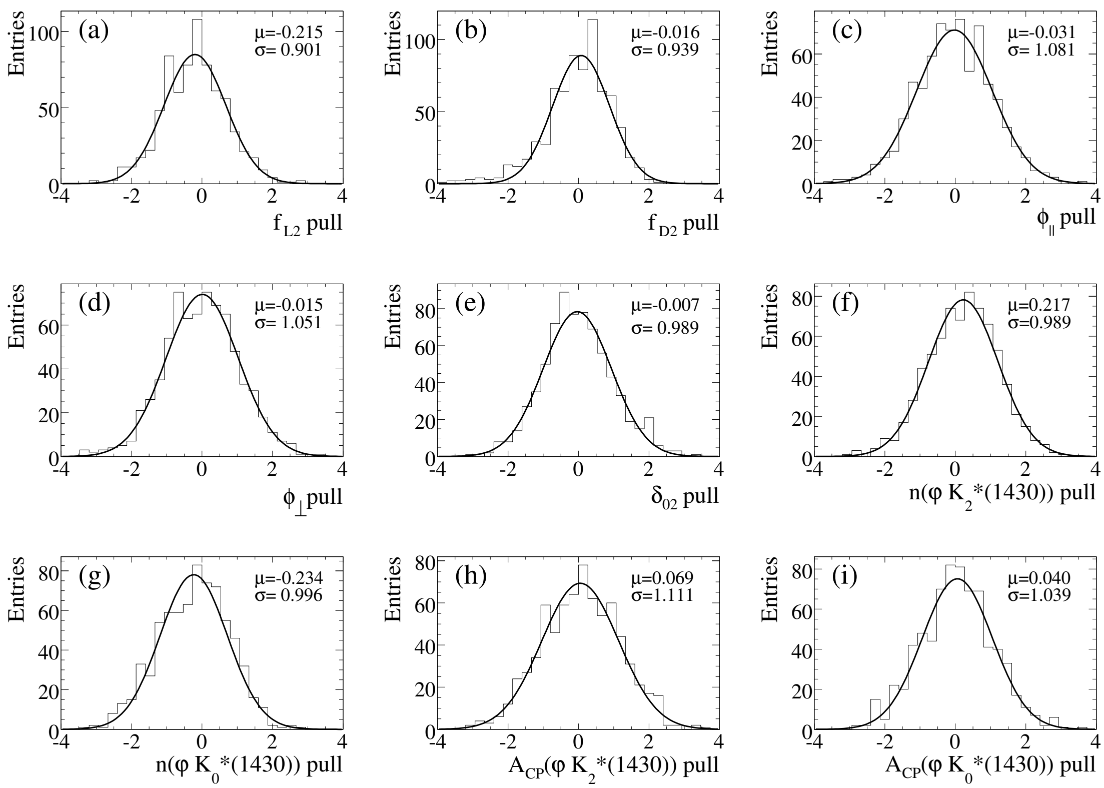

Figure 3.13: Distributions of $(x^{\text{fitted}} - x^{\text{generated}})/\sigma(x)$ for a large number of generated MC experiments for the lower mass range $B^0 \to \varphi K_J^{*0}(K^+\pi^-)$ ($1.13 < m_{K\pi} < 1.53$ GeV). A Gaussian fit is superimposed for each plot, and x denotes signal parameters: f_{L2} (a), $f_{\perp 2}$ (b), $\phi_{\parallel}$ (c), $\phi_{\perp}$ (d) and δ_{02} (e) for $\varphi K_2^*(1430)^+$, the yields of decays $\varphi K_2^*(1430)^0$ (f), $\varphi(K\pi)_0^{*0}$ (g), and the overal CP asymmetries of decays $\varphi K_2^*(1430)^0$ (h), $\varphi(K\pi)_0^{*0}$ (i).

yields. Large fit bias on the yields measurements are found due to the limited statistics. As shown in further tests the fit bias on all yields would decrease significantly if provided larger signal events. The CP-violation parameters are constrained to zero in these decay amplitudes. The interferences between the final states $B \to \phi(K\pi)_J$ with different J are also ignored because no significant signal is observed, see Table 4.2. The polarization parameters f_{LJ} with $J = 1, 3, 4$ for $B^0 \to \varphi K^*(1680$, $\varphi K_3^*(1780)$ and $\varphi K_4^*(2045)^0$ are allowed to float to account for any statistical fluctuations. However, due to the low significance (around 1.0σ), these polarization measurements are consistent with any physically allowed value. The interferences between different $(K\pi)$ resonances are ignored. Since the acceptance in the decay angles is nearly uniform, the event yields are almost completely unaffected by interference among states of different J.

Figs. 3.15 show the $(x^{\text{fitted}} - x^{\text{generated}})/\sigma(x)$ distributions for the yield parameters $n_{\text{sig}J}$ for $B^+ \to \varphi K_J^{(*+)}$ decays and polarization parameters f_{L2} and f_{L1} for the vector-tensor ($\varphi K_2^*(1430)^+$) and vector–axial-vector ($\varphi K_1(1270)^+$) decays. The CP-violation paramters in the decay amplitudes of $B^+ \to \varphi K^*(1410)^+$, $\varphi K_1(1400)^+$ and $\varphi K_2(1820)^+$ are constrained to zero, as no significant signal has been observed in any of these modes, see Table 4.3. scalar $(K\pi)_0^{*+}$ contributions is implemented in the same way as in the $B^0 \to \varphi(K\pi)^0_{0,2}$ decays. The interferences between the other decays are ignored, with the effects accounted for in the systematics, discussed in Sec. 4.3.

A “blind” technique is used at all analysis development steps. Numerical values of all

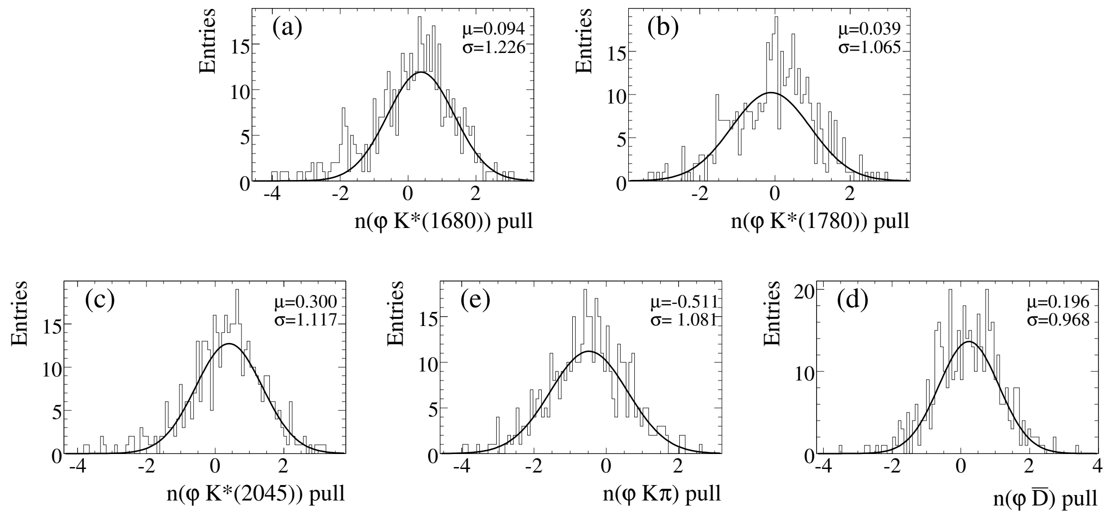

Figure 3.14: Distributions of $(x^{\text{fitted}} - x^{\text{generated}})/\sigma(x)$ for a large number of generated MC experiments for the higher mass range $B^0 \to \varphi K_J^{*0}(K^+\pi^-)$ $(1.60 < m_{K\pi} < 2.10$ GeV). A Gaussian fit is superimposed for each plot, and x denotes the yields parameters for decays $B^0 \to \varphi K^*(1680)^0$ (a), $\varphi K_3^*(1780)^0$ (b), $\varphi K_4^*(2045)^0$ (c), $\varphi K^+\pi^-$ (d) and $\varphi \overline{D}^0$ (e).

physics parameters $n_{\text{sig}J}$, $\mathcal{A}_{CPJ}$ and $\vec{\zeta}$ were kept hidden until the analysis method and tools were selected, validated and fixed. Consistency between the blind fit results and prediction from generated samples for the likelihood $\mathcal{L}$ and error values were used to judge the goodness of fit. The projection of data and likelihood fit PDFs onto individual variables with the enhancement of either signal or background to judge consistency are also examined. Detailed study of the systematic errors did not reveal any uncertainties which would exceed statistical errors.

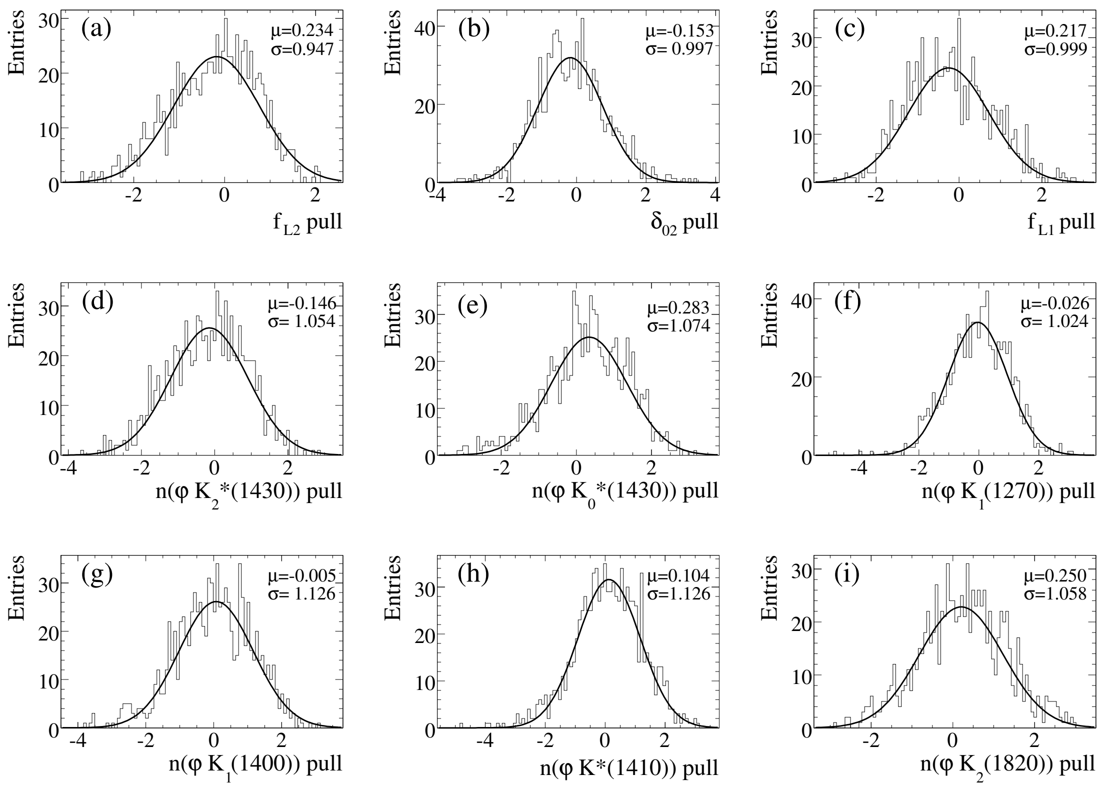

Figure 3.15: Distributions of $(x^{\text{fitted}} - x^{\text{generated}})/\sigma(x)$ of the yields measurements for a large number of generated MC experiments in decays $B^+ \to \varphi K_J^{*+}$. A Gaussian fit is superimposed in each plot, and x denotes signal parameters: f_{L2} (a) and δ_{02} (b) for $\varphi K_2^*(1430)^+$, f_{L1} (c) for $\varphi K_1(1270)^+$, the yields of decays $\varphi K_2^*(1430)^+$ (d), $\varphi(K\pi)_0^{*+}$ (e), $\varphi K_1(1270)^+$ (f), $\varphi K_1(1400)^+$ (g), $\varphi K^*(1410)^+$ (h), $\varphi K_2(1820)^+$ (i).

3.7 $B \to \bar{D}\pi$ Control Sample Study

In order to establish that the MC simulation reproduces the kinematic observables in the data, such as $m_{\rm ES}$, ΔE, and $\mathcal{F}$, high-statistics B^0-meson decays with similar kinematics and topology are studied, such as the $B^0 \to D^-\pi^+ \to (K^+\pi^-\pi^-)(\pi^+)$ decays.

There is good agreement between data and MC for $m_{\rm ES}$, ΔE and $\mathcal{F}$ with the validation shown in Table 3.6, and the projection plots shown in Fig. 3.16. The deviations in the means of the distributions of $m_{\rm ES}$ and ΔE vary according to the data taking conditions. The average deviations are 0.7 MeV for $m_{\rm ES}$, 4 MeV for ΔE, much smaller than the resolutions. These corrections into account in the study of the $B^0 \to \varphi K\pi(\pi)$ decays. The deviations in the $\mathcal{F}$ are negligible, with no additional corrections needed.

Table 3.6: Data–MC validation for m_{ES}, $\Delta E$and $\mathcal{F}$ width decays $B^0 \rightarrow D^-\pi^+$.

Observable	Data	MC	Data-MC Shift
m_{ES} (MeV)	5278.920 ± 0.022	5279.610 ± 0.009	-0.690
$\sigma_{m_{ES}}$ (MeV)	2.598 ± 0.018	2.483 ± 0.008	–
ΔE (MeV)	-4.717 ± 0.194	-0.785 ± 0.084	-3.932
$\sigma_{\Delta E}$ (MeV)	20.416 ± 0.178	18.565 ± 0.103	–
$\mathcal{F}$ Mean	-0.603 ± 0.004	-0.606 ± 0.001	+0.003
$\mathcal{F}$ R.M.S.	0.453 ± 0.003	0.457 ± 0.001	–
$\mathcal{F}$ Asym.	0.061 ± 0.013	0.093 ± 0.004	–

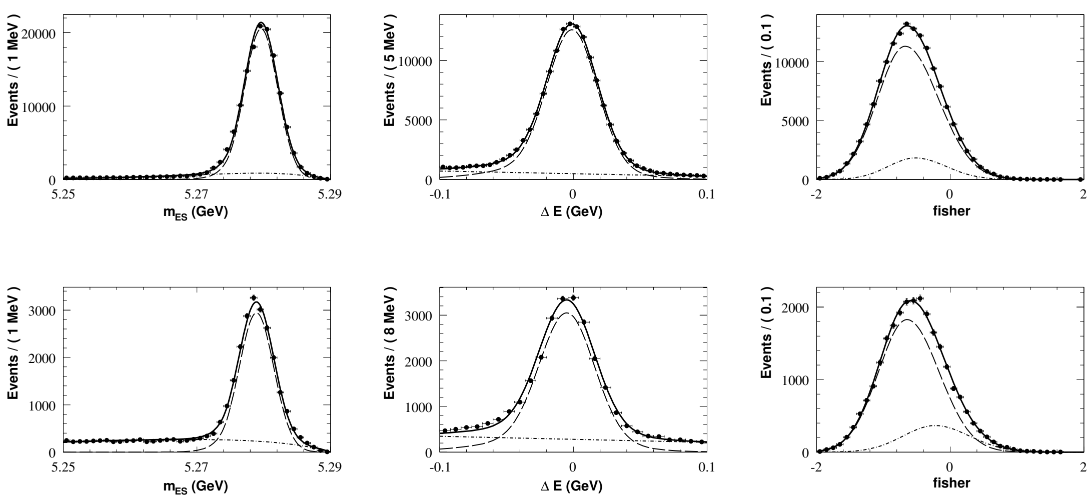

Figure 3.16: Projections onto the variables m_{ES}, ΔE and $\mathcal{F}$ are shown from left to right for MonteCarlo (first row) and the Run1-6 on peak data (second row). The solid lines represent fit results, while dots with error bars represent the data. Dashed lines in Data plots represent combinatorial background.

Chapter 4

Analysis Results

This chapters describes the results on the decays $B \to \varphi K_J^{(*)}$, published in Ref. [59,60, 62], including the fit results, signal significance, systematic uncertainties, signal efficiency and branching fractions.

The fit results are presented in three parts based on the three ML fit models on four sub-decays $K_J^{(*0)} \to K^+\pi^-$ and $K_J^{*+} \to K_S^0\pi^+$, $K^+\pi^0$ and $K^+\pi^+\pi^-$, see Sec. 3.6.1. The signal significance is defined as the square root of the change in $2\ln\mathcal{L}$ when the yield is constrained to zero in the likelihood $\mathcal{L}$. The systematic errors are discussed in Sec. 4.3. The total efficiency ε of a signal decay is defined as the product of reconstructed efficiency $\varepsilon_{\mathrm{reco}}$ obtained from the MC samples, and the daughter branching fractions of φ and $K_J^{(*)}$ [56]. The branching fraction of $B \to \varphi K_J^{(*)}$ is defined as $\mathcal{B} = n_{\mathrm{sig}}/(n_{B\overline{B}} \cdot \mathcal{E})$, where the n_{sig} is the number of signal events, $\mathcal{E}$ is the reconstructed efficiency, and $n_{B\overline{B}}$ is the number of

$B\overline{B}$ mesons produced.

4.1 Fit Results

4.1.1 Decays $B^0 \to \varphi K^+\pi^-$ in Lower $K\pi$ Mass Range

In the lower mass range ($1.13 < m_{K\pi} < 1.53$ GeV) of decays $B^0 \to \varphi K^+\pi^-$, non-zero yields with more than $10\,\sigma$ significance (including systematic uncertainties) in both $\varphi K_2^*(1430)^0$ and $\varphi(K\pi)_0^{*0}$ modes are observed.

Projections onto the discriminating variables are shown in Fig. 4.1. For illustration, the signal fraction is enhanced with a requirement on the signal-to-background probability ratio to be greater than a value within the range (0.85 – 0.95), calculated with the plotted variable excluded. This requirement is at least 50% efficient for the signal events. In Tables 4.1 the $n_{\mathrm{sig}J}$, $\mathcal{A}_{CPJ}$, and $\vec{\zeta} \equiv \{f_{L2}$, $f_{\perp 2}$, $\phi_{\parallel 2}$, δ_{02}, $\mathcal{A}^0_{CP2}$, $\Delta\phi_{\parallel 2}$, and $\Delta\delta_{02}\}$ parameters of the $\varphi K_2^*(1430)^0$, and $\varphi(K\pi)_0^{*0}$ decays are shown.

The longitudinal polarization f_L of the vector–tensor decay $B^0 \to \varphi K_2^*(1430)^0$ is measured as $0.901^{+0.046}_{-0.058} \pm 0.037$, consistent with the naive expectation of the longitudinal polarization dominance [17, 29–34]. However its difference from the value observed in the vector-vector decay $0.494 \pm 0.034 \pm 0.013$ [63] brings additional puzzle. It points to a unique role for the spin-1 particle recoiling against the φ in the $B \to \varphi K^*$ polarization puzzle. Projections onto $\mathcal{H}_1$ and $\mathcal{H}_2$ in Fig. 4.1 (e,f) confirm predominant longitudinal po-

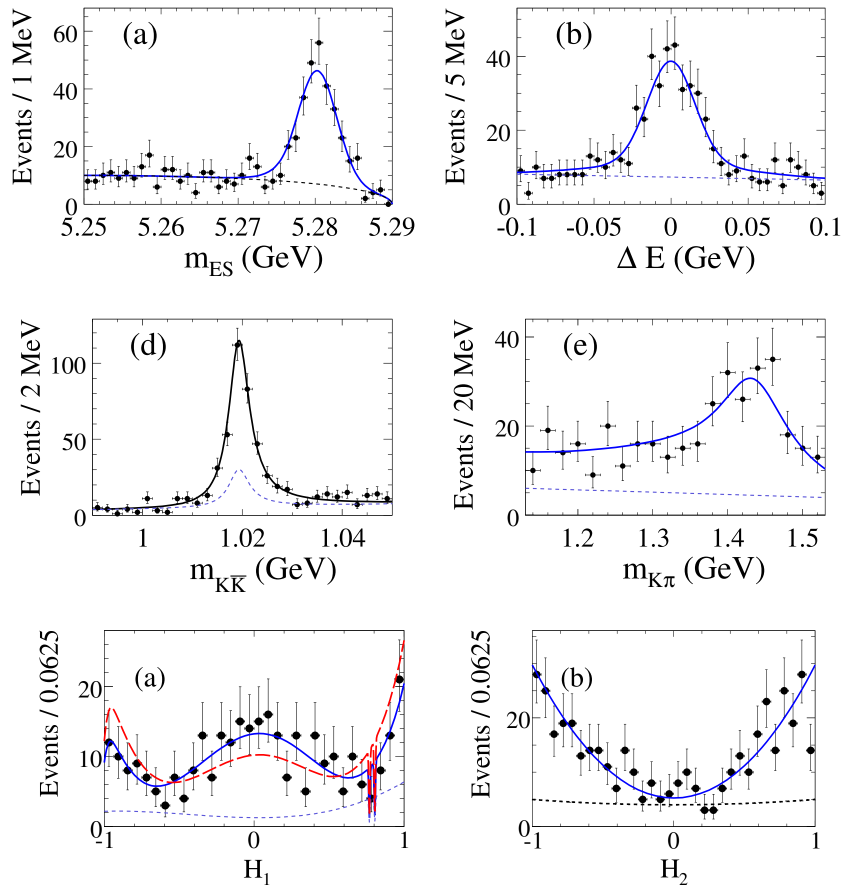

Figure 4.1: Projections onto the variables $m_{\rm ES}$(a), ΔE(b), $m_{K\pi}$ (c), $m_{K\overline{K}}$ (d), $\mathcal{H}_1$ (e) and $\mathcal{H}_2$ (f) for the signal $B^0 \to \varphi K_2^*(1430)^0$ and $\varphi(K\pi)_0^{*0}$ candidates combined. The $D_{(s)^\pm}$-meson veto causes the sharp acceptance dips near $\mathcal{H}_1 = 0.8$ in (a), and the long-dashed line represents the PDF projection without the interference term included. Data distributions are shown with a requirement on the signal-to-background probability ratio calculated with the plotted variable excluded. The solid (dashed) lines show the signal-plus-background (background) PDF projections in the left,

Table 4.1: Fit results on $B^0 \to \varphi K^+\pi^-$ in the lower mass range, see Table 1.5 for definition of the parameters. The dominant fit correlation coefficients (ρ) are presented for the $\varphi K_2^*(1430)^0$ mode where correlations of δ_0 with $\phi_\parallel$ and of $\Delta\delta_0$ with $\Delta\phi_\parallel$ are shown. The systematic errors are quoted last.

parameter	$\varphi(K\pi)_0^{*0}$	$\varphi K_2^*(1430)^0$	ρ
	$J=0$	$J=2$	
$n_{\mathrm{sig}J}$ (events)	$158 \pm 22 \pm 13$	$158 \pm 20 \pm 7$	
$\mathcal{S}(\sigma)$	> 10	> 10	
f_{LJ}		$0.901^{+0.046}_{-0.058} \pm 0.037$	$\}-15\%$
$f_{\perp J}$		$0.002^{+0.018}_{-0.002} \pm 0.031$	
$\phi_{\parallel J}$ (rad)		$3.96 \pm 0.38 \pm 0.06$	–
δ_{0J} (rad)		$3.41 \pm 0.13 \pm 0.13$	19%
$\mathcal{A}_{CPJ}$	$+0.20 \pm 0.14 \pm 0.06$	$-0.08 \pm 0.12 \pm 0.05$	
$\mathcal{A}^0_{CPJ}$		$-0.05 \pm 0.06 \pm 0.01$	–
$\Delta\phi_{\parallel J}$ (rad)		$-1.00 \pm 0.38 \pm 0.09$	–
$\Delta\delta_{0J}$ (rad)		$+0.11 \pm 0.13 \pm 0.06$	16%

larization with sizable $(3\mathcal{H}_1^2-1)^2\mathcal{H}_2^2$ and $\mathcal{H}_2^2$ contributions for the vector-tensor $\varphi K_2^*(1430)$ and vector-scalar $\varphi(K\pi)_0^*$ decays. Fig. 4.1 (e) illustrates the effect of tensor-scalar $K\pi$ interference, which could either enhance events in the middle of the $\mathcal{H}_1$ distribution and deplete them at the edges, or the other way around. Fig. 4.1 (e) indeed shows significant improvement in the $\mathcal{H}_1$ parameterization with the inclusion of interference, corresponding to the observed $\delta_{02} \simeq \pi$.

The three quantities $\phi_{\perp 2}$, $\mathcal{A}_{CP2}^{\perp}$ and $\Delta\phi_{\perp 2}$, which characterize parity-odd transverse amplitudes in the vector-tensor decay are not measured because $f_{\perp 2}$ is found to be consistent with zero. Due to the low significance of the measurements of $f_{\parallel 2} = (1 - f_{L2} - f_{\perp 2})$ (1.9 σ) and $f_{\perp 2}$ (0 σ) in the $B^0 \to \varphi K_2^*(1430)^0$ decay, there is no sufficient information to constrain $\phi_{\parallel 2}$ at higher significance or to measure $\phi_{\perp 2}$, $A_{CP2}^{\perp}$, or $\Delta\phi_{\perp 2}$, which are thus constrained to zero in the fit. The yield of nonresonant decay $B^0 \to f_0(K\pi)^{*0}$ is found to be consistent with zero, resulting in negligible interference with the signal modes $B \to \varphi K_J^*$.

4.1.2 Decays $B^0 \to \varphi K^+\pi^-$ in Higher $K\pi$ Mass Range

In the higher mass range $(1.60 < m_{K\pi} < 2.15$ GeV) of decays $B^0 \to \varphi(K^+\pi^-)$ no significant signal is found in any of these four modes $\varphi K^*(1680)^0$, $\varphi K_3^*(1780)^0$, $\varphi K_4^*(2045)^0$ or $\varphi\overline{D}^0$. However, the significance of the $B^0 \to \varphi(K^+\pi^-)$ decay with $(K\pi)_0^{*0}$, $K^*(1680)^0$, $K_3^*(1780)^0$ and $K_4^*(2045)^0$ combined is larger than 5σ.

In Table 4.2, the $n_{\mathrm{sig}J}$ and signal significance are shown for $B^0 \to \varphi(K^+\pi^-)$ decays.

The likelihood distributions in the physically allowed ranges are integrated to compute the upper limits on the branching fractions, shown in Table 4.14. Projections onto the discriminating variables are shown in Fig. 4.2, where data distributions are shown with a requirement on the signal-to-background probability ratio calculated with the plotted variable excluded. In each plot this requirement is independently optimized to enhance the $\varphi K^+\pi^-$ signals, and results in an efficiency factor of (60–90)%.

Table 4.2: Fit results on $B^0 \to \varphi K^+\pi^-$ in the higher mass range. Yields $n_{\mathrm{sig}J}$ (events) and significance are shown. The systematic errors are quoted last.

parameter	$\varphi(K\pi)^{*0}_0$	$\varphi\overline{D}^0$	$\varphi K^*(1680)^0$	$\varphi K^*_3(1780)^0$	$\varphi K^*_4(2045)^0$
	$J=0$	$J=0$	$J=1$	$J=3$	$J=4$
$n_{\mathrm{sig}J}$	$47\pm16\pm15$	$16\pm7\pm3$	$8^{+10}_{-7}\pm11$	$-6\pm10\pm7$	$18^{+14}_{-12}\pm12$
$\mathcal{S}(\sigma)$	2.2	2.2	0.6	0.0	1.2

The nonresonant $\varphi(K\pi)^{*0}_0$ contribution is measured to be $47\pm16\pm15$ events, consistent with extrapolation (33 events) from the lower mass range. As the flavor asymmetries are constrained to zero, the branching fraction limit on $B \to \varphi D$ refer to the sum of two flavor final states, $\varphi\overline{D}^0$ and φD^0. The limit on the $B^0 \to \varphi\overline{D}^0$ decay provides a test of the B decay mechanisms involving φ mesons in the final state. It is later used as a confirmation in Ref. [80] for the small $\omega-\varphi$ mixing and the insignificant enhancement from rescattering processes like $B^0 \to \rho^+D^- \to \varphi\overline{D}^0$ or $B^0 \to K^{*+}D^-_s \to \varphi\overline{D}^0$.

Due to large correlation among various signal yields of the decay modes with broad $K\pi$

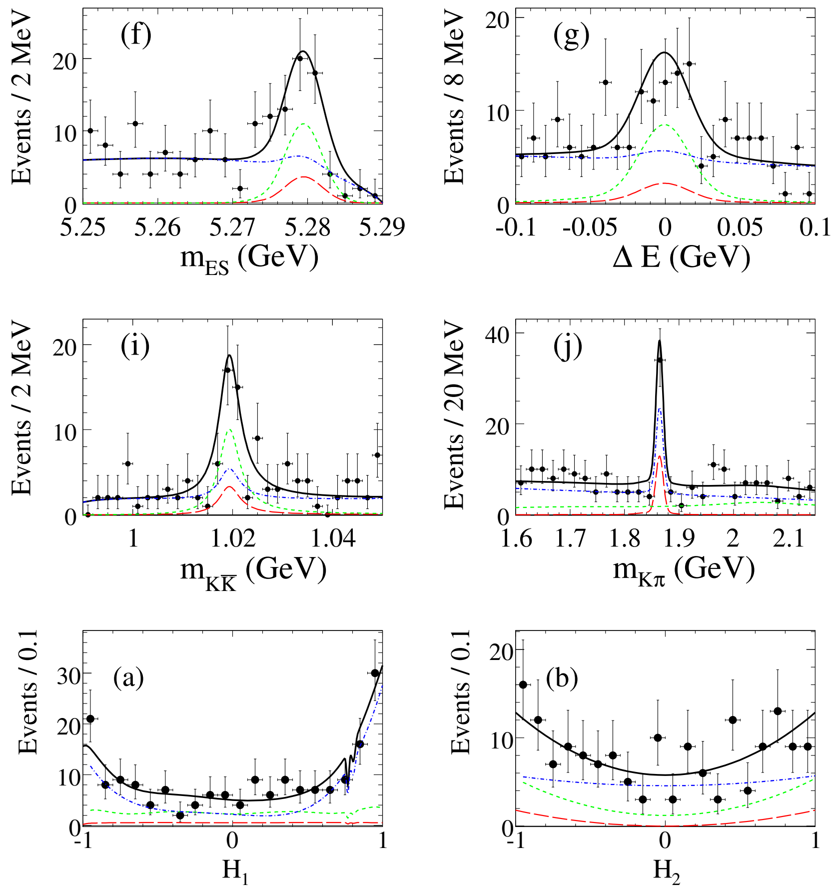

Figure 4.2: Projections onto the variables $m_{\rm ES}$(a), ΔE(b), $m_{K\pi}$ (c), $m_{K\overline{K}}$ (d), $\mathcal{H}_1$ (e) and $\mathcal{H}_2$ (f) for the $B^0 \to \varphi(K\pi)$ signal candidates combined in the higher mass range (right). The pronounced $\overline{D}^0$ mass peak in (d) is predominantly due to background. Data distributions are shown with a requirement on the signal-to-background probability ratio calculated with the plotted variable excluded. The solid (dotted-dashed) line shows the signal-plus-background (background only) PDF projection, while the dashed (long-dashed) line shows PDF projection for the sum of four $B^0 \to \varphi(K\pi)$ categories (for $B^0 \to \varphi\overline{D}^0$).

distributions, the errors on individual decay modes are relatively large. Thus in the fit, both event yields and polarization fractions f_{LJ} are constrained to the physically allowed ranges, $n_{\rm sig} > 0$ and $0 < f_{LJ} < 1$. The negative event yield in the $B^0 \to \varphi K_3^*(1780)^0$ decay is obtained by using the likelihood in the positive event region and fitting its shape with a parabolic function whose minimum is in the negative event region. The $B^0 \to f_0(980)K^{*0}$ yield is found to be consistent with zero for any of the K^{*0} spin assumptions, thus its interference with the signal modes is ignored.

For the three $B^0 \to \varphi K_J^{*0}$ decay modes with $J \geq 1$, the f_{LJ} fit results are consistent with any allowed value between 0 and 1. Therefore, the central values on f_{LJ} measurements are not reported. In the branching fraction upper limits calculations for these modes, To be conservative, the polarization which gives the smallest reconstruction efficiency is used in the branching fraction upper limits calculations for these modes.

4.1.3 Decays $B^+ \to \varphi K\pi(\pi)$

In the $B^+ \to \varphi K_J^{(*)+}$ decays, nonzero signals $\varphi K_1(1270)^+$ and $\varphi K_2^*(1430)^+$ are observed with significances (excluding systematic uncertainties in parentheses) of 5.0(5.3)σ and 5.5(6.0)σ, respectively. The combined $\varphi K_1(1270)^+$ and $\varphi K_1(1400)^+$ significance is 5.7(6.4)σ. This procedure is tested with the generated MC samples and account for a small observed deviation from the one-dimensional χ^2 statistical treatment, see Sec. 4.2.

In Tables 4.3 and 4.4 $n_{{\rm sig}J}$ and signal significance $\mathcal{S}(\sigma)$ of all $B^+ \to \varphi K_J^{(*+)}$ decays,

Table 4.3: Fit results on $B^+ \to \varphi K\pi\pi$: the number of signal events $n_{\mathrm{sig}J}$; significance $\mathcal{S}$; fraction of longitudinal polarization f_L; and the flavor asymmetry $\mathcal{A}_{CP}$. The $\varphi K_2(1770)^+$ yield is not considered in the nominal fit and the value indicated with † is obtained with these $\varphi K_2(1820)^+$ yield constrained to zero. The systematic errors are quoted last.

Mode	$n_{\mathrm{sig}J}$	$\mathcal{S}$ (σ)	f_L	$\mathcal{A}_{CP}$
$\varphi K_1(1270)^+$	$116 \pm 26\ ^{+15}_{-14}$	5.0	$0.46^{+0.12\ +0.06}_{-0.13\ -0.07}$	$+0.15 \pm 0.19 \pm 0.05$
$\varphi K_1(1400)^+$	$7 \pm 39 \pm 18$	0.2		
$\varphi K_2^*(1430)^+$	$130 \pm 27 \pm 14$	5.5	$0.80^{+0.09}_{-0.10} \pm 0.03$	$-0.23 \pm 0.19 \pm 0.06$
$\to K_S^0\pi^+$	$27 \pm 6 \pm 3$			
$\to K^\pm\pi^0$	$39 \pm 8 \pm 4$			
$\to K^+\pi^+\pi^-$	$64 \pm 14 \pm 7$			
$\varphi(K\pi)_0^{*+}$	$128 \pm 21 \pm 12$	8.2		$+0.04 \pm 0.15 \pm 0.04$
$\to K_S^0\pi^+$	$48 \pm 8 \pm 4$			
$\to K^+\pi^0$	$80 \pm 13 \pm 8$			
$\varphi K^*(1410)^+$	$64 \pm 31^{+20}_{-31}$	< 2		
$\varphi K_2(1770)^+$	$(90 \pm 32\ ^{+39}_{-46})^\dagger$	< 2		
$\varphi K_2(1820)^+$	$122 \pm 40^{+26}_{-83}$	< 2		

Table 4.4: Interference parameters δ_0 and $\Delta\delta_0$ for $\varphi K_2^*(1430)^+$ and $\varphi(K\pi)_0^{*+}$.

	δ_0	$\Delta\delta_0$
Results	$3.59 \pm 0.19 \pm 0.12$	$-0.05 \pm 0.19 \pm 0.06$

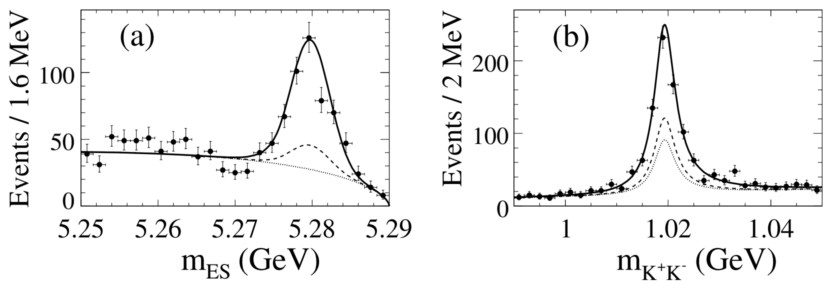

Figure 4.3: Projections onto the variables $m_{\rm ES}$ (a), and $m_{K\overline{K}}$ (b) for the signal $B^+ \to \varphi(K\pi)$ and $B^+ \to \varphi(K\pi\pi)$ candidates. Data distributions are shown with a requirement on the signal-to-background probability ratio calculated with the plotted variable excluded. The solid (dotted) lines show the signal-plus-background (combinatorial background) PDF projections, while the dashed lines show the full PDF projections excluding the signal.

flavor asymmetries $\mathcal{A}_{CPJ}$ and $\vec{\zeta} \equiv \{f_{L2}, f_{L1}, \delta_{02}, \Delta\delta_{02}\}$ of decays $\varphi K_2^*(1430)^+$, $\varphi(K\pi)_0^{*+}$ and $\varphi K_1(1270)^+$ are shown. The combined results are obtained from the simultaneous fit to the three decay subchannels $B \to \varphi K_S^0\pi^+$, $\varphi K^+\pi^0$ and $\varphi K^+\pi^+\pi^-$, see Sec. 3.6.1. When several subchannels contribute, the signal yield is quoted for each subchannel. The signal is illustrated in the projection plots in Figs. 4.3 and 4.4, where in the latter either the $\varphi K_1(1270)^+$ signal (left) or the $\varphi K_2^*(1430)^+$ signal (right) is enhanced.

The polarization of a vector–axial-vector decay $B^+ \to \varphi K_1(1270)^+$ is measured for the first time as $0.46^{+0.12}_{-0.13}\,^{+0.06}_{-0.07}$, resulting in a large fraction of transverse amplitude just as the vector-vector decay $B \to \varphi K^*(892)$ [59, 61, 63]. It indicate substantial A_{1+1} or A_{1-1} amplitude from an uncertain source, such as penguin annihilation [17, 29–34] and non-perturbative QCD rescattering [36–39] in the SM, or scalar and right-handed currents from multi-Higgs models beyond the SM [20–28] (see Sec. 1.3).

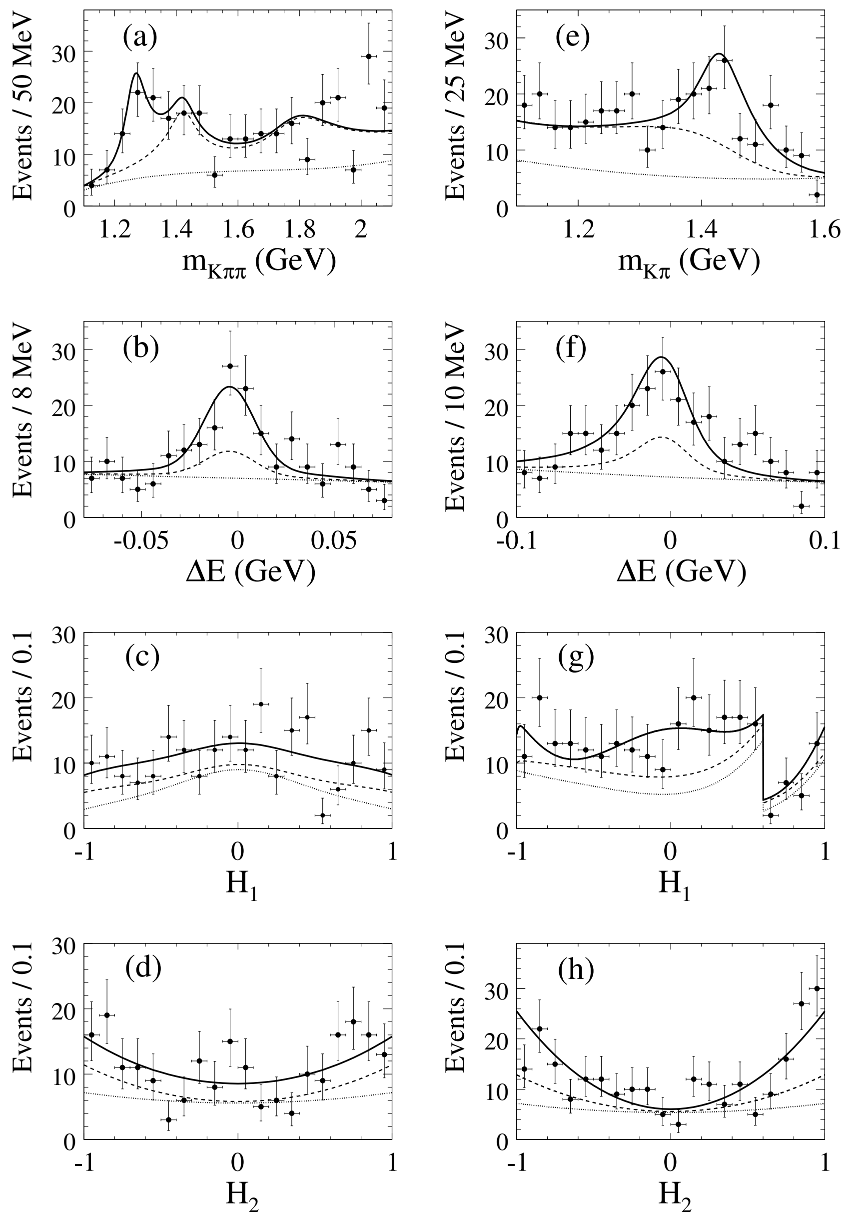

Figure 4.4: Left column: projections onto the variables $m_{K\pi\pi}$ (a), ΔE (b), $\mathcal{H}_1$ (c), and $\mathcal{H}_2$ (d) for the signal $\varphi K_1(1270)^{\pm}$ candidate. Right column: projections onto the variables $m_{K\pi}$ (e), ΔE (f), $\mathcal{H}_1$ (g), and $\mathcal{H}_2$ (h) for the signal $\varphi K_2^*(1430)^{\pm}$ and $\varphi(K\pi)_0^{*\pm}$ candidates combined. The step in (g) is due to selection requirement $\mathcal{H}_1 < 0.6$ in the channel with π^0. Data distributions are shown with a requirement on the signal-to-background probability ratio calculated with the plotted variable excluded. The solid (dotted) lines show the signal-plus-background (combinatorial background) PDF projections, while the dashed lines show the full PDF projections excluding $\varphi K_1^{\pm}$ (left) or $\varphi K_2^*(1430)^{\pm}$ (right).

Similar to the other final states, the yield of decay $B^0 \to f_0 K_1$, the nonresonant K^+K^- contribution under the φ is found to be consistent with zero. The nonresonant category $\varphi K\pi\pi$ yield is 148 ± 54 with statistical errors only.

4.2 Signal Significance

Signal significance is defined as the square root of the change in $2\ \ln\mathcal{L}$ when the yield is constrained to zero in the likelihood $\mathcal{L}$, corresponding to one-dimensional χ^2 statistical treatment. However, if the signal PDF has additional parameters other than the yield, such as polarization f_{LJ}, the significance can be overestimated by this treatment. This is critical for the decays with significance lower than 10σ, such as $B^+ \to \varphi K_1(1270)^+$ and $\varphi K_2^*(1430)^+$, where a nuisance parameter f_L is present. In that case, as the yield is constrained to zero, it may correspond to more than one degrees of freedom change to the original fit. However, as the yield and f_L are correlated, the significance would be underestimated in the two-dimensional χ^2 statistical treatment. The true value can be estimated with the generated MC samples, to be discussed below.

The probabilities of observing a signal yield with significance larger than $n\ \sigma$ calculated in both one-dimensional and two-dimensional χ^2 statistical treatment are shown in Table 4.5. On the other hand, it can also be determined experimentally by repeating the significance measurement on a large number of independent datasets without the signal decay embedded. As shown in Table 4.5, 10 million independent significance measurements are required to test the significance up to 5σ. With the complicate joint fit, it may take as long as several years. For this consideration the significance of decay $B^+ \to \varphi K_1(1270)^+$ is only tested up to 4σ, by performing 62000 significance measurements on 62000 independently generated MC samples without the signal $\varphi K_1(1270)$. The results are listed in Table 4.5. It is found that the observed probability corresponds to a significance in the middle of the one and two dimensional χ^2 treatment. The procedure is fully tested in the decays $B \to \varphi K^*(892)(K_S^0\pi^0)$, shown in Table 4.5.

The statistical significance of decay $B^+ \to \phi K_1(1270)^+$ is 5.5σ or 5.1σ with one-dimensional or two-dimensional χ^2 statistical treatment, and chosen as 5.3σ as the best estimation. Similarly, the significance for the combined signal of $B \to \varphi K_1(1270)$ and $\varphi K_1(1400)$ modes is found to be 6.6σ or 6.3σ with one-dimensional or two-dimensional χ^2 statistical treatment so 6.4σ is chosen as the best estimation. For decay $B^+ \to \phi K_2^*(1430)^+$ the statistical significance is 6.2σ or 5.8σ with one-dimensional or two-dimensional χ^2 statistical treatment so 6.0σ is chosen as the best estimation.

In the end, the statistical and systematic errors are convoluted to obtain the total significance. The systematic errors due to the interference does not affect the significance of $B^+ \to \varphi K_1(1270)^+$ or $\varphi K_2^*(1430)^+$. This is because in the null hypothesis (with the signal yield constrained to 0), the interference term vanishes leaving the $\mathcal{L}$ unchanged, while in the nominal fit $\mathcal{L}$ can only get larger with interference added. However, the systematic error due the interference is taken into account in the significance evaluation of the combined signal $B \to \varphi K_1$.

Table 4.5: Probability of observing a signal yield with significance larger than $n\ \sigma$. Statistical expectation based on one-dimensional (one-dim) and two-dimensional χ^2 treatment, and the tests are based on MC studies on decays $B^+ \to \varphi K_1(1270)^+(K^+\pi^+\pi^-)$ ($\varphi K_1(1270)$) and $B^0 \to \varphi K^*(892)^0(K_S^0\pi^0)$ [63] are shown.

n	1-D	2-D	$\varphi K_1(1270)^+$	$\varphi K^*(892)^0$
0	50%	50%	57.7%	41.8%
1	15.9%	30.3%	24.5%	17.7%
2	2.27%	6.76%	5.10%	17.7%
3	0.13%	0.56%	0.39%	0.23%
3.2	0.07%	0.30%	0.21%	–
3.4	0.034%	0.15%	0.12%	–
3.6	0.016%	0.077%	0.063%	–
3.8	0.007%	0.037%	0.023%	–
4.0	0.003%	0.017%	0.010%	0.006%
5.0	2.9×10^{-5}%	0.002%	0	7×10^{-5}%

4.3 Systematic Uncertainties Estimation

The dominant sources of systematic errors in the signal parameters for decays $B^0 \to \varphi K_J^{*0}$ and $B^+ \to \varphi K_J^{(*)+}$ are summarized in Tables 4.6-4.8

Table 4.6: Systematic errors in the signal yields φK_J^* (%) and other signal parameters (absolute values) for $B^0 \to \varphi(K^+\pi^-)$. Uncertainties due to PDF parameterization, acceptance (acc.) function modeling, B-background (B-bkgd), fit response, $m_{K\overline{K}}$ PDF for the $f_0(980)(K^+K^-)$, charge asymmetry in reconstruction, assumptions about the unconstrained CP asymmetries $\mathcal{A}_{CP2}^{\perp}$ and $\Delta\phi_{\perp 2}$ (CP asym.), and the total errors are quoted.

	PDF	$m_{K\overline{K}}(f_0)$	acc.	B-bkgd	fit	charge	CP-asym.	total
$\varphi(K\pi)_0^*$	7.1	–	–	3.4	2.7	–	–	8.3
$\varphi K_2^*(1430)$	3.3	–	–	0.8	2.8	–	–	4.4
$\varphi K^*(1680)$	22.7	100.0	–	1.1	110.7	–	–	150.7
$\varphi K_3^*(1780)$	45.6	100.0	–	14.5	32.3	–	–	116.1
$\varphi K_4^*(2045)$	9.0	60.1	–	1.1	27.0	–	–	66.3
$\varphi(K\pi)\dagger$	6.0	20.9	–	0.6	22.8	–	–	31.4
$\varphi\overline{D}$	5.8	19.4	–	6.5	7.1	–	–	21.3
$\mathcal{A}_{CP0}$	0.036	–	0.002	0.048	0.001	0.020	0.008	0.064
f_{L2}	0.006	–	0.001	0.016	0.033	–	0.004	0.037
$f_{\perp 2}$	0.001	–	0.001	0.004	0.031	–	0.003	0.031
$\phi_{\parallel 2}$	0.051	–	0.002	0.021	0.029	–	0.012	0.063
$\mathcal{A}_{CP2}$	0.037	–	0.002	0.029	0.001	0.020	0.005	0.051
$\mathcal{A}_{CP2}^0$	0.012	–	0.001	0.005	0.002	–	0.003	0.014
$\Delta\phi_{\parallel 2}$	0.027	–	0.002	0.088	0.012	–	0.011	0.093
δ_{02}	0.117	–	0.004	0.062	0.009	–	0.006	0.133
$\Delta\delta_{02}$	0.012	–	0.004	0.057	0.009	–	0.007	0.059

Table 4.7: Systematic errors in the signal yields (events) for decays $B^+ \to \varphi K_J^{(*+)}$. Uncertainties due to the PDF parameterization of $m_{K\pi\pi}$ PDF for $K_2^*(1430)$ and nonresonant $B^+ \to \varphi K^+\pi^+\pi^-$, $m_{K\overline{K}}$ PDF for $f_0(980)$, B-background (B-bkgd), fixed B-background (fixed B-bkgd), fit response, assumptions about the constrained angular and yield parameters f_{LJ}, r_{02} for decays $\varphi K^*(1410)$ and φK_2, reconstructed efficiencies ($\mathcal{E}$), interference between the $\varphi K_2^*(1430)^+$ and $(K\pi)_0^{*+}$ ($K^*(1430)$ interf), and between the $\varphi K_1(1270)^+$ and $K_1(1400)^+$ (K_1 interf) and the total errors are quoted.

$B^+ \to \varphi$	K_2^*	$(K\pi)_0^*$	K_1	K_1'	$K_1\dagger$	K^*	$K_2(1770)$	$K_2(1820)$
PDF	4.1	2.8	8.7	7.5	$^{+8.8}_{-6.1}$	8.4	12.6	15.6
$m_{K\pi\pi}(K_2^*)$	0.5	0.3	$^{+2.0}_{-0.0}$	1.1	$^{+3.1}_{-0.0}$	2.0	1.0	0.9
$m_{K\pi\pi}$(nonres)	2.8	0.9	$^{+6.0}_{-0.0}$	9.5	$^{+15.5}_{-0.0}$	17.3	7.0	15.8
$m_{K\overline{K}}(f_0)$	0.2	2.3	0.4	$^{+5.0}_{-0.0}$	$^{+4.7}_{-0.0}$	0.5	1.0	0.1
B-bkgd	1.5	0.9	0.2	0.4	0.2	1.5	1.5	0.1
Fixed B-bkgd	0.2	1.8	0.0	0.1	0.1	0.1	1.0	0.0
fit	4.8	7.1	0.6	1.9	1.3	5.1	5.3	12.3
$f_L(\varphi K^*(1410))$	$^{+9.1}_{-1.3}$	1.8	$^{+1.5}_{-0.0}$	$^{+5.8}_{-2.4}$	$^{+5.9}_{-0.9}$	$^{+0.0}_{-20.1}$	$^{+0.0}_{-13.3}$	$^{+5.3}_{-15.3}$
$f_L(\varphi K_2)$	0.4	0.1	$^{+0.0}_{-1.3}$	$^{+0.0}_{-3.6}$	$^{+0.0}_{-4.9}$	$^{+0.0}_{-5.4}$	$^{+4.7}_{-20.9}$	$^{+0.0}_{-26.2}$
$r_{02}(\varphi K_2)$	0.7	0.5	$^{+0.0}_{-2.8}$	$^{+0.0}_{-4.8}$	$^{+0.0}_{-7.6}$	$^{+0.6}_{-17.6}$	$^{+0.0}_{-36.4}$	$^{+0.0}_{-66.1}$
$K_2(1770)$	0.7	0.5	$^{+0.0}_{-2.1}$	$^{+0.0}_{-8.7}$	$^{+0.0}_{-6.3}$	$^{+0.0}_{-9.0}$	$^{+35.6}_{-0.0}$	$^{+0.0}_{-35.6}$
$\mathcal{E}$	8.2	5.0	1.0	3.0	2.0	2.5	1.0	0.1
$K^*(1430)$ interf	3.3	5.0	–	–	–	–	–	
K_1 interf	–	–	10.3	11.0	7.6	–	–	–
Total	$^{+14.6}_{-11.5}$	11.4	$^{+15.0}_{-14.0}$	$^{+18.5}_{-17.6}$	$^{+21.2}_{-17.3}$	$^{+20.2}_{-30.5}$	$^{+39.1}_{-46.2}$	$^{+25.6}_{-83.4}$

Table 4.8: Systematic errors in angular and CP-asymmetries parameters (absolute values) for decays $B^+ \to \varphi K_J^{*+}$. Uncertainties due to PDF parameterization, $m_{K\pi\pi}$ PDF for $K_2^*(1430)$ and nonresonant $K^+\pi^+\pi^-$, $m_{K\overline{K}}$ PDF for $f_0(980)$, acceptance (acc.) function modeling, B-background (B-bkgd), fixed B-background (fixed B-bkgd), fit response, charge asymmetry in reconstruction, assumptions about the constrained angular and yield parameters f_{LJ}, r_{02} for decays $\varphi K^*(1410)$ and φK_2, and the total errors are quoted.

	$\varphi K_2^*(1430)^+$		$\varphi(K\pi)_0^{*+}$	Interference		φK_1^+	
	f_{L2}	$\mathcal{A}_{CP2}$	$\mathcal{A}_{CP0}$	δ_{02}	$\Delta\delta_{02}$	f_{L1}	$\mathcal{A}_{CP1}$
PDF	0.008	0.025	0.015	0.040	0.015	0.022	0.042
$m_{K\pi\pi}(K_2^*)$	0.005	0.011	0.003	0.001	0.001	0.008	0.005
$m_{K\pi\pi}$(nonres)	0.004	0.004	0.001	0.002	0.001	0.054	0.001
$m_{K\overline{K}}(f_0)$	0.007	0.002	0.004	0.023	0.007	0.004	0.001
acceptance	0.002	0.001	0.002	0.032	0.035	0.010	0.002
B-bkgd	0.012	0.006	0.025	0.069	0.014	0.003	0.001
Fixed B-bkgd	0.003	0.001	0.002	0.008	0.001	0.000	0.000
fit	0.020	0.013	0.009	0.060	0.017	$^{+0.001}_{-0.037}$	0.014
charge	–	0.020	0.020	–	–	–	0.020
$f_L(\varphi K^*(1410))$	0.011	0.013	0.003	0.004	0.005	0.008	0.005
$f_L(\varphi K_2)$	0.003	0.002	0.001	0.001	0.035	$^{+0.000}_{-0.020}$	0.007
$r_{02}(\varphi K_2)$	0.005	0.005	0.002	0.001	0.001	$^{+0.000}_{-0.041}$	0.005
$K_2(1770)$	0.004	0.005	0.000	0.000	0.003	$^{+0.000}_{-0.032}$	0.002
$\mathcal{E}$	0.006	0.024	0.002	0.010	0.009	0.004	0.003
Total	0.030	0.048	0.038	0.108	0.060	$^{+0.061}_{-0.072}$	0.050

4.3.1 PDF Uncertainties

Certain assumptions are made about the signal and background distributions in the fit. Most background parameters are allowed to vary in the fit, but most B-decay parameters to the expectations are constrained based on MC and control samples. In order to account for the resulting uncertainties, these parameters are allowed to vary within their errors to account for the correlations among the parameters. Uncertainties on $m_{\rm ES}$, ΔE, and $\mathcal{F}$ are obtained from the control samples discussed in Sec. 3.7. The invariant mass uncertainties incorporate errors on the resonance parameters as quoted in Table 1.4 and Ref. [56]. The resolution in the $K\pi$ and K^+K^- invariant masses are also accounted for with the corresponding errors on the absolute values of 1 MeV and 0.3 MeV, respectively. For most of the $K\pi(\pi)$ resonances the errors from the PDG [56] dominate.

In $B^+ \to \varphi K_J^{*+}(K^+\pi^-\pi^-)$ decays additional systematics to the $m_{K\pi\pi}$ PDF parameterizations is assigned due to the sequential subchannels of decays $K_J^* \to K\pi\pi$. The systematic errors $m_{K\pi\pi}(K_2^*)$ and $m_{K\pi\pi}$(nonres) systematics come from the uncertainties in the $m_{K\pi\pi}$ PDF of the signal $B^+ \to \varphi K_2^*(1430)^+$ and nonresonant decay $\varphi K^+\pi^+\pi^-$. The nominal fit includes only the subchannel $K^{*0}\pi^+ \to K^+\pi^+\pi^-$, which is then replaced by subchannel $K^+\rho^0 \to K^+\pi^+\pi^-$ as cross-checks. The alternative $m_{K\pi\pi}$ PDF for $K_2^*(1430)^+$ and three-body kinematics phase term $\varphi K^+\rho^0$ are validated with the generated MC sample. The substitution induced changes to the nominal results taken as systematic errors.

In all channels the $f_0(K\pi)$ or $f_0(K\pi\pi)$ mode represents for both the nonresonant

$K\overline{K}K_J^*$ mode and the $f_0K_J^*$ resonance. The exact composition is not clear. Thus, as cross-checks, the empirical Flatte distribution [72, 73] of $m_{K\overline{K}}$ PDF is replaced by both flat line and pure $B \to K^+K^-K_J^*$ Dalitz term, with the largest deviation from the nominal results quoted as the systematics due to "$m_{K\overline{K}}$ (f_0)" in This effect is found negligible in other final states except in the higher mass range of $B^0 \to \varphi K_J^{*0}(K^+\pi^-)$.

There is a special class of PDF uncertainties for the helicity angles, due to the acceptance function. In addition to statistical errors in the MC sample, the momentum-dependent uncertainty of the tracking efficiency is also considered. The main effect is on the curvature of the acceptance function shown in Fig. 3.7 due to a strong correlation between the momentum of a track and the value of the helicity angle. Moreover, in order to study the effects of charge asymmetry in angular distributions, the acceptance correction is applied independently to only B or only $\overline{B}$ decay subsamples. The largest deviation is taken the systematic error due to acceptance in Tables 4.6 and 4.8.

4.3.2 Uncertainties Due to B-background

To estimate the effect of the B-background which could mimic signal, a full GEANT4-based [71] MC simulation of the $\Upsilon(4S) \to B\overline{B}$ events are studied. The events which may have ΔE and $m_{\rm ES}$ distributions similar to signal are embedded into the data sample and fitted. The observed variations to the nominal fit results are taken as systematic errors "B-bkgd" in Tables 4.6-4.8. The nonresonant contribution is taken into account naturally in the fit with both $K\overline{K}$ and $K\pi(\pi)$ contributions allowed to vary. The $K\overline{K}K_J^{(*)}$ contribution is modeled as $f_0(K\pi)_0^{*0}$ or $f_0K^*(1680)^0$ in the lower or higher mass ranges of B^0-decays, and $f_0K_1(1400)^+$ in the B^+-decays.

In the nominal fit the number of $B^0 \to \varphi K^*(892)^0$ events constrained to the the value extrapolated from measured branching fraction [59]. As cross-checks this number is varied corresponding to $\pm 1\sigma$ change to the $\varphi K^*(892)$ branching fractions. The resulting variations to the nominal fit results are found negligible for decays $B^0 \to \varphi K_J^{*0}(K^+\pi^-)$, and quoted as systematic errors "Fixed B-bkgd" for decays $B^+ \to \varphi K_J^{*+}(K_S^0\pi^+/K^+\pi^0)$ in Tables 4.7 and 4.8.

4.3.3 Potential Fit Bias

The selected signal $B \to \varphi K_J^{(*)}$ events contain a small fraction of incorrectly reconstructed candidates. Misreconstruction occurs when at least one candidate track belongs to the decay products of the other B from the $\Upsilon(4S)$ decay, which happens in about 5% of the cases in the $B^0 \to \varphi K^+\pi-$ decay. The distributions that show peaks for correctly reconstructed events have substantial tails, with large uncertainties in MC simulation, when misreconstructed events are included. These tails and incorrect angular dependence would reduce the power of the distributions to discriminate between the background and the collection of correctly and incorrectly reconstructed events. Therefore, in the analyses described here, the signal PDF is chosen to represent only the correctly reconstructed candidates, while the reconstruction efficiency accounts for both the correctly reconstructed and misreconstructed MC events.

Fitting the generated samples to determine the number of correctly reconstructed candidates has an efficiency close to 100% in spite of a few percent of selected candidates are identified as background. This is accounted with a systematic error taken as half the fraction of candidates identified as background. Similarly, systematic errors on other parameters are taken as the largest deviation from the expectation. This includes a potential bias from the finite resolution in the helicity angle measurement and a possible dilution due to the misreconstructed component. These uncertainties are quoted as the the systematic error "fit"in Tables 4.6-4.8.

4.3.4 Charge Bias

The charge bias uncertainty affects only the relative yields of B and $\overline{B}$ events. A systematic error of 2% is assigned account for a possible asymmetry in the reconstruction of a charged kaon from a K^{*0} [13], quoted as "charge" in Tables 4.6 and 4.8. Overall charge asymmetry has a negligible effect on the angular asymmetry parameters, while the angular dependence of the charge asymmetry is tested with the flavor-dependent acceptance function discussed in the above.

4.3.5 Constrained Signal Parameters

Due to the limited statistics, some signal parameters are not measured properly. The fit results could have statistical errors large enough to accommodate the whole fit range (such as the polarizations for extremely low statistics modes), or by including those parameters the fit becomes very unstable (such as CP asymmetries). Thus, in the nominal fit values of these parameters are constrained to the SM favored values, while the sensitivity of the fit results to these parameters is studied in extensive cross-checks. Additional systematic errors are assigned if non-negligible variations to the nominal results are seen in those cross-checks, to be described in the following.

The two CP parameters $\mathcal{A}_{CP2}^{\perp}$ and $\Delta\phi_{\perp 2}$ are not measured in decay $B^0 \to \varphi K_2^*(1430)^0$. They are constrained to be zero in nominal fit, and varied in the cross-checks within ± 0.2 for the direct-CP asymmetry and ± 0.5 rad for the phase asymmetry. This introduces a small effect to the angular parameters in decays $B^0 \to \varphi K^*(892)^0$ and $\varphi K_2^*(1430)^0$, quoted as the uncertainties due to "CP-asym." in Table 4.6.

For the low statistics decays $B^+ \to \varphi K^*(1410)^+$ and φK_2^+, the longitudinal polarizations are constrained to 0.8 in the nominal fit and varied between 0.5 and 0.93 in cross-checks. The largest variations to the results are quoted as the systematic errors "$f_L(\varphi K^*)$" and "$f_L(\varphi K_2)$" in Tables 4.7 and 4.8. Asymmetric behavior of the yields of decays $B \to \varphi K_1(1400)$, $B \to \varphi K^*(1410)$ and $B \to \varphi K_2(1770)$ are observed usually in the negative side. This affects the polarization f_L of $B \to \varphi K_1$ in the negative side as well.

The kinematic parameter r_{02} in Ref. [66]) describing $K_2^+ \to K\pi\pi$ decays is not predicted well. It is thus varied to a set of values corresponding to various partial waves of the quasi-two-body K_2 decay channels as cross-checks. The dominant decay is $K_2(1770) \to K_2^*(1430)\pi$ from the PDG [56]. There is no branching fraction measurement or predication for $K_2(1820)$ decay, it is assumed that $K_2(1820)$ decays to $K_2^*(1430)\pi$. In the $K_2 \to K_2^*(1430)\pi$ decays the total orbital angular momentum of the system takes the value of 0, 2 or 4, considering parity conservation. Large statistics MC samples are generated from these three partial wave states, from which r_{02} is found as 0.329 ± 0.006, 1.908 ± 0.074 and 0.132 ± 0.007 for $L = 0, 2, 4$, respectively. The alternative subchannel $K_2 \to K^*(892)\pi$ is also tested, and r_{02} is found as 0.110 ± 0.002 and 0.178 ± 0.006, corresponding to with $L = 1, 3$. In the nominal fit the r_{02} is constrained to 0.333, as the value obtained from expected dominant S-wave state. It is then replaced by $\{0,\ 0.1,\ 0.15,\ 1.0,\ 2.0\}$ in cross-checks. The largest variations to the nominal results are quoted as the systematic error "$r_{02}(\varphi K_2)$" in Tables 4.7 and 4.8.

As discussed in Sec. 3.6.3, the fit model can not separate the contributions from $K_2(1770)$ from $K_2(1820)$ in $B^+ \to \varphi K_2^+$ decays. The exact decay mechanism of the $K_2(1770)$ and $K_2(1820)$ is not clear. No significant signal is observed for the two $B^+ \to \varphi K_2^+$ decays, see Table 4.3, either. So to avoid any model dependence and double counting, only the upper limits on the branching fractions of decays $B \to \varphi K_2(1820)$ or $B \to \varphi K_2(1770)$ are quoted, assuming no $B \to \varphi K_2(1770)$ or $B \to \varphi K_2(1820)$ contribution. In the nominal fit only the $K_2(1820)$ contribution is included, as the decay width of $K_2(1820)$ is broad enough to cover the $K_2(1770)$ resonance. Systematic errors to the yields of $B \to \varphi K_2(1820)$ or $\varphi K_2(1770)$ mode are assigned by replacing the $K_2(1820)$ or $K_2(1770)$ with $K_2(1770)$ or $K_2(1820)$. This action doesn't affect the other modes.

4.3.6 Uncertainties Due to Interference

This section describes the systematic errors due to the interference between decays $B \to \phi K_2^*(1430)$ and $(K\pi)_0^*$, and between the $B^+ \to \varphi K_1(1270)^+$ and $\varphi K_1(1400)^+$.

The interference between $B \to \varphi K_2^*(1430)$ and $(K\pi)_0^*$ is described by a composite PDF based on $\{m_{K\pi}, \mathcal{H}_1, \mathcal{H}_2, \Phi\}$, shown in Eq. (3.31) of Sec. 3.3. Given ideal angular distributions, the integrated interference term $2\Re e(A_0(m_{K\pi}, \theta_1, \theta_2, \Phi)A_2^*(m_{K\pi}, \theta_1, \theta_2, \Phi))$ over full angular ranges should vanish. However, as the detector acceptance effects $\mathcal{G}(\mathcal{H}_1, \mathcal{H}_2, \Phi)$ (see Fig. 3.7) is introduced, the interference contribution becomes non-zero. The total yield of the two modes needs to corrected before calculating the branching fractions, by comparing the integral of the differential decay widths of $B \to \varphi K_2^*(1430)$ and $\varphi(K\pi)_0^*$ and the interference probability contribution, as discussed in Sec. 3.6.2.

The interference contribution depends on the signal parameters f_{L2}, the fraction μ of the $\varphi K_2^*(1430)$ yield in the total yield, and δ_{0J}. It is found that the interference contribution to the total yield f_{inter} is 3.5% in the $B^0 \to \varphi K^+\pi^-$ mode, 3% in the $B^+ \to \varphi K_S^0\pi^+$ mode and 10% in the $B^+ \to \varphi K^+\pi^0$ mode. The uncertainty of this contribution is propagated

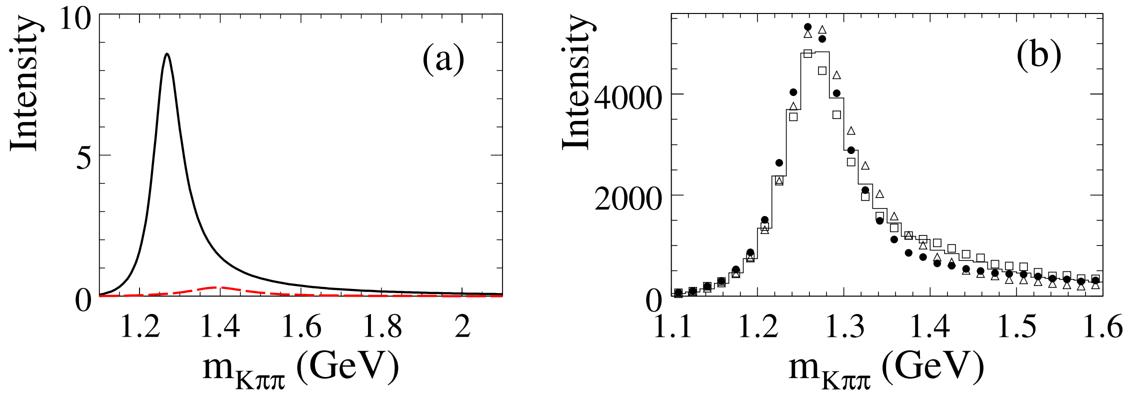

Figure 4.5: Intensity $|M_J(m_{K\pi\pi})|^2$ of the invariant amplitudes for $K_1(1270)$ (solid) and $K_1(1400)$ $K\pi\pi$ separately (a) and the combined K_1 (Right) contributions. In plot (b), the histogram represents the intensity without the interference contribution, while the open triangles (△), filled cirles (•) and open squares (□)represent the intensities with interference δ as 0, 1/2π and π respectively. The relative intensity of the amplitudes is taken from the results in Table 4.3, while the absolute intensity is shown in arbitrary units.

from the errors of the depending signal parameters. In the joint fit to the $B^+ \to \varphi K_J^{*+}$ data these corrections are put back to the ML fit to obtain the final results. To test the sensitivity of the fit results to these correction, each of them is allowed to vary by $\pm 1\sigma$ from the central value. The largest variations to the nominal results are quoted as as the systematics "$K^*(1430)$ interf." in Tables 4.7.

The interference between $B \to \varphi K_1(1270)$ and $\varphi K_1(1400)$ is ignored in the fit model to start with. Since the observed yield of $B \to \varphi K_1(1400)$ is found consistent with 0 (see Table 4.3), the interference effects are thus accounted for as systematic errors rather than in the nominal fit. Fig. 4.5 shows the two K_1 resonances $m_{K\pi\pi}$ distributions with the relative size scaled by the results in Table 4.3.

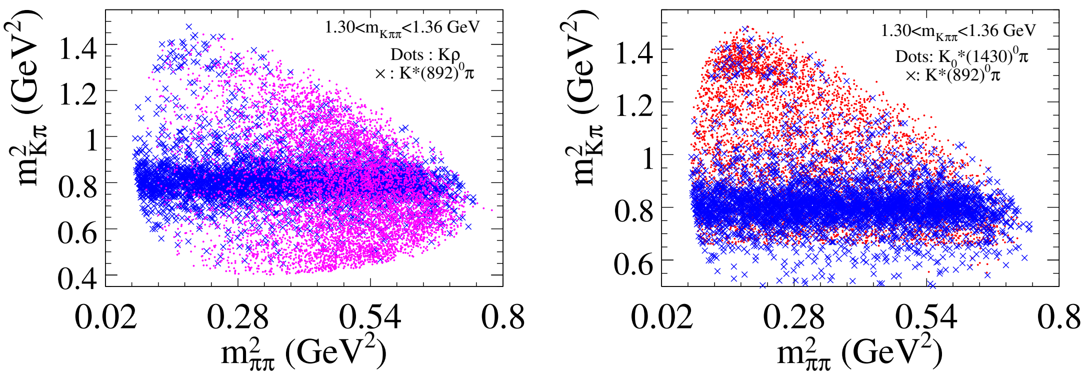

Figure 4.6: Left: $m^2_{K\pi} - m^2_{K\pi\pi}$ Dalitz plot for the three body decays $K\pi\pi$, in the $K\pi\pi$ invariant mass range (1.33 - 1.36) GeV. The left plot shows the contributions from decays $K^*\pi$ (cross) and $K\rho$ (dot), while the right plot shows the contribution from $K^*(892)\pi$ (cross) and $K_0^*(1430)\pi$ (dot) decays.

Similar to the interference treatment in φK_2^* and $(K\pi)_0^*$, a composite PDF can be built from $\varphi K_1(1270)$ and $\varphi K_1(1400)$ modes as

$$\mathtt{PDF}(K_1) = f \cdot |A_1|^2 + (1-f) \cdot |A_2|^2 + \sqrt{f(1-f)} \cdot \alpha \cdot 2\mathtt{Re}(A_1 \cdot \mathtt{e}^{\mathrm{i}\delta} A_2^*), \qquad (4.1)$$

where f is the fraction of $B \to \varphi K_1(1270)$ yield in the total yield of $B \to \varphi K_1$; A_1 or A_2 is the normalized $m_{K\pi\pi}$ PDF of $K_1(1270)$ or $K_1(1400)$; α (0 - 1) denotes the degree of overlap of the $K_1 \to K\pi\pi$ subchannels.

While $K_1(1270)$ decays through three channels ($K^*(892)\pi$, $K_0(1430)^*\pi$ and $K\rho$), $K_1(1400)$ decays to $K^*(892)\pi$ dominantly. In the Dalitz plot $m^2_{K\pi} - m^2_{\pi\pi}$, the $K^*(892)\pi$ channel of the two K_1 resonances overlap completely. The overlap between the other two subchannels of $K_1(1270)$ ($K_0(1430)^*\pi$ and $K\rho$ of $K_1(1270)$) and the $K^*(892)\pi$ subchannel of $K_1(1400)$ can be illustrated with the Dalitz plots shown in Fig. 4.6. The phase of α

is absorbed in the overall phase δ, while the amplitude of α can be estimated by

$$\alpha = |f_1 \cdot \alpha_1 + f_2 \cdot \alpha_2 \cdot \mathtt{e}^{\mathtt{i}\delta_2} + f_3 \cdot \alpha_3 \mathtt{e}^{\mathtt{i}\delta_3}| \tag{4.2}$$

where f_1, f_2 and f_3 describe the branching fractions of each decay subchannel $K^*\pi$, $K_0^*\pi$ and $K\rho$ of $K_1(1270)$, respectively. The α_1, α_2 and α_3 are complex numbers, the amplitudes of which describe the degree of overlap between these three subchannels ($K^*(892)^0\pi^+$, $K_0^*(1430)^0\pi^+$ and $K^+\rho^0$) of $B \to \varphi K_1(1270)$ and the $K^*(892)^0\pi^+$ of $B \to \varphi K_1(1400)$.

The α_i can be estimated by integrating out the mass dependence of the differential decay width at $m_{K\pi\pi} = 1.34$ GeV, which corresponds to the middle of the interference zone of the two K_1

$$\begin{aligned}
\alpha_1 &= 1 && (4.3)\\
\alpha_2 &= \int dm^2_{K\pi} \int dm^2_{\pi\pi} B_1(m_{K\pi})(K_0^*) \cdot B_2(m_{K\pi})^*(K^*) = 0.26 + 0.40\mathtt{i} && (4.4)\\
\alpha_3 &= \int dm^2_{K\pi} \int dm^2_{\pi\pi} B_1(m_{\pi\pi})(\rho) \cdot B_2(m_{K\pi})^*(K^*) = 0.23 - 0.11\mathtt{i}. && (4.5)
\end{aligned}$$

In the above formulae, $B_1(m_{K\pi})(K_0^*)$ and $B_1(m_{\pi\pi})(\rho)$ are Dalitz plot normalized amplitudes of resonances $(K\pi)_0^{*0}$ and ρ^0 from $K_1(1270)$; B_2 is the B-W amplitude of resonance $K^*(892)^0$ from $K_1(1400) \to K^*(892)\pi$.

The phase factors δ_2 and δ_3 in α_2 and α_3 calculations are not known. However, the maximum of $|\alpha|$ can be determined as $f_1\ |\alpha_1| + f_2\ |\alpha_2| + f_3\ |\alpha_3|\ =\ 0.47$. Assuming $\delta_2 = \delta_3 = 0$, α is found to be 0.39. Ref. [81] on the analysis of decay $B \to K_1\pi$ finds δ_2 and δ_3 as 109 and 123 degrees, from which it is found $\alpha = 0.357 \pm 0.030$. The errors on α is propagated from the errors of the subchannel branching fractions f_i.

The remaining phase factor δ in Eq. 4.1 plays an important role in the direction of the interference, destructive or constructive. Large MC samples are generated based on four values across $(0 - \pi)$ $\delta = 0, 1/2\pi, \pi$, with the total decay amplitude shown in Fig. 4.5. Constructive interference under the resonance $K_1(1270)$ is seen for $\delta = 1/2\pi$ and π, while destructive interference is seen for $\delta = 0$.

To estimate the interference effect to the fit results, 1000 MC samples are generated from PDF directly for each phase $\delta = 0,\ 1/2\pi,\ \pi$. Each of these 1000 MC samples are then fit twice by two models, with and without the interference. The differences in the angular parameters between the two fit models are found to be negligible, while differences in the yields of decays $B \to \varphi K_1(1270)^+$ and $K_1(1400)^+$ are observed. The fraction f in Eq. 4.1 is also varied from the nominal value 0.95 to 0.75, corresponding to $+1\sigma$ and -1σ change to the observed $\varphi K_1(1270)$ and $\varphi K_1(1400)$ yields.

The largest deviations from the nominal fit results in the above tests are assigned as the systematic errors due to the K_1 interference. This introduces a systematic error of 10.3 events for $B^+ \to \varphi K_1(1270)^+$, 11.0 events for $B^+ \to \varphi K_1(1400)^+$, and 7.6 events to the combined yield of $B^+ \to \varphi K_1^+$, as one of the dominant sources of the systmatic errors.

4.4 Signal Efficiencies

In the branching fractions calculations the total efficiency ε of a signal decay is defined as the product of reconstructed efficiency $\varepsilon_{\text{reco}}$ and the daughter branching fractions of

φ and $K_J^{(*)}$ [56]. The reconstruction efficiency is obtained from signal MC samples, by normalizing the reconstructed events to the number of generated events.

Tables 4.9-4.11 summarize the systematic errors in the efficiencies in all final states. They affect the branching fraction error, but do not change the signal significance. The errors on the reconstruction efficiency are typically due to imperfect MC simulation and are obtained from independent studies, such as control samples. When several subchannels contribute, efficiency is quoted for each subchannel.

The corrections to the track finding efficiencies are evaluated from a study of absolute tracking efficiency, resulting in a systematic error of 0.5% per track and the total error of 2.0% for four charged tracks in the $K^+K^-K^+\pi^-$ final states, 1.5% for three charged tracks in the $K^+K^-K_S\pi^+$ and $K^+K^-K^+\pi^0$ final states, and 2.5% for five charged tracks in the $K^+K^-K^+\pi^+\pi^-$ final states.

The error due to particle identification (PID) is about 1.2% for the kaon selection and 0.5% for the pion selection. The errors on the same type of mesons are added linearly, and combined the different types of mesons in quadrature. Particle identification performance has been validated with high-statistics data and MC control samples, such as $\overline{D}^*$-tagged $\overline{D} \to K\pi$ decays. It has been found later that the errors have been underestimated, such as for the $B^0 \to \varphi K^+\pi^-$ decays, the error is only 2.1%. As shown in Tables 4.9-4.11, this change from around 3% to 2% does not affect the total efficiency or the branching fraction. The K_S^0 selection efficiency systematic uncertainty is taken from an inclusive K_S^0

control sample study, giving a total error of 3.5%. The π^0 reconstruction efficiency error is estimated to be 3.0% from a study of τ decays to modes with π^0 mesons.

The reconstruction efficiency has a weak dependence on the longitudinal polarization (f_{LJ}) due to a non-uniform acceptance function of the helicity angles. The measured polarization are used in the efficiency computation. The uncertainty in this measurement translates into a systematic error in the reconstruction efficiency. The polarization f_{LJ} are not properly measured for the low significance (1σ) decays $B^0 \rightarrow \varphi K^*(1680)^0$, $K_3^*(1780)^0$ and $K_4^*(2045)^0$. The lowest reconstruction efficiency is thus used to calculate of branching fraction upper limit of those decay modes as a conservative approach.

Several requirements on the multi-hadronic final state, minimum number of charged tracks, event-shape, the thrust angle θ_T cut and vertex requirements result in a few percent errors. They are found to be independent of the $B \rightarrow \varphi K\pi(\pi)$ final states.

The daughter branching fractions uncertainties are obtained from the PDG [56] for the two body decays of φ and K_J^*. However for the three body decays ($K^+\pi^+\pi^-$) of $K_2^*(1430)^+$, $K_1(1270)^+$, and $K_1(1400)^+$, the branching fractions are taken as the sum of all subchannels, shown in Tables 4.12- 4.13. The total uncertainties on the branching fractions of decays $K_2^*(1430)^+$, $K_1(1270)^+$ and $K_1(1400)^+$ to $(K^+\pi^+\pi^-)$ are calculated as the quadrature sum of the branching fraction weighted uncertainties in each subchannel.

Assumptions are made regarding to the branching fractions of decays $K^*(1410)$ and K_2 to avoid model dependence. For the $K^*(1410)$ decay there is only a lower limit of

40% placed for $K^*(1410) \to K^*(892)\pi$ mode. It is because the only known branching fraction for $K^*(1410)$ decay is $\mathcal{B}(K^*(1410) \to K\pi) = (6.6 \pm 1.3)\%$. This leads to the assumption $\mathcal{B}(K^*(1410) \to K^*\pi) = 0.934 \pm 0.013$ in the branching fraction calculation for decay $B^+ \to \varphi K^*(1410)^+$. On the other hand, there is no known branching fraction for either $K_2(1770)$ or $K_2(1820)$ decay. The only input in PDG [56] is that $K_2(1770)$ decays through $K_2^*(1430)\pi$ dominantly. Thus, in the branching fraction calculations for decays $B^+ \to \varphi K_2(1770)^+$ and $\varphi K_2(1820)^+$, only $K_2 \to K_2^*(1430)\pi$ subchannel is considered.

The width of each K_J^* resonance affects the selection efficiency. This effect is negligible if the data selection window is wide enough to cover the whole resonance range. It is thus only accounted for decays $B^0 \to \varphi K^*(1680)^0/K_3^*(1780)^0/K_4^*(2045)^0$, To estimate the effect to the nominal results, the K_J^* width is varied within 1 σ from the central value, leading to the changes in the efficiency, the largest value is then quoted as systematic error in efficiency, shown in Table 4.9.

4.5 Branching Fraction Calculation

The branching fraction of $B \to \varphi K_J^{(*)}$ is defined as $\mathcal{B} = n_{\rm sig}/(n_{B\overline{B}} \cdot \mathcal{E})$, where the $n_{\rm sig}$ is the number of signal events, $\mathcal{E}$ is the reconstructed efficiency, and $n_{B\overline{B}}$ is the number of $B\overline{B}$ mesons produced. The likelihood distributions in the physically allowed ranges are integrated to compute the branching fraction upper limits at 90% confidence level.

Tables 4.14 and 4.15 show the branching fractions results for the decays $B^0 \to$

Table 4.9: Systematic errors (%) in efficiency for decays $B^0 \to \varphi K_J^{*0}(K^+\pi^-)$. The K_0^*, K_2^*, K_3^* and K_4^* refer to $K_0^*(1430)$, $K_2^*(1430)$, $K_3^*(1780)$ and $K_4^*(2045)$ respectively. The $(K\pi)\dagger$ refers to the nonresonant $B \to \varphi K^+\pi^-$ mode in the higher mass range. The $\varphi(K\pi)_0^{*0}$ and $\varphi K_0^*(1430)^0$ modes are separated to account for different errors in the daughter branching fractions, see Sec. 4.5.

$B^0 \to \varphi$	K_2^*	$(K\pi)_0^*$	K_0^*	$K^*(1680)$	K_3^*	K_4^*	$(K\pi)\dagger$	$\overline{D}$
track finding	2.0	2.0	2.0	2.0	2.0	2.0	2.0	2.0
PID	2.1	2.1	2.1	3.5	3.5	3.5	3.5	3.5
f_{LJ}	0.2	–	–	–	–	–	–	–
event selection	1.0	1.0	1.0	1.0	1.0	1.0	1.0	1.0
thrust angle θ_T cut	1.0	1.0	1.0	1.0	1.0	1.0	1.0	1.0
vertex requirement	2.0	2.0	2.0	2.0	2.0	2.0	2.0	2.0
φ branching fraction	1.2	1.2	1.2	1.2	1.2	1.2	1.2	1.2
K_J^* branching fraction	2.4	0.0	10.8	6.5	5.3	12.1	0.0	1.8
K_J^* width	–	–	–	13.2	2.4	4.3	0.0	0.0
total	4.7	4.0	11.5	15.5	9.2	15.0	4.9	5.2

Table 4.10: Systematic errors (%) in efficiency for decays $B^+ \to \varphi K_2^{*+}(1430)$, $(K\pi)_0^{*+}$ and $K_0^*(1430)^+$, in the final states $K^+K^-(K_S^0\pi^+/K^+\pi^0)$. The $\varphi(K\pi)_0^{*+}$ and $\varphi K_0^*(1430)^+$ modes are separated to account for different errors in the daughter branching fractions, see Sec. 4.5.

$B^+ \to \varphi$	$K_2^*(1430)^+$			$(K\pi)_0^{*+}$		$K_0^*(1430)^+$	
$K_J^{*+} \to$	$K_S\pi^+$	$K^+\pi^0$	$K^+\pi^+\pi^-$	$K_S\pi^+$	$K^+\pi^0$	$K_S\pi^+$	$K^+\pi^0$
track finding	1.5	1.5	2.5	1.5	1.5	1.5	1.5
PID	2.5	3.6	3.7	2.5	3.6	2.5	3.6
K_S^0 selection	3.5	–	–	3.5	–	3.5	–
π^0 selection	–	3.0	–	–	3.0	–	3.0
polarization f_{LJ}	0.9	0.7	0.3	–	–	–	–
event selection	1.0	1.0	1.0	1.0	1.0	1.0	1.0
thrust angle θ_T cut	1.0	1.0	1.0	1.0	1.0	1.0	1.0
vertex requirement	2.0	2.0	2.0	2.0	2.0	2.0	2.0
φ branching fraction	1.2	1.2	1.2	1.2	1.2	1.2	1.2
K_J^* branching fraction	2.4	2.4	5.2	0.0	0.0	10.8	10.8
total	5.9	6.2	7.4	5.3	5.6	12.0	12.1

Table 4.11: Systematic errors (%) in efficiency for decays $B^+ \to \varphi K_J^{(*)+}(K^+\pi^+\pi^-)$, including $K_1(1270)$, $K_1(1400)$, $K^*(1410)$, $K_2(1770)$, and $K_2(1820)$.

$B^+ \to \varphi$	$K_1(1270)$	$K_1(1400)$	$K^*(1410)$	$K_2(1770)$	$K_2(1820)$
track finding	2.5	2.5	2.5	2.5	2.5
PID	3.7	3.7	3.7	3.7	3.7
MC statistics	0.3	0.3	0.3	0.3	0.3
polarization f_{LJ}	2.0	1.0	6.0	4.0	5.0
event selection	1.0	1.0	1.0	1.0	1.0
θ_T cut	1.0	1.0	1.0	1.0	1.0
vertex requirement	2.0	2.0	2.0	2.0	2.0
φ branching fraction	1.2	1.2	1.2	1.2	1.2
K_J^* branching fraction	11.1	6.7	1.4	2.4	2.4
total	12.0	8.6	8.1	7.0	7.6

Table 4.12: Branching fraction calculation of $K_2^*(1430)^+$. The branching fraction $K_2^*(1430)^+ \rightarrow K^+\pi^+\pi^-$ is the sum of two subchannels $K^*(892)^0\pi^+ \rightarrow K^+\pi^-\pi^-$ and $K^+\rho^0 \rightarrow K^+\pi^+\pi^-$, with isospin factors $2/3$ or $1/3$ considered. †: $\pi^0 \rightarrow \gamma\gamma$ branching fraction is embedded in the MC.

Mode	Intermediate Decays	$\mathcal{B}(K_2^{*+} \rightarrow K\pi(\pi))$
$K^+\pi^+\pi^-$	$\mathcal{B}(K_2^{*+} \rightarrow K^{*0}\pi^+) \cdot \mathcal{B}(K^{*0} \rightarrow K^+\pi^-)$ $\frac{2}{3}(24.7 \pm 1.5)\% \cdot \frac{2}{3}$ $\mathcal{B}(K_1^+ \rightarrow K^+\rho^0) \cdot \mathcal{B}(\rho^0 \rightarrow \pi^+\pi^-)$ $\frac{1}{3}(8.7 \pm 0.8)\% \cdot 100\%$	$(13.8 \pm 0.7)\%$
$K_S^0(\pi^+\pi^-)\pi^+$	$\mathcal{B}(K_2^{*+} \rightarrow K^0\pi^+) \cdot \mathcal{B}(K^0 \rightarrow K_S^0(\pi^+\pi^-))$ $\frac{2}{3}(49.9 \pm 1.2)\% \cdot \frac{1}{2}(69.2)\%$	$(11.51 \pm 0.28)\%$
$K^+\pi^0$†	$\mathcal{B}(K_2^{*+} \rightarrow K^+\pi^0)$ $\frac{1}{3}(49.9 \pm 1.2)\%$	$(16.63 \pm 0.40)\%$

Table 4.13: Branching fraction calculation of $K_1^+ \to K^+\pi^+\pi^-$, as the sum of three subchannels $K^{*0}\pi^+ \to K^+\pi^-\pi^+$, $K^+\rho^0 \to K^+\pi^+\pi^-$ and $K_0^{*0}\pi^+ \to K^+\pi^+\pi^-$. Isospin factors $2/3$ or $1/3$ are considered.

	$K_1(1270)^+$	$K_1(1400)^+$
$\mathcal{B}(K_1^+ \to K^{*0}\pi^+) \cdot \mathcal{B}(K^{*0} \to K^+\pi^-)$	$\frac{2}{3}(16 \pm 5)\% \cdot \frac{2}{3}$	$\frac{2}{3}(94 \pm 6)\% \cdot \frac{2}{3}$
$\mathcal{B}(K_1^+ \to K^+\rho^0) \cdot \mathcal{B}(\rho^0 \to \pi^+\pi^-)$	$\frac{1}{3}(42 \pm 6)\% \cdot 100\%$	$\frac{1}{3}(3 \pm 3)\% \cdot 100\%$
$\mathcal{B}(K_1^+ \to K_0^{*0}\pi^+) \cdot \mathcal{B}(K_0^{*0} \to K^+\pi^-)$	$\frac{2}{3}(28 \pm 4)\% \cdot \frac{2}{3}(93 \pm 10)\%$	–
$\mathcal{B}(K_1 \to K^+\pi^+\pi^-)$	$(32.68 \pm 3.64)\%$	$(42.78 \pm 2.85)\%$

$\varphi K_J^{*0}(K^+\pi^-)$ and $B^+ \to \varphi K_J^{(*)+}(K_S^0\pi^+/K^+\pi^0/K^+\pi^+\pi^-)$. The errors on the branching fractions are propagated from the errors on the yields (see Tables 4.6-4.7) and efficiencies (see Tables 4.9-4.10). The errors on $n_{B\overline{B}}$ is estimated to be 1.1%, where equal decay rates of $\Upsilon(4S) \to B^0\overline{B}^0$ and B^+B^- are assumed. The branching fractions upper limits of decays $\varphi K^*(1680)^0$, $\varphi K_3^*(1780)^0$ and $\varphi K_4^*(2045)^0$ are calculated based on the smaller value of the longitudinal (ln) and transverse (tr) reconstruction efficiencies. The 90% confidence level upper limit on $\mathcal{B}$ is quoted with the central values and errors in parentheses. The negative event yield (or $\mathcal{B}$) for $\varphi K_3^*(1780)^0$ in Table 4.14 is extrapolated from the likelihood distribution in the physical range.

The branching fraction $\mathcal{B}(B \to \varphi(K\pi)_0^*)$ refers to the coherent sum $|A_{\text{res}} + A_{\text{non-res}}|^2$ of the $K_0^*(1430)$ resonance and an effective range non-resonant component below the invariant mass of 1.6 GeV, see Sec. 3.2. The resonant and non-resonant contributions cannot

Table 4.14: Results on decays $B^0 \to \varphi K_J^{*0}(K^+\pi^-)$: the reconstruction efficiency $\varepsilon_{\rm reco}$; the total efficiency ε including the daughter branching fractions [56]; the number of signal events $n_{{\rm sig}J}$; significance ($\mathcal{S}$) of the signal; the branching fraction $\mathcal{B}_J$ with the upper limit (UL) at 90% C.L. listed in the parenthesis. The branching fractions upper limits of decays $\varphi K^*(1680)^0$, $K_3^*(1780)^0$ and $K_4^*(2045)^0$ are calculated based on the smaller value of the longitudinal (ln) and transverse (tr) reconstruction efficiencies. The $\mathcal{B}(B^0 \to (K\pi)_0^{*0}\dagger)$ refers to the nonresonant $J^P = 0^+$ $K\pi$ components quoted for $1.60 < m_{K\pi} < 2.15$ GeV. The systematic errors are quoted last.

$B^0 \to \varphi$	$\varepsilon_{\rm reco}$ (%)	ε (%)	$n_{{\rm sig}J}$	$\mathcal{S}$ (σ)	$\mathcal{B}$ (10^{-6})
Lower Mass Range ($1.13 < m_{K\pi} < 1.53$ GeV)					
$K_0^*(1430)^0$					$3.9 \pm 0.5 \pm 0.6$
$(K\pi)_0^{*0}$	23.2 ± 0.9	7.6 ± 0.3	$158 \pm 22 \pm 13$	> 10	$4.3 \pm 0.6 \pm 0.4$
$K_2^*(1430)^0$	26.7 ± 1.0	4.4 ± 0.2	$158 \pm 20 \pm 7$	> 10	$7.5 \pm 0.9 \pm 0.5$
Higher Mass Range ($1.60 < m_{K\pi} < 2.10$ GeV)					
$K^*(1680)^0$	20.8 ± 2.9 (ln) 21.6 ± 3.0 (tr)	2.6 ± 0.4	$8^{+10}_{-7} \pm 11$	0.6	$0.7^{+1.0}_{-0.7} \pm 1.1$ (< 3.5)
$K_3^*(1780)^0$	27.7 ± 2.0 (ln) 28.2 ± 2.1 (tr)	1.7 ± 0.2	$-6 \pm 10 \pm 7$	0.0	$-0.9 \pm 1.4 \pm 1.1$ (< 2.7)
$K_4^*(2045)^0$	23.6 ± 2.1 (ln) 24.5 ± 2.2 (tr)	0.8 ± 0.1	$18^{+14}_{-12} \pm 12$	1.2	$6.0^{+4.8}_{-4.0} \pm 4.1$ (< 15.3)
$(K\pi)_0^{*0}\dagger$	34.8 ± 1.6	11.4 ± 0.6	$47 \pm 16 \pm 15$	2.2	$1.1 \pm 0.4 \pm 0.3$ (< 1.7)
$\overline{D}^0$	33.1 ± 1.6	0.6 ± 0.0	$16 \pm 7 \pm 3$	2.4	$6.5^{+3.1}_{-2.7} \pm 1.4$ (< 11.6)

Table 4.15: Results for decays $B^{\pm} \to \varphi K_J^{(*)\pm}$: the reconstruction efficiency $\varepsilon_{\text{reco}}$; the total efficiency ε, including the daughter branching fractions [56] the number of signal events n_{sig}; significance ($\mathcal{S}$) of the signal; the branching fraction $\mathcal{B}$ with the upper limit (UL) at 90% C.L. listed in the parenthesis. When several subchannels contribute, yield and efficiency are quoted for each subchannel. The $\varphi K_2(1770)^{\pm}$ yield is not considered in the nominal fit and the value indicated with † is obtained with these $\varphi K_2(1820)^{\pm}$ yield constrained to 0. The systematic errors are quoted last.

$B^{\pm} \to \varphi$	$\varepsilon_{\text{reco}}$ (%)	ε (%)	$n_{\text{sig}J}$ (events)	$\mathcal{S}$ (σ)	$\mathcal{B}$ (10^{-6})
$K_1(1270)^{\pm}$	25.4 ± 1.4	4.07 ± 0.51	$116 \pm 26\ ^{+15}_{-14}$	5.0	$6.1 \pm 1.6 \pm 1.1$
$K_1(1400)^{\pm}$	24.6 ± 1.3	5.19 ± 0.44	$7 \pm 39 \pm 18$	< 2	$0.3 \pm 1.6 \pm 0.7$ (< 3.2)
$K_2^*(1430)^{\pm}$		3.34 ± 0.14	$130 \pm 27 \pm 14$	5.5	$8.4 \pm 1.8 \pm 1.0$
$\to K_S^0\pi^{\pm}$	11.9 ± 0.6	0.64 ± 0.04	$27 \pm 6 \pm 3$		
$\to K^{\pm}\pi^0$	12.2 ± 0.7	1.00 ± 0.06	$39 \pm 8 \pm 4$		
$\to K^{\pm}\pi^+\pi^-$	24.7 ± 1.3	1.68 ± 0.12	$64 \pm 14 \pm 7$		
$(K\pi)_0^{*\pm}$		3.33 ± 0.13	$128 \pm 21 \pm 12$	8.2	$8.3 \pm 1.4 \pm 0.8$
$\to K_S^0\pi^{\pm}$	10.9 ± 0.6	1.24 ± 0.07	$48 \pm 8 \pm 4$		
$\to K^{\pm}\pi^0$	12.8 ± 0.7	2.09 ± 0.12	$80 \pm 13 \pm 8$		
$K_0^*(1430)^{\pm}$					$7.0 \pm 1.3 \pm 0.9$
$K^*(1410)^{\pm}$	28.0 ± 2.2	5.71 ± 0.44	$64 \pm 31^{+20}_{-31}$	< 2	$2.4 \pm 1.2\ ^{+0.8}_{-1.2}$ (< 4.3)
$K_2(1770)^{\pm}$	20.8 ± 1.4	2.27 ± 0.16	$(90 \pm 32\ ^{+39}_{-46})^{\dagger}$	< 2	< 15.0
$K_2(1820)^{\pm}$	21.6 ± 1.5	2.35 ± 0.18	$122 \pm 40^{+26}_{-83}$	< 2	< 16.3

be simply separated because of their destructive interference. Therefore, the branching fraction of $B \to \varphi K_0^*(1430)$ and $(K\pi)_0^*$ modes are quoted separately.

The signal yield of $(B \to \varphi(K\pi)_0^*)$ is obtained from the fit. The reconstruction efficiency needs additional correction as the MC sample is generated with resonant decay $B \to \varphi K_0^*(1430)$. The MC sample is re-weighted to yield the correct LASS shape for $(K\pi)_0^*$. So the number of reconstructed events cannot be simply normalized to the number of generated events to get the reconstruction efficiency. Furthermore, the LASS shape has been only tested below 1.6 GeV, see also Ref. [82] for discussion of this effect in the $B \to K\pi$ decay. The branching fraction of $B \to \varphi(K\pi)_0^*$ is thus quoted up to 1.60 GeV.

When re-weighting MC for reconstructed efficiency, the difference of generated $m_{K\pi}$ Breit-Wigner distribution and the empirical LASS distribution is accounted. The reconstructed efficiency of $B \to \varphi(K\pi)_0^*$ with the LASS shape is estimated from the efficiency of Breit-Wigner shape by multiplying the ratio

$$\frac{\int_{1.10}^{1.60} |A_{\mathrm{LASS}}|^2(m_{K\pi}) \times F_{\mathrm{Dalitz}}(m_{K\pi})\, dm_{K\pi}}{\int_{1.10}^{1.60} |A_{\mathrm{BW}}|^2(m_{K\pi}) \times F_{\mathrm{Dalitz}}(m_{K\pi})\, dm_{K\pi}}, \tag{4.6}$$

where $|A_{\mathrm{BW}}|^2$ is normalized in the whole physical range $(m_K + m_\pi, m_B - m_\phi)$, while $|A_{\mathrm{LASS}}|^2$ is normalized in the range $(m_K + m_\pi, 1.6)$GeV.

The branching fraction of decays $B \to \varphi K_0^*(1430)$ is derived from it by integrating separately the Breit-Wigner formula of the resonant component without $m_{K\pi}$ restriction. The $B \to \varphi K_0^*(1430)$ yield is calculated as the product of the $B \to \varphi(K\pi)_0^*$ yield (obtained directly from the fit) and a correction ratio

$$R_{\text{res}} = \frac{\int_{m_L}^{m_U} |A_{\text{res}}|^2(m_{K\pi}) \times F_{\text{Dalitz}}(m_{K\pi})\, dm_{K\pi}}{\int_{m_L}^{m_U} |A_{\text{res}} + A_{\text{non-res}}|^2(m_{K\pi}) \times F_{\text{Dalitz}}(m_{K\pi})\, dm_{K\pi}}, \tag{4.7}$$

where m_L and m_H represent the lower and upper boundaries of the $K\pi$ mass, either (1.13-1.53) GeV for the B^0 modes or (1.10-1.60) GeV for the B^+ modes, and the F_{Dalitz} terms are the phase-space factors for the $B \to \varphi K\pi$ defined in Eq. (3.28). This ratio is 83.3% for the $B^0 \to \varphi K^*(1430)^0$ and 91.5% for the $B^+ \to \varphi K^*(1430)^+$. It varies less than 0.1% from the two final states $(K_S\pi^+)$ and $(K^+\pi^0)$.

Chapter 5

Summary and Discussion

In a summary, this thesis describes three amplitude analyses [59, 60, 62, 63] on decays $B \to \varphi K_J^{(*)}$ based on 465 or 384 million $B\overline{B}$ pairs recorded at *BABAR* detector. A total of fourteen $K_J^{(*)}$ resonances and $\overline{D}^0$ meson are studied, with the projections onto invariant mass $m_{K\pi}$ shown in Fig. 5.1. Tables 5.1– 5.3 summarize the results on branching fractions, polarizations, CP-violation parameters, and parameters sensitive to final-state interactions.

Eleven parameters each on vector–vector decays $B \to \varphi K^*(892)^0$ and $B^\pm \to \varphi K^*(892)^\pm$ [1], nine or five parameters on vector–tensor decay $B^0 \to \varphi K_2^*(1430)^0$ or $B^+ \to \varphi K_2^*(1430)^+$, and two parameters on vector–scalar decays $B^0 \to \varphi K_0^*(1430)^0$ and $B^\pm \to \varphi K_0^*(1430)^\pm$ are extracted. Upper limits at 90% confidence level are placed on branching fractions of B^0 and $B^\pm$ decays to final states with φ and $K^*(1680)^0$, $K_3^*(1780)^0$, $K_4^*(2045)^0$, $\overline{D}^0$, and $K_1(1400)^\pm$, $K^*(1410)^\pm$ and $K_2(1770)^\pm$ or $K_2(1820)^\pm$.

[1] Results on vector–vector decays $B \to \varphi K^*(892)$ are updated by Zijin Guo in a joint effort.

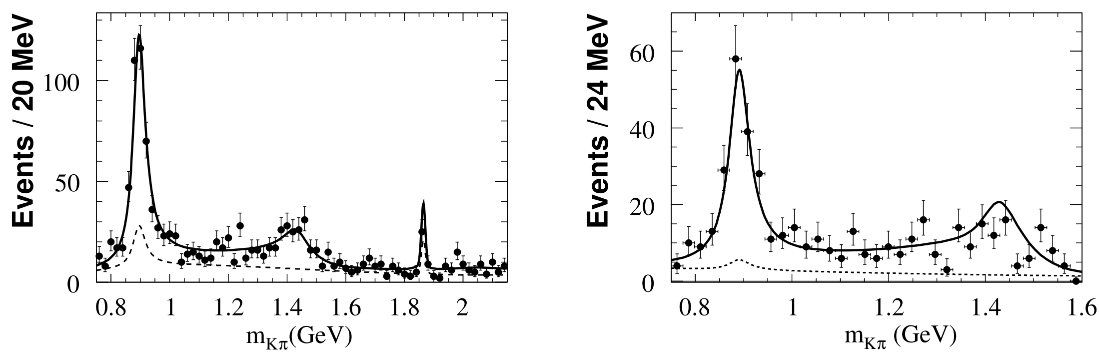

Figure 5.1: Distribution of the $K\pi$ invariant mass for the study of decays $B^0 \to \varphi(K^+\pi^-)$ (left) and $B^\pm \to \varphi(K_S^0\pi^\pm)/(K^\pm\pi^0)$ (right). The data distribution is shown with a requirement to enhance the signal. The solid (dashed) line shows the signal-plus-background (background) expected distributions.

The $(V\text{-}A)$ structure of the weak interaction and the s-quark spin-flip suppression in the process shown in Fig. 1.3 suggest $|A_{J0}| \gg |A_{J+1}| \gg |A_{J-1}|$ [17, 29–34]. The relatively small value of $f_{L1} = 0.494 \pm 0.034 \pm 0.013$ and the relatively large value of $f_{\perp 1} = 0.212 \pm 0.032 \pm 0.013$ in the vector–vector decay remain a puzzle. Furthermore, the polarization of a vector–axial-vector decay $B^+ \to \varphi K_1(1270)^+$ is measured for the first time as $0.46^{+0.12}_{-0.13}{}^{+0.06}_{-0.07}$, resulting in a large fraction of transverse amplitude as well. Both measurements indicate substantial A_{1+1} (or still possible A_{1-1} for vector–axial-vector decay) amplitude from an uncertain source, such as penguin annihilation [17, 29–34] and non-perturbative QCD rescattering [36–39] in the SM, or scalar and right-handed currents from multi-Higgs models beyond the SM [20–28] (see Sec. 1.3).

The naive SM expectation is that the $(V\text{-}A)$ nature of the weak decays requires that an

Table 5.1: Measurements of the branching fraction $\mathcal{B}$, significance and overall flavor asymmetry $\mathcal{A}_{CPJ}$ for $B \to \varphi K_J^*$ and $B \to \varphi \overline{D}^0$. Numbers in parentheses indicate observables measured with less than 4σ significance. The systematic errors are quoted last.

Mode	$\mathcal{B}$ (10^{-6})	$\mathcal{S}$ (σ)	$\mathcal{A}_{CPJ}$
$\varphi K_0^*(1430)^0$	$3.9 \pm 0.5 \pm 0.6$	> 10	$+0.20 \pm 0.14 \pm 0.06$
$\varphi K_0^*(1430)^+$	$7.0 \pm 1.3 \pm 0.9$	8.2	$+0.04 \pm 0.15 \pm 0.04$
$\varphi K^*(892)^0$	$9.7 \pm 0.5 \pm 0.5$		$+0.01 \pm 0.06 \pm 0.03$
$\varphi K^*(892)^+$	$11.2 \pm 1.0 \pm 0.9$	> 10	$+0.00 \pm 0.09 \pm 0.04$
$\varphi K^*(1680)^0$	$< 3.5(0.7^{+1.0}_{-0.7} \pm 1.1)$	< 2	Fixed to 0
$\varphi K_2^*(1430)^0$	$7.5 \pm 0.9 \pm 0.5$	> 10	$-0.08 \pm 0.12 \pm 0.05$
$\varphi K_2^*(1430)^+$	$8.4 \pm 1.8 \pm 1.0$	5.5	$-0.23 \pm 0.19 \pm 0.06$
$\varphi K_3^*(1780)^0$	$< 2.7(-0.9 \pm 1.4 \pm 1.1)$	< 2	Fixed to 0
$\varphi K_4^*(2045)^0$	$< 15.3(6.0^{+4.8}_{-4.0} \pm 4.1)$	< 2	Fixed to 0
$\varphi K_1(1270)^+$	$6.1 \pm 1.6 \pm 1.1$	5.0	$+0.15 \pm 0.19 \pm 0.05$
$\varphi K_1(1400)^+$	$< 3.2(0.3 \pm 1.6 \pm 0.7)$	< 2	Fixed to 0
$\varphi K^*(1410)^+$	$< 4.3(2.4 \pm 1.2^{+0.8}_{1.2})$	< 2	Fixed to 0
$\varphi K_2(1770)^+$	< 15.0	< 2	Fixed to 0
$\varphi K_2(1820)^+$	< 16.3	< 2	Fixed to 0
φD^0	$< 11.6(6.5^{+3.1}_{-2.7} \pm 1.4)$	2.4	Fixed to 0

Table 5.2: Summary of the angular measurements, see Table 1.5 for definition of the parameters. The measurements in the parenthesis are for $B^+ \to \varphi K^*(892)^+$ or $\varphi K_2^*(1430)^+$ decays. The systematic errors are quoted last.

parameter	$\varphi K^*(892)^{0(+)}$	$\varphi K_1(1270)^+$	$\varphi K_2^*(1430)^{0(+)}$
f_{LJ}	$0.494 \pm 0.034 \pm 0.013$	$0.46^{+0.12}_{-0.13}{}^{+0.06}_{-0.07}$	$0.901^{+0.046}_{-0.058} \pm 0.037$
	$(0.49 \pm 0.05 \pm 0.03)$		$(0.80^{+0.09}_{-0.10} \pm 0.03)$
$f_{\perp J}$	$0.212 \pm 0.032 \pm 0.013$		$0.002^{+0.018}_{-0.002} \pm 0.031$
	$(0.21 \pm 0.05 \pm 0.02)$		
$\phi_{\parallel J}$ $(-\pi)$ (rad)	$2.40 \pm 0.13 \pm 0.08$		$3.96 \pm 0.38 \pm 0.06$
	$(-0.67^{+0.20}_{-0.19} \pm 0.07)$		
$\phi_{\perp J}$ $(-\pi)$ (rad)	$2.35 \pm 0.13 \pm 0.09$		
	$(-0.45^{+0.19}_{-0.20} \pm 0.07)$		
$\mathcal{A}^0_{CPJ}$	$+0.01 \pm 0.07 \pm 0.02$		$-0.05 \pm 0.06 \pm 0.01$
	$(+0.17 \pm 0.11 \pm 0.02)$		
$\mathcal{A}^\perp_{CPJ}$	$-0.04 \pm 0.15 \pm 0.06$		
	$(+0.22^{+0.24}_{-0.23} \pm 0.08)$		
$\Delta\phi_{\parallel J}$ (rad)	$+0.22 \pm 0.12 \pm 0.08$		$-1.00 \pm 0.38 \pm 0.09$
	$(+0.07 \pm 0.20 \pm 0.05)$		
$\Delta\phi_{\perp J}$ (rad)	$+0.21 \pm 0.13 \pm 0.08$		
	$(+0.19^{+0.20}_{-0.19} \pm 0.07)$		

Table 5.3: Summary of the interference measurements, see Table 1.5 for definition of the parameters. The measurements in the parenthesis are for $B^+ \to \varphi K^*(892)^+$ or $\varphi K_2^*(1430)^+$ decays. The systematic errors are quoted last.

parameter	$\varphi K^*(892)^{0(+)}$	$\varphi K_2^*(1430)^{0(+)}$
δ_{0J} $(-\pi)$ (rad)	$2.82 \pm 0.15 \pm 0.09$	$3.41 \pm 0.13 \pm 0.13$
	$(-0.07 \pm 0.18 \pm 0.06)$	$(3.59 \pm 0.0.19 \pm 0.12)$
$\Delta\delta_{0J}$ (rad)	$+0.27 \pm 0.14 \pm 0.08$	$+0.11 \pm 0.13 \pm 0.06$
	$(+0.20 \pm 0.18 \pm 0.03)$	$(-0.05 \pm 0.19 \pm 0.06)$

anti-quark originating from the $\bar{b} \to \bar{q}W^+$ decay be produced in helicity state $+\frac{1}{2}$. This argument applies to the penguin loop which is a purely weak transition, $\bar{b} \to \bar{s}$, with the double-W coupling in the SM. The $\bar{s}$ anti-quark can couple to the s quark (see Fig. 1.3) to produce the φ state with helicity of either $\lambda = 0$ or $\lambda = +1$, but not $\lambda = -1$. However, the K^* state should have the same helicity as the φ due to angular momentum conservation. The $\lambda = +1$ state is not allowed in this case because both s and $\bar{s}$ quarks would have helicity $+\frac{1}{2}$, in violation of helicity conservation in the vector coupling, $\mathrm{g} \to s\bar{s}$. The spin-flip can alter both of the above requirements, but its suppression factor is of order $\sim m_V/m_B$ for each flip, where m_V is the mass of the φ or K^{*0} mesons. It leads to the amplitude hierarchy $|A_{J0}| \gg |A_{J+1}| \gg |A_{J-1}|$, or $|A_{J0}| \gg |A_{J\perp}|$ and $A_{J\perp} \simeq A_{J\parallel}$, where A_{J+1} is suppressed by one spin flip, while A_{J-1} is suppressed by two spin flips.

The polarizations of the vector–tensor decays $B^0 \to \varphi K_2^*(1430)$ and $B^+ \to$

$\varphi K_2^*(1430)^+$ are measured to be $0.901^{+0.046}_{-0.058}\pm0.037$ and $0.80^{+0.09}_{-0.10}\pm0.03$ respectively, both consistent with the naive expectation of the longitudinal polarization dominance. However the difference in f_L of the vector–tensor decay from the vector-vector(axial-vector) decay brings additional puzzle. This points to a unique role for the spin-1 particle recoiling against the φ in the $B \to \varphi K^*$ polarization puzzle.

The dependence on the $K\pi$ invariant mass of the interference between the scalar and vector or scalar and tensor components is implemented to resolve discrete ambiguities of both the strong and weak phases (see Sec. 3.1 and 3.3). In $B \to \varphi K^*(892)$ decays, the solution $\phi_{\parallel 1} \simeq \phi_{\perp 1}$ is found without discrete ambiguities. Combined with the approximate solution $f_{L1} \simeq 1/2$ and $f_{\perp 1} \simeq (1-f_{L1})/2$, this results in the approximate decay amplitude hierarchy $|A_{10}| \simeq |A_{1+1}| \gg |A_{1-1}|$. This measurement thus contradicts the proposed right-handed current [17,20,21] prediction $|A_{-1}| \gg |A_{+1}|$. In addition, more than more than 5 σ (4 σ) or 3.1σ (2.4σ) deviation (including systematic uncertainties) is found of $\phi_\perp(\phi_\parallel)$from either π or zero in the $B^0 \to \varphi K^*(892)^0$ or $B^\pm \to \varphi K^*(892)^\pm$ decay. This indicates the presence of final-state interactions (FSI) not accounted for in the naive factorization. In the $B^0 \to \varphi K_2^*(1430)^0$ decay, there is no sufficient information to constrain the $\phi_{\parallel 2}$ at higher significance or to measure $\phi_{\perp 2}$, $A_{CP2}^{\perp}$, or $\Delta\phi_{\perp 2}$, due to the low significance of the $f_{\parallel 2} = (1 - f_{L2} - f_{\perp 2})$ (1.9 σ) and $f_{\perp 2}$ (0 σ) measurements.

The new polarization measurements on the vector–tensor and vector–axial-vector decays have limited constraint on the current theoretical explanations. The penguin annihilation and rescattering solutions in the SM are not either ruled out or distinguished. This is because there is new set of parameters specific to the new $K_2^*(1430)$ or $K_1(1270)$ final state. Some of these parameters are virtually impossible to calculate due to the difficulties in the QCD factorization, just as those parameters defined in $B \to \varphi K^*(892)$ decays,

New physics scenarios are not ruled out either for two reasons. First, the coupling strength of the NP sector to the SM physics is not exactly understood. Second, the calculations of the NP contributions also have similar large QCD uncertainties, such as the two universal form factors in the $B \to K_J^*$ transition. However, it is pointed out in Ref. [28] that, models which contain only V/A operators like those with SUSY or extra $Z\prime$ bosons cannot explain both the $B^0 \to \varphi K_S^0$ and $B \to \varphi K^*$ data. Nevertheless, it is safe to conclude that the models that have weak dependence on the K_J^* final states are not in favor.

Bibliography

[1] Dirac, P.A.M., Principles of Quantum Mechanics, 4th edition (Clarendon, 1982)

[2] Gordon Kane, Modern Elementary Particle Physics, updated edition (Addison-Wesley Publishing Company, 1993)

[3] P. Higgs, Phys. Rev. Lett. **13**, 508-509 (1964).

[4] P. Higgs, Phys. Rev. **145**, 1156-1163 (1966).

[5] Noether E (1918), Math-phys. Klasse 1918: 235-257.

[6] N. Cabibbo, Phys. Rev. Lett. **10**, 531 (1963).

[7] M. Kobayashi and T. Maskawa, Prog. Theor. Phys. **49**, 652 (1973)

[8] L. Wolfenstein, Phys. Rev. Lett. **51**, 1945 (1983).

[9] Y. Grossman and M. P. Worah, Phys. Lett. B **395**, 241 (1997).

[10] D. London and A. Soni, Phys. Lett. B **407**, 61-65 (1997).

[11] CLEO Collaboration, R.A. Briere *et al.*, Phys. Rev. Lett. **86**, 3718 (2001).

[12] *BABAR* Collaboration, B. Aubert *et al.*, Phys. Rev. Lett. **87**, 151801 (2001);

[13] *BABAR* Collaboration, B. Aubert *et al.*, Phys. Rev. D **65**, 051101 (2002).

[14] *BABAR* Collaboration, B. Aubert *et al.*, Phys. Rev. Lett. **91**, 171802 (2003);

[15] *BABAR* Collaboration, B. Aubert *et al.*, Phys. Rev. Lett. **93**, 231804 (2004).

[16] BELLE Collaboration, K.-F. Chen *et al.*, Phys. Rev. Lett. **91**, 201801 (2003).

[17] A. L. Kagan, Phys. Lett. B **601**, 151 (2004).

[18] BELLE Collaboration, J. Zhang *et al.*, Phys. Rev. Lett. **95**, 141801 (2005).

[19] *BABAR* Collaboration, B. Aubert *et al.*, Phys. Rev. Lett. **97**, 201801 (2006).

[20] Y. Grossman, Int. J. Mod. Phys. A **19**, 907 (2004).

[21] E. Alvarez *et al.*, Phys. Rev. D **70**, 115014 (2004).

[22] C. H. Chen and C. Q. Geng, Phys. Rev. D **71**, 115004 (2005).

[23] C. S. Huang *et al.*, Phys. Rev. D **73**, 034026 (2006).

[24] Y. D. Yang *et al.*, Phys. Rev. D **72**, 015009 (2005).

[25] A. Faessler *et al.*, Phys. Rev. D **75**, 074029 (2007).

[26] C. H. Chen and H. Hatanaka, Phys. Rev. D **73**, 075003 (2006).

[27] P. K. Das and K. C. Yang, Phys. Rev. D **71**, 094002 (2005).

[28] A. Datta *et al.*, arXiv:0811.2957[hep-ph]

[29] H.-n. Li and S. Mishima, Phys. Rev. D **71**, 054025 (2005).

[30] C.-H. Chen et al., Phys. Rev. D **72**, 054011 (2005).

[31] M. Beneke *et al.*, Nucl. Phys. B **774**, 64 (2007).

[32] C.-H. Chen and C.-Q. Geng, Phys. Rev. D **75**, 054010 (2007).

[33] A. Datta *et al.*, Phys. Rev. D **76**, 034015 (2007).

[34] H.-Y. Cheng, K.-C. Yang, Phys. Rev. D **78**, 094001 (2008).

[35] M. Beneke *et al.*, Phys. Rev. Lett. **96**, 141801 (2006).

[36] C. W. Bauer *et al.*, Phys. Rev. D **70**, 054015 (2004).

[37] P. Colangelo *et al.*, Phys. Lett. B **597**, 291 (2004).

[38] M. Ladisa *et al.*, Phys. Rev. D **70**, 114025 (2004).

[39] H. Y. Cheng *et al.*, Phys. Rev. D **71**, 014030 (2005).

[40] K. Wilson and W. Zimmermann, Comm. Math. Phys. , **24**, 87 (1972).

[41] J. Charles, Phys. Rev. D**60**, 014001 (1999).

[42] M. Gell-Mann and F. Low, Phys. Rev. **84**, 350-354 (1951).

[43] E. C. G. Stueckelberg and A. Petermann, Helv. Phys. Acta **26**, 499-520 (1953).

[44] M. Gell-Mann and F. E. Low, Phys. Rev. **95**, 1300-1312 (1954).

[45] L.V. Ovsyannikov, Dokl. Akad. Nauk Ser. Fiz. **109**, 1112-1114 (1956).

[46] G. 't Hooft, Nucl. Phys. B **61**, 455-468 (1973).

[47] S. Weinberg, Phys. Rev. Lett. **31**, 494-497 (1973).

[48] A. Datta and D. London, Int. J. Mod. Phys. A **19**, 2505 (2004).

[49] A. V. Gritsan and J. G. Smith, Phys. Lett. B **667**, 1 (2008).

[50] G. Buchalla, *et al.*, Rev. Mod. Phys. **98**, 1125 (1996).

[51] T. P. Cheng, *et al.*, Phys. Rev. D, **35**, 3484 (1987).

[52] D. Atwood, *et al.*, Phys. Rev. D, **55**, 3156 (1997).

[53] *BABAR* Collaboration, B. Aubert *et al.*, Nucl. Instrum. Meth. A**479**, 1 (2002)

[54] PEP-II Conceptual Design Report, SLAC Report No. SLAC-R-418,(1993).

[55] D.N. Brown *et al.*, arXiv:0809.3823 [physics.ins-det]

[56] Particle Data Group, C. Amsler *et al.*, Phys. Lett. B **667**, 1 (2008).

[57] *BABAR*-DIRC Collaboration, I. Adam *et al.*, Nucl.Instrum.Meth. **A538**, 281-357 (2005)

[58] P. Billoir, Nucl. Instr. Methods **A225**, 225 (1984)

[59] *BABAR* Collaboration, B. Aubert *et al.*, Phys. Rev. Lett. **98**, 051801 (2007).

[60] *BABAR* Collaboration, B. Aubert *et al.*, Phys. Rev. D **76**, 051103 (2007).

[61] *BABAR* Collaboration, B. Aubert *et al.*, Phys. Rev. Lett. **99**, 201802 (2007);

[62] *BABAR* Collaboration, B. Aubert *et al.*, Phys. Rev. Lett. **101**, 161801 (2008);

[63] *BABAR* Collaboration, B. Aubert *et al.*, Phys. Rev. D **78**, 092008 (2008).

[64] M. Jacob and G. C. Wick, Ann. Phys. **7**, 404 (1959).

[65] S. M. Berman and M. Jacob, Phys. Rev. 139, 1023 (1965).

[66] A. Datta *et al.*, Phys. Rev. D. **77**, 114025 (2008).

[67] *BABAR* Collaboration, B. Aubert *et al.*, Phys. Rev. D **70**, 032006 (2004).

[68] LASS Collaboration, D. Aston *et al.*, Nucl. Phys. B **296**, 493 (1988).

[69] *BABAR* Collaboration, B. Aubert *et al.*, Phys. Rev. D **72**, 072003 (2005).

[70] W. M. Dunwoodie, on behalf of the LASS Collaboration, private communications.

[71] S. Agostinelli *et al.*, Nucl. Instrum. Methods Phys. Res., Sect. A **506**, 250 (2003).

[72] ACCMOR Collaboration, C. Daum *et al.*, Nucl. Phys. B **187**, 1 (1981).

[73] E791 Collaboration, E. M. Aitala *et al.*, Phys. Rev. Lett. **86**, 765 (2001).

[74] *BABAR* Collaboration, B. Aubert *et al.*, Phys. Rev. D **71**, 032005 (2005).

[75] *BABAR* Collaboration, B. Aubert *et al.*, Phys. Rev. D **78**, 012004 (2008).

[76] E. P. Wigner, Phys. Rev. D **98**, 145 (1955)

[77] F. James *et al.*, MINUIT, Function Minimization and Error Analysis CERN Program Library.

[78] R. Brun and F. Rademakers, Root data-analysis framework, Nucl. Inst. and Meth. in Phys. Res., Sect. A **389**, 81 (1997); see also http://root.cern.ch/.

[79] ARGUS Collaboration, H. Albrecht *et al.*, Phys. Lett. **B 241**, 278 (1990).

[80] M. Gronau and J. L. Rosner, Phy. Lett. B **666**, 185-188 (2008).

[81] Presented at 34th International Conference on High Energy Physics (ICHEP 08).

[82] *BABAR* Collaboration, B. Aubert *et al.*, Phys. Rev. D **72**, 072003 (2005)

[83] We perform averaging of the latest results, otherwise refer to E. Barberio *et al.* [Heavy Flavor Averaging Group], arXiv:0704.3575 [hep-ex] and online update at http://www.slac.stanford.edu/xorg/hfag.

Vita

Yanyan Gao was born in Jiang Su Province of China in September of 1982. She enrolled as an undergraduate in the University of Science and Technology Beijing in 1999. She graduated with a Bachelor of Science degree in Applied Physics in 2003. During the four years in the university, she was granted many Chinese awards and scholarships, such as the People Scholarship and the National Scholarship.

In August of 2003, Yanyan entered the Johns Hopkins University and started the Ph.D program in the physics. In the first three years, she worked as a teaching assistant. In the December of 2006, she moved to the SLAC National Accelerator Laboratory and concentrated on the research in experimental particle physics. In the December of 2008, Yanyan completed the requirements for a Doctor of Philosophy degree in physics.